UNIVERSITÄT ZU LÜBECK

From the Institute of Biomedical Optics
of the University of Lübeck
Director: Prof. Dr. Robert Huber

"Harmonic Light from Membrane Resonators"

Dissertation
for Fulfillment of
Requirements
for the Doctoral Degree
of the University of Lübeck

from the Department of Natural Sciences

Submitted by
Jörn Wollenzin
from
Lidingö, Sweden

Lübeck, 2025

First referee: Prof. Dr. Robert Huber
Second referee: Prof. Dr. Kai Seger
Date of oral examination: May 8, 2026
Approved for printing: Lübeck, May 12, 2026

Acknowledgements

I would like to express my heartfelt gratitude to all those who have supported and guided me throughout my Doctoral journey.

First and foremost, I would like to thank my supervisor, Robert Huber, for his support, for encouraging me to embark on the path that led to this work, and for accepting me as a doctoral student.

A special thanks goes to Kai Seger for inviting me to join his team, work in his lab, and for our many fruitful discussions that have greatly enriched my research.

I am deeply grateful to Bruno Gross and Julien Vigroux, who provided crucial support for my scientific work while I balanced my professional position. Their encouragement and forward-looking attitude were vital during this process.

I would also like to acknowledge Matt Kirchner, Michael Verges, Johannes Dühn, Matthias Neef, and Matthias Voelker from the Thorlabs team for their support, the many exciting technical discussions and their understanding, especially during the times when I was physically and mentally less present within the team.

My sincere thanks go to Ulrich Sowada, my professor from Kiel, whose passion for optics and lasers ignited my own interest in the field and has been a guiding inspiration throughout my career.

I am incredibly grateful to Garrett Cole for his tremendous support, especially in the discussions we had and for enabling the excellent bonding and processing of the MECSEL gain chips, a critical part of this work.

I would also like to express my thanks to Imke Grube and Heike Jurzig, who were both excellent writing buddies, and are amongst my trusted friends Matthias Kornblum and Indra Stülcken, who helped me navigate the challenging and stormy years of this journey.

Finally, I owe my deepest gratitude to my mother Hanne and my father Jürgen, whose endless love and support have been a constant source of strength and encouragement.

Abstract

The subject of this thesis is the exploration of novel approaches that enable the technology of optically pumped membrane external cavity surface emitting lasers (MECSEL) to serve demanding applications in the optical cooling of ultra-cold atoms used in optical clocks, fundamental physics studies and quantum computing. With emission in the visible spectrum, the lasers are operated at a single longitudinal mode (SLM) with narrow line width (20 kHz) in linear standing wave cavities.

The technology explored and improved provides means of mode hop prevention in continuous tuning or frequency locked operation. It suggests a technological concept to fundamentally overcome the MECSEL disadvantage of un-controlled position of the intra-cavity standing wave pattern with respect to the Quantum Wells (QW) in the gain structure, while in addition supports mode filtering and mode hop prevention through active stabilization of the resonant mode. The thermally induced lens in the MECSEL gain chip assembly is numerically analyzed with respect to the strengst of the first-order lens, as well as distorting aberrations. The dynamic response upon pump modulation is analyzed and discussed towards judgement of the feasibility to enable pump-induced frequency control of the laser system. All computation results are compared to experimental data.

The thesis provides a technological background, and describes the design optimization of longitudinal and transverse optimization of the laser setup. The spectal filters required, as well as a theoretical analysis of coupled-cavity concepts are presented. The optimization is accompanied by thorough analysis of thermally induced optical distortions. Parasiteric effects that create a burdon on tunable single-frequency operation are discussed. Intra-cavity harmonic light generation is introduced in order to provide high efficiency conversion of pump radiation into a narrow line width output in the visible spectrum. Line width and intensity noise are experimentally determined and compared with theoretical limits. Finally, the results are discussed and compared with scientific data provided by other groups.

Zusammenfassung

Inhalt dieser Dissertation ist die Untersuchung neuer Ansätze, die es der Technologie der optisch gepumpten Membranlaser mit externer Kavität (MECSEL) ermöglichen, anspruchsvolle Anwendungen in der optischen Kühlung von ultrakalten Atomen zu bedienen, die in optischen Uhren, fundamentalen physikalischen Studien und der Quantencomputing-Technologie verwendet werden. Mit Emission im sichtbaren Spektrum werden die Laser im Einfrequenzmodus (SLM) mit schmaler Linienbreite (20 kHz) in linearen Stehwellenresonatoren betrieben.

Die untersuchte und verbesserte Technologie bietet Lösungen zur Verhinderung von Modensprüngen im kontinuierlichen Durchstimmen oder frequenzstabilen Dauerbetrieb. Es wird ein technologisches Konzept vorgestellt, das den MECSEL-Nachteil der unkontrollierten Position des stehenden Wellenmusters im Resonator im Hinblick auf die Quantengitter (QW) in der Verstärkungsstruktur grundsätzlich überwindet und gleichzeitig die Modenselektion sowie die Verhinderung von Modensprüngen durch aktive Stabilisierung der resonanten Mode unterstützt. Die thermisch induzierte Linse in der MECSEL-Verstärker-Chip-Baugruppe wird numerisch hinsichtlich der Stärke der Linse erster Ordnung, sowie der Verzerrungsfehler analysiert. Die dynamische Reaktion auf Pumpleistungsmodulation wird analysiert und im Hinblick auf die Beurteilung der Realisierbarkeit einer Pumpleistungs-induzierten Frequenzkontrolle des Lasersystems diskutiert. Alle Berechnungsergebnisse werden mit experimentellen Daten verglichen.

Die Dissertation bietet eine Einführung in den technologischen Hintergrund und beschreibt die Optimierung des Designs in der longitudinalen und transversalen Ausrichtung des Laseraufbaus. Die erforderlichen Spektralfilter, sowie eine theoretische Analyse von gekoppelten Resonator-Konzepten, werden aufgezeigt. Die Optimierung wird von einer weitreichenden Analyse der thermisch induzierten optischen Verzerrungsfehler begleitet. Parasitäre Effekte, die den abstimmbaren Einzelmodusbetrieb erschweren, werden diskutiert. Die resonatorinterne harmonische Lichterzeugung wird erläutert, mit der eine hoch effiziente Umwandlung der Pumpstrahlung in einen schmalbandigen Ausgang im sichtbaren Spektrum möglich wird. Linienbreite und Intensitätsrauschen werden experimentell bestimmt und mit theoretischen Grenzwerten verglichen. Schließlich werden die Ergebnisse diskutiert und mit wissenschaftlichen Daten anderer Gruppen verglichen.

Contents

List of Abbreviations

AOM . . . . . Acousto-optical modulator

AR . . . . . Anti-reflection (coating)

ASE . . . . . Amplified spontaneous emission

BBO . . . . . Barium borate

BOA . . . . . Broad-band optical amplifier

BRF . . . . . Birefringent filter

CTE . . . . . Coefficient of thermal expansion

cw . . . . . Continous wave (emission of a laser, not pulsed)

DBR . . . . . Distributed Bragg reflector

DFB . . . . . Distributed feedback

DHR . . . . . Dual HR - mirror reflecting two wavelength ranges

DPSSL . . . . Diode-pumped vertical external-cavity surface-emitting semiconductor laser

ECDL . . . . . External-cavity diode laser

EEL . . . . . Edge emitting laser

EFL . . . . . Effective focal length

FET . . . . . Field-effect transistor

FFT . . . . . Fast Fourier transform

FP . . . . . Fabry-Perot

FPI . . . . . Fabry-Perot interferometer

FSR . . . . . Free spectral range

FWHM . . . . Full width half maximum

GDD . . . . . Group delay dispersion

H-MECSEL . Hybrid MECSEL (one reflective coating applied directly to the gain chip)

KDP . . . . . Potassium dihydrogen phosphate

LBO . . . . . Lithium Triborate

MECSEL . . . Membrane external cavity semiconductor surface emitting laser

MOT . . . . . Magneto-optical trap

MOVPE . . . Metal-organic vapor-phase epitaxy

MQW . . . . . Multi-quantum well

NIR . . . . . Near-infrared sprectral range (760 nm to 2500 nm)

OSA . . . . . Optical spectrum analyzer

PBS . . . . . Polarizing beam splitter

PDH . . . . . Pound-Drever-Hall - method of locking a laser to a resonant cavity

PID . . . . . Proportional–integral–derivative controller

PTR . . . . . Photo-thermo-refractive (glass)

PZT . . . . . Lead zirconium titanate - a piezo-electric material

QPM . . . . . Quasi-phase-matching

QW . . . . . Quantum Well

RF . . . . . Radio frequency

RIN . . . . . Relative intensity noise

ROC . . . . . Radius of curvature

RPG . . . . . Resonant periodic gain

SFP . . . . . Scanning fabry perot interferometer

SHG . . . . . Second harmonic generation

SLD . . . . . Superluminescent diode

SLM . . . . . Single longitudinal mode

SM . . . . . Single mode

SNR . . . . . Signal-to-noise ratio

TE . . . . . Transverse electric - polarized light with its electric field being perpendicular to the plane of incidence

TEC . . . . . Thermo-electric cooler

TEM . . . . . Transverse electromagnetic mode(s)

TM . . . . . Transverse magnetic - polarized light with its magnetic field being perpendicular to the plane of incidence

TMM . . . . . Transmission matrix method

VCO . . . . . Voltage controlled oscillator

VCSEL . . . . Vertically-emitting semiconductor laser

VECSEL . . . Vertical cavity surface emitting semiconductor laser

1 Introduction and Background

1.1 Semiconductor Lasers

The first demonstration of a semiconductor laser was published in 1962 [1]. A GaAs chip with a p-n junction was operated at 77 K (liquid nitrogen temperature) and pumped with 5 µs to 20 µs current pulses. It did not show single transverse mode operation yet, but emitted coherent radiation around 850 nm. In the same year, room temperature operation and optical pumping were demonstrated [2]. In the following decades, semiconductor laser technology was further developed to suit applications in communications, optical data storage [3] and many other. Introduction of optical feedback technology [4] and various forms of gratings [5] improved the spectral purity of semiconductor devices and enabled spectroscopic application of semiconductor lasers [6]. Optimized mounting and cooling technologies, and stacking of multi-diode laser bars, enabled output powers in the kW range [7], making semiconductor lasers a feasible light source in welding and marking applications [8]. Volumetric Holographic Grating technology, using photo-thermo-refractive (PTR) glass [9], significantly increased the brightness of high power laser diode assemblies, both by spatial filtering, high brightness spectral narrowing photo thermo refractive glass, phase locking and spectral beam combining [10]. In the field of narrow linewidth and spatially single mode lasers, though, these methods of power scaling and spectral

narrowing have significant limitations [11]. In the 1990s, semiconductor optical amplifiers were developed that achieved significantly higher single transverse mode output powers using a tapered design that significantly increased the gain and output area, preventing damage at the exit surface [12]. At the cost of introducing significant amplified spontaneous emission signal to the spectrum of the core laser, this method is the state-of-the-art for creation of Watt-level narrow linewidth ($\Delta f \ll 1\,\mathrm{MHz}$) lasers for spectroscopic or laser cooling applications [13].

Commercial semiconductor laser development has clearly focused on Gallium Arsenide (GaAs) based instruments (850 nm), Gallium-Indium-Phosphite (GaInP) laser in the red (used in CD technology), Gallium Nitride (GaN) devices in the UV, blue and green [14]. Indium Phosphite (InP) devices for use in the 1550 nm region were commercially developed when telecom applications emerged in the 1990s [15]. The reason for this is the zero Group Delay Dispersion (GDD) of silica fibers around that wavelength [16]. Still, some spectral regions in the UV and visible wavelength region, as well as the "gap region" between GaAs-based Quantum Well (QW) and InP-based lasers around 1200 nm are not commercially covered.

1.2 Nonlinear Frequency Conversion

Very early in the development of lasers, scientific groups worked on extending the spectral coverage of laser light, so far limited to specific energy levels of the host material, by nonlinear frequency conversion. In 1961, a ruby laser (at that time still called "optical maser") at 694.3 nm, flashlamp pumped with 1 ms pulses, was focused into crystalline quartz and sufficient efficiency could be reached to prove second harmonic generation (SHG) in the UV (347 nm) [17]. They observed a certain dependency on birefringence of SHG efficiency. Later, the concept of phase matching was described [18]. Maker et al. chose potassium dihydrogen phosphate (KDP) for SHG generation, since its birefringence is larger than its dispersion. Matching the phase delay of fundamental and SHG light by carefully choosing temperature and crystal angle, a 300-fold increase in conversion efficiency was reported. Three years later, the concept of optical parametric amplification was

demonstrated in KDP, pumped with an intense 530 nm beam, a signal wavelength at 1060 nm, showing noticeable amplification of 630 nm light [19]. Still, there were some limitations in efficiency due to birefringent walk-off in Type-II phase matching (where the laser light does not exactly travel along one crystalline axis). This can be circumvented by the concept of periodic poling, which was first demonstrated in crystalline fibers in 1985 [20], through a 5 cm long lithium niobate ($LiNbO_3$) piece. In 2007, periodic poling of bulk $LiNbO_3$ in combination with a Bragg grating could increase the OPO slope efficiency to 75 % [21].

1.3 Vertical Cavity Surface Emitting Lasers

In the first decades of semiconductor lasers, the technology focused on edge-emitting lasers (EEL) of various types, external cavity feedback systems and embedded distributed feedback (DFB) designs. In this operating principle, the laser resonance travels along the active area, guided by the refractive index, and is emitted at the edge of the structure [22], as depicted in figure 1.1a. In 1977, Kenichi Iga from the Tokyo Institute of Technology proposed a novel concept, the vertically-emitting semiconductor laser (VCSEL) [23]. Two years later, the first device composed of a GaInAsP/InP structure was reported [24]. This device already incorporated a vertical double heterostructure, where the vertically-emitting active layer of GaInAsP was surrounded by doped InP structures, which confine electrons and holes in the interacting region called the Quantum Well (see chapter 2.6). In this approach, the resonant beam travels in a direction perpendicular to the active gain layer, or, in later, more efficient devices, through a structure of multiple Quantum Wells. Through thermal and current-induced refractive index variations, and careful design of the aperture, single transverse mode operation can be reached. The end mirrors of the cavity are epitaxially grown along with the active area, or grown separately and optically bonded against it. Proper design of total optical thickness (with respect to the gain bandwidth) allows these devices to limit the emission to a single longitudinal resonance mode as well.

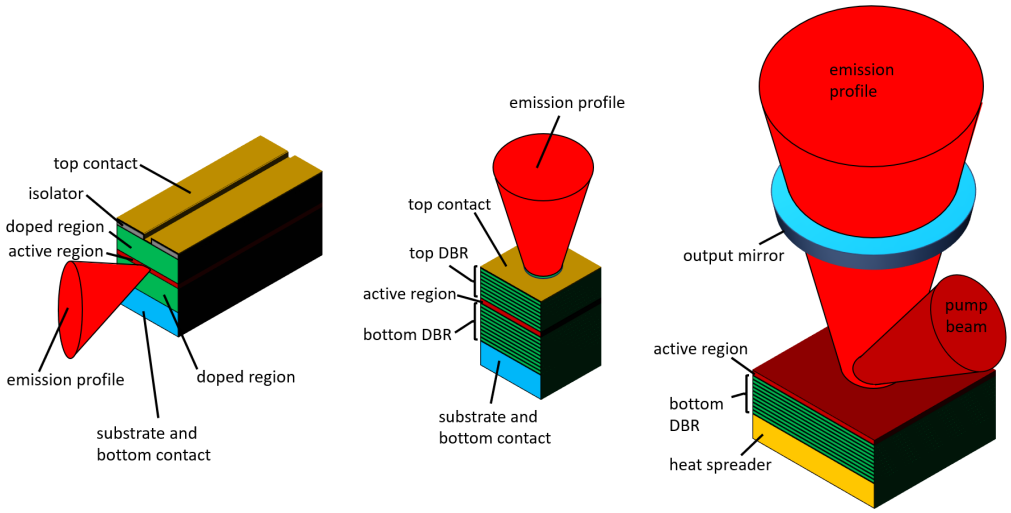

(a) EEL **(b)** VCSEL **(c)** VECSEL

Figure 1.1: Simplified structure of an edge-emitting laser (a), a vertical cavity surface emitting semiconductor laser (b), and the structural setup of a vertical external cavity surface emitting semiconductor laser (c).

VCSEL devices are spectrally pure in comparison with most edge emitting approaches, but the gain and total output power are limited by thermal conductivity of the epitaxially grown distributed Bragg reflector (DBR), and the short gain length (typically $< 3\,\mu m$ optical thickness). In order to increase the power deposited for stimulated emission without reaching critical temperatures in the gain material, further enlargement of the active area and improvement of the heat sinking are desired. In order to fulfill a sufficient transverse filtering for single transverse mode resonance in this scaling method, longer cavities with well-defined resonance quality are required. Another drawback of increased active area is the non-uniform distribution of current guided through the active area, so that optical pumping of the structure is advised. In 1997, Mike Kuznetsov from MIT Lincoln Laboratories presented a fundamental paper, first demonstrating a laser Diode-Pumped Vertical External-Cavity Surface-Emitting Semiconductor Laser (VECSEL or DPSSL) [25]. In this approach, the pump is absorbed in AlGaAs barriers and the excited carriers are diffused into the Quantum Well layers. The first demonstration showed 0.5 W of TEM_{00} output power. Further improvements of heat sinking (back side and intra-cavity diamond heat spreaders) and resonator setup lead to output powers in

excess of 100 W up to now [26], but operation in single transverse and longitudinal mode could not be achieved at this power level, due to the required cavity length with narrow longitudinal mode separation and thermo-optical distortions.

1.4 MECSEL

In order to increase the thermal conductivity from the gain area into the heatsink, and to overcome the bandwidth limitation of epitaxially grown DBRs, the groups led by Mansoor Sheik-Bahae (University of New Mexico) and Peter Michler (University of Stuttgart) worked on operating vertical gain structures without DBR. In the first approaches, the gain structure alone was grown on a GaAs substrate, which was completely removed. The gain structure, less than 1 µm thick, was transferred to transparent single crystal diamond from a floating state in alcohol. Mansoor et al. were the first to report lasing operation with 2.5 W achieved at a center wavelength of 1160 nm, with a so far unachieved tuning range of 78 nm [27]. A year later, Michler et al. reported almost 0.6 W from an AlGaInP-based system at 657 nm and named this new approach Semiconductor Membrane External-Cavity Surface-Emitting Laser (MECSEL). Though the results were very encouraging, the process of transferring the floating membranes to diamond had a very low yield, which improved significantly after direct waferbonding to Silicon Carbide (SiC) was demonstrated [28]. By now, up to 28 W of output power have been demonstrated with MECSEL technology [29]. So far, none of these demonstrations could show single longitudinal mode operation with significant (>1 GHz) mode-hop-free tuning.

1.5 Optical Tweezers and Laser Cooling

Manipulation of the velocity of small particles by laser radiation has been described by Ashkin as far back as 1970 [30]. In this paper, both the acceleration of particles and optical trapping are explained.

Figure 1.2 depicts this phenomenon. When a light beam passes through a small sphere (beam a or b) at an off-center axis, the resulting reflection and deflection

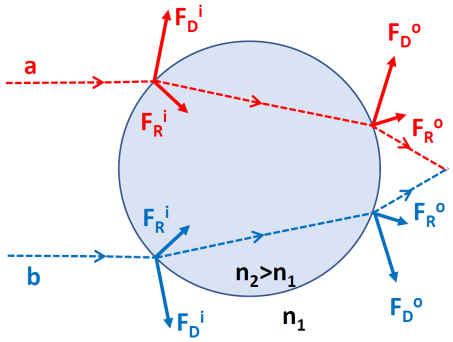

Figure 1.2: Radiation forces of laser light passing through a small sphere

radiation forces at the entrance (F_D^i and F_D^i) and at the exit surface (F_D^o and F_D^o) are depicted for a laser beam traveling from left to right. Following the path of beam a (red) in figure 1.2, the vertical components of F_R^i and F_R^o almost cancel out, while the vertical components of F_D^i and F_D^o act upwards. All four forces partially point in the travel direction of the laser light. Hence, for beam a, there is acceleration upwards and right, while for beam b, the acceleration would be downwards and to the right. Considering that the laser beam has higher intensity at position a compared to b, the sphere would be accelerated upwards. Since Gaussian beams have the maximum intensity at the center of the beam, the sphere is accelerated toward the beam center when passed by a beam with a Gaussian intensity distribution.

In 1975, both Hänsch and Schawlow [31], and Wineland and Dehmelt [32], proposed using laser radiation for cooling atoms. They describe how laser cooling occurs when optical scattering is excited on the lower half of the Doppler-broadened absorption line. This happens when the temperature-induced velocity is directed away from the travel direction of the exciting laser. After the scattering event, the momentum and energy levels of the atom are reduced, leading to a decrease in temperature. Using this method, the atom can be cooled to a state close to zero Kelvin, where the natural, non-Doppler-broadened linewidth is emitted. Depending on the atom type, this linewidth can be as narrow as 182 kHz (ytterbium, [33]) or 32 MHz (strontium, [34]).

Combining both technologies, clouds of single atoms can be held in a well defined space in a vacuum chamber, while simultaneously being cooled. This is typically

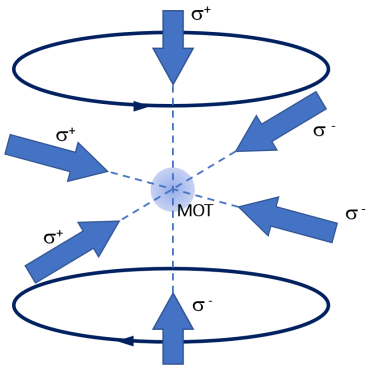

Figure 1.3: Magneto-optical trap

done with six laser beams (which could be three laser beams with a back-reflection mirror). In Magneto-Optical Traps (MOTs), a quadrupole magnetic field provides additional force at the center of the trap to overcome gravitational forces [35]. Figure 1.3 depicts the six laser beam directions and the orientation of the coils with counter-circulating electrical current.

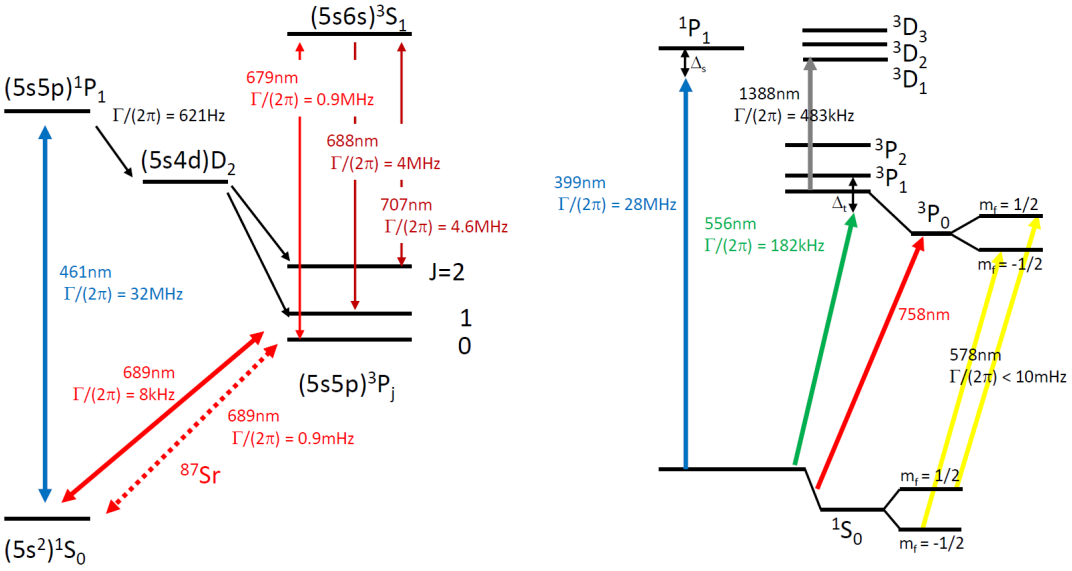

(a) Strontium **(b)** Ytterbium

Figure 1.4: Simplified energy level scheme of strontium and ytterbium showing cooling and repumping transitions, lattice wavelength and clock transitions. Sr data from [36] and Yb data from [37].

The possibility of using lasers to create sub-Kelvin ("ultracold") clouds of atoms, ions and molecules allowed research of Bose-Einstein-condensates and Fermi gases in the 1990s. With the discovery of frequency combs (stabilized mode-locked lasers

with precise mode spacing), ground-state transitions of ultracold atoms could be used as a frequency standard for scientific experiments [38]. While optical probing of an ultracold cesium atom, for instance, gives a 100-fold improvement in frequency accuracy compared to a cesium microwave clock, the absolute high frequency of this transition is impractical for electronic counting. Frequency combs can convert this fundamental optical frequency into useful radio frequency ranges, or serve as precise spectroscopic tools in the mid-IR region [39].

Neutral atoms can achieve a higher precision than ions [40]. Two very promising candidates for optical clocks based on neutral atoms are strontium [41] and ytterbium [42]. Figure 1.4 summarizes the key transitions of these atoms. The strong cooling lines of 398.9 nm (ytterbium, 29 MHz linewidth) and 460.9 nm (strontium, 32 MHz linewidth), as well as the narrow cooling line of ytterbium at 555.8 nm (182 kHz linewidth) presents a challenge for existing tapered amplifier technology, where the signal-to-noise ratio (SNR) is limited by the amplified spontaneous emission (ASE) of the amplifier stage.

2

Semiconductor Membrane Lasers

This chapter introduces fundamental Multi-Quantum-Well (MQW) design rules for vertically emitting laser structures. It gives an introduction to MECSEL technology, its advantages and critical parameters required to reach feasible processing conditions. To aid in understanding the relationship between gain, threshold, and output power in relation to the design of Quantum Well structures, theoretical approximations are summarized and compared with experimental measurement data.

2.1 Multi-Quantum Well Design

The Quantum Well structure supporting the semiconductor membrane lasers studied in this work needs to provide sufficient gain to enable stable resonant operation of the laser. In the structure studied in this work, materials from groups III and V of the periodic table are used to form the gain membrane. Within this structure, compositions of gallium, arsenic, and indium form crystalline layers with bandgap energies that support stimulated emission in the near-infrared (NIR) spectral range. The membrane is grown on GaAs wafers using metal-organic vapor-phase epitaxy (MOVPE). As depicted in figure 2.1, the bandgap energy of $In_xGa_{1-x}As$ can be varied to reach equivalent wavelengths from $\sim 900\,\mathrm{nm}$ to $> 3\,\mu\mathrm{m}$ in different compositions.

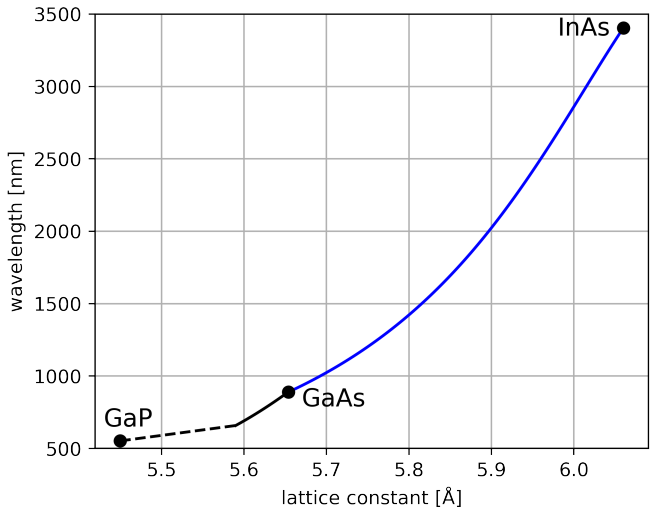

Figure 2.1: Lattice constant and bandgap energy-equivalent wavelength of GaAsP and InGaAs (data from [43]).

To grow a stable crystalline structure on the cubic GaAs substrate, the lattice constant must almost match that of the crystals grown on top. The Indium content of the gain material increases the lattice constant, leading to compressive stress in the gain crystal, which increases with the size of the layers grown on top of the GaAs substrate wafer. To prevent the crystalline structure from breaking or forming stress-reducing dislocations, stress compensation layers are introduced. As depicted in figure 2.1, $GaAs_xP_{1-x}$ layers exert opposite stress compared to $In_xGa_{1-x}As$ when GaAs is used as the substrate material. Based on the target bandgap energy, GaAsP layers can be designed to fully compensate for the total stress in the structure. This "lattice-matched" stress compensation is illustrated in figure 2.2.

In practice, this strain compensation is feasible up to 1 % to 2 % of lattice constant mismatch where crystalline defects become difficult to avoid. This limits the gain wavelength from significantly exceeding 1.2 µm [44]. The total thickness of the crystalline gain layer is as small as several nanometers, which consequently provides only a very small gain per pass ($\sim 10^{-3}$). Considering practical optical losses in the cavity, a single gain element does not allow continuous-wave (cw) lasing in external cavity setups. Hence, multiple stacks of these lattice-matched gain structures are placed on top of each other to increase the net gain of the system.

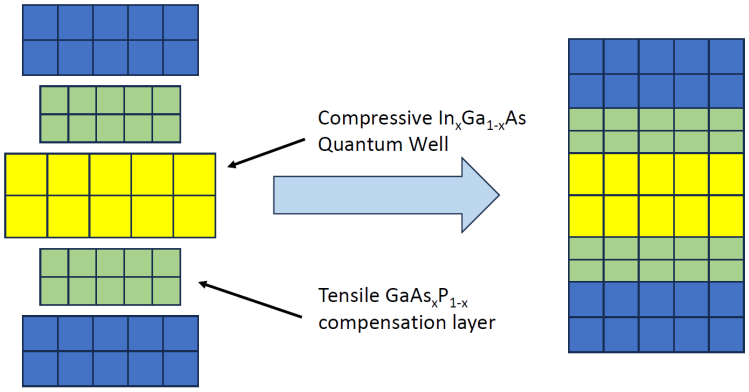

Figure 2.2: Strain compensation of InGaAs Quantum Wells with respect to GaAs (blue) base crystalline structure.

Since the absorption length in the gain crystals is very short (several nanometers thick), the stack is designed in a way that the optical radiation used to pump the stack is absorbed in pure GaAs layers in between the gain stacks. In these so-called "barriers", the pump radiation is absorbed and provides free charge carriers that can diffuse into the crystalline gain layer, which then serves as the Quantum Well for the optical transition. In a standing-wave configuration of the laser system, maximum gain extraction efficiency is reached when the antinodes of the standing wave interference of the resonant radiation coincide with the Quantum Wells. The optical thickness of a barrier/gain system of a multi-Quantum-Well stack is therefore designed to be equal to half of the standing wave wavelength. Section 3.2 provides a detailed description of methods for locking the laser to this resonance.

Figure 2.3 depicts the energy levels in the conduction and valence bands of the system. In order to prevent free charge carriers from diffusing onto the surface of the stack, or material attached to it, a diffusion barrier with higher bandgap energy than all other materials ($In_xGa_{1-x}P$) is being placed at both sides of the stack.

2.2 Operation Principle

The gain material composition and growth techniques of a MECSEL are similar to gain structures used in a Vertical External Cavity Surface Emitting Laser (VECSEL). In a VECSEL setup, one cavity end mirror is epitaxially grown along with the

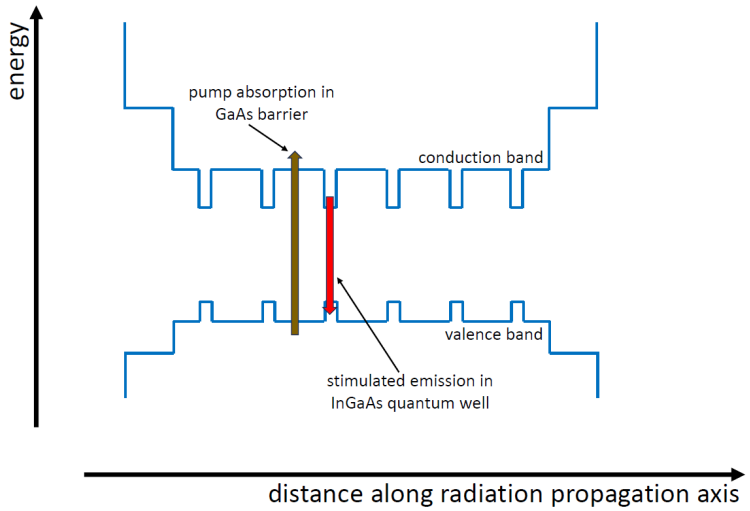

Figure 2.3: Energy diagram, optical pumping and stimulated emission in a multi-Quantum-Well semiconductor membrane.

gain material, or bonded to it. Excess heat is typically extracted through the Bragg-type end mirror into a heat spreading material. Additional heat spreading by transparent material inside the laser cavity has been demonstrated, overcoming the limitations of thermal resistance in the Bragg mirror (described, for instance, by [45]). A MECSEL chip also contains layers that provide optical gain, but no Bragg mirror structures are attached to the gain structure. The gain element is bonded to a transparent heat spreading material on either one or both surfaces and all cavity mirrors are located separately (see figure 2.4). Both VECSEL and MECSEL gain chips typically are attached to a copper mount which is actively cooled. Also, both setups incorporate external means of coupling a portion of the resonant laser light out of the cavity. In the plot, a partially transparent mirror is depicted. Other configurations include intra-cavity nonlinear frequency conversion, where the frequency-converted radiation penetrates through a mirror structure that is transparent to the frequency-converted light.

The gain structures studied in this work contain gallium as a base material, and are grown on a GaAs substrate. Table 2.1 summarizes important thermal parameters of typical materials suited for MECSEL and VECSEL structure design. Comparing GaAs as a mirror component and heat-transmitting medium to silicon carbide (SiC), which can be used as a heat spreading material in MECSEL, the

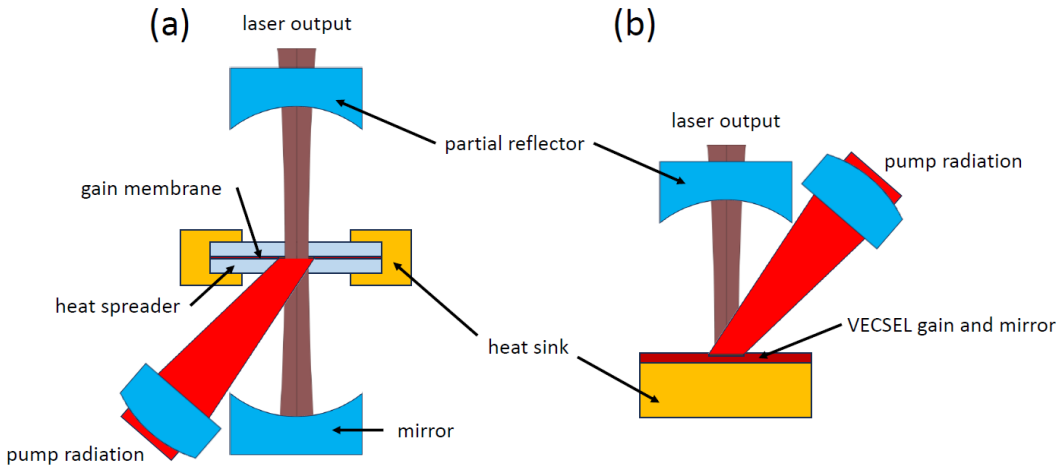

Figure 2.4: Simplified schematic of a MECSEL (a) and a VECSEL (b).

thermal conductivity of Silicon Carbide exceeds that of GaAs by a factor of about ten. Furthermore, the coefficient of thermal expansion (CTE) is better matched with that of GaAs than synthetic diamond and copper. This reduces mechanical shear forces in the gain structure. Reducing these shear forces allows thicker gain structures to be attached and limits the risk of dislocations to form inside the gain stack.

There are several technical advantages of membrane laser operation with external mirrors on both sides. By contacting the heat spreading material directly to the gain stack, the thermal impedance of the epitaxially grown mirror is avoided. Using external mirrors allows for an independent selection of mirror material, avoids the critical bonding process between Bragg mirror and the heat spreader, thereby allowing wafer-scale processing. The absence of thermal impedance through the Bragg mirror has a positive effect on the maximum temperature rise in the pumped region of the gain membrane.

material	thermal conductivity k	CTE α	references
GaAs	$45\,W(m \cdot K)^{-1}$	$5.45 \cdot 10^{-6} K^{-1}$	[46], [47]
silicon carbide 4H	$472\,W(m \cdot K)^{-1}$	$3.09 \cdot 10^{-6} K^{-1}$	[48], [49]
synthetic diamond	$2400\,W(m \cdot K)^{-1}$	$1.0 \cdot 10^{-6} K^{-1}$	[50], [51]
copper 99.95 %	$530\,W(m \cdot K)^{-1}$	$16.91 \cdot 10^{-6} K^{-1}$	[52], [53]

Table 2.1: Physical parameters of heat spreader material at room temperature

In contrast to a VECSEL setup, the resonator mirrors do not need to match

the lattice of the gain material and can therefore be built with a wide selection of materials. This is especially significant for large target reflection bandwidths, since materials from groups III and V offer only limited contrast in the refractive index compared to oxide mirror coatings (with typical mirror materials being GaAs, AlAs, InP and GaInAsP). In a DBR configuration, layers with a high refractive index, n_H, and a low refractive index, n_L, are applied with an optical thickness of a quarter of the target center wavelength. The full-width half-maximum (FWHM) bandwidth is defined by the contrast between n_H and n_L, as described by formula 2.1 [54].

$$\frac{\Delta\lambda}{\lambda} = \frac{4}{\pi}\sin^{-1}\frac{\Delta n}{n_H + n_L} \tag{2.1}$$

The mirror coating layers used in MECSEL configuration can be deposited as oxide material (for instance, SiO_2 , Al_2O_3, MgF_2, Ti_2O_5, Ta_2O_5), which offer significantly higher refractive index contrast in comparison to III-V materials. While oxidation of epitaxially grown layers is possible after growth, this process limits the useable active area due to etching features required for the post-growth oxidation.

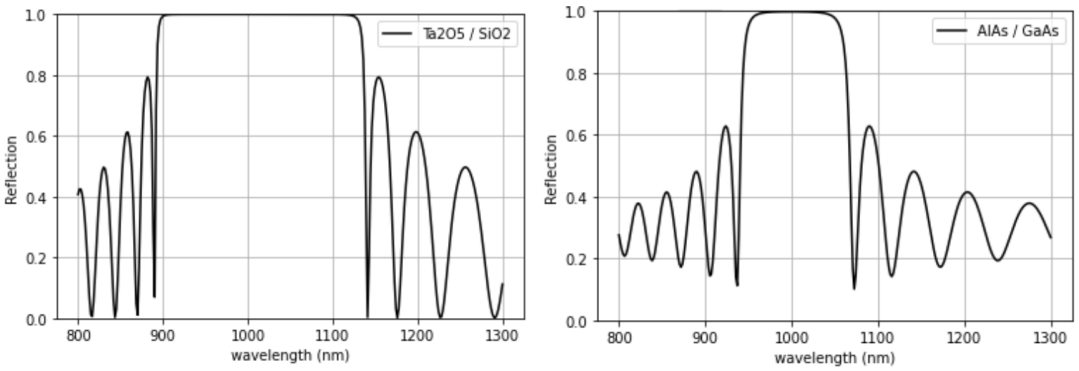

(a) Typical MECSEL mirror **(b)** Typical VECSEL mirror

Figure 2.5: Reflectivity spectrum comparison

Figure 2.5 depicts the reflectivity of an end mirror made of SiO_2 and Ta_2O_5 compared to a VECSEL cavity end mirror made of AlAs and GaAs, monolithically grown on top of the Quantum Well structure. Both cases show a multi-layer Bragg reflector design with 20 pairs of n_L and n_H, each having $\lambda/4$ optical thickness. In these examples, a two-fold increase in available reflectivity bandwidth is achieved.

The dielectric reflector coating can also be applied to the transparent heat spreader, forming (when applied to one side only) a hybrid MECSEL structure (H-MECSEL), which allows the operation of the H-MECSEL chip in configurations very similar to VECSEL designs [29].

2.3 Chip Processing

A major advantage of MECSEL technology is the feasibility of wafer-scale bonding of gain material to a transparent heat spreader. SiC is commercially available with very low surface roughness, and matches the thermal expansion of GaAs-based material well (see table 2.1). Growing only the gain structure without a Bragg mirror mostly preserves the surface quality of the epitaxially grown material and allows for wafer-scale bonding of the gain material by optical contact bonding, where van der Waals forces [55] form a rigid contact.

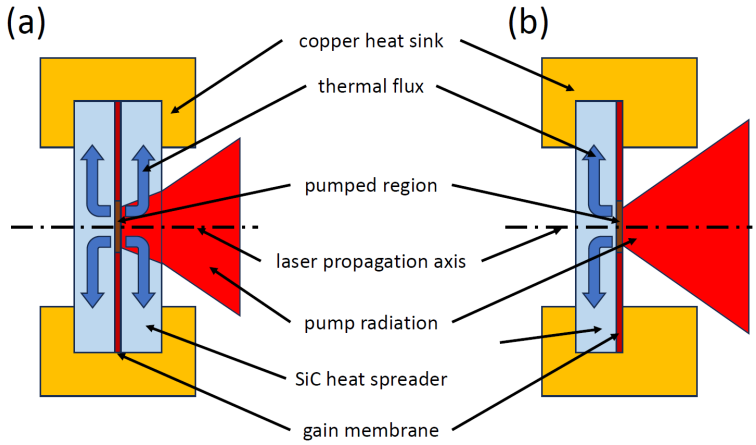

Figure 2.6: Membrane structure with double (a) and single (b) SiC transparent heat spreader

Using low surface roughness Silicon Carbide wafer material, direct bonding of the Multi-Quantum-Well structure to the transparent heat spreader is feasible, and requires no effort other than cleaning and activation steps. Currently, synthetic diamond is not available at wafer scale with suitable surface roughness and transmission properties. Silicon Carbide production and processing was improved by industry to a very high standard, serving the market of high-frequency and high-voltage power

devices [56]. Since the surface roughness of Gallium Nitride (GaN) devices is a key parameter for their performance, this property of commercially available SiC was optimized to a level where van der Waals bonding is feasible at wafer-scale [57].

The MECSEL gain samples studied are processed with either one or two SiC heat spreader plates (bonded to both surfaces of the membrane), each with 500 µm thickness. For operation in an optically pumped laser resonator setup, these are typically held in TEC-cooled copper mounts with Indium foil serving as an adhesion layer. Figure 2.6 shows both configurations, also indicating the heat flow from the optically pumped area to the actively cooled heat sink.

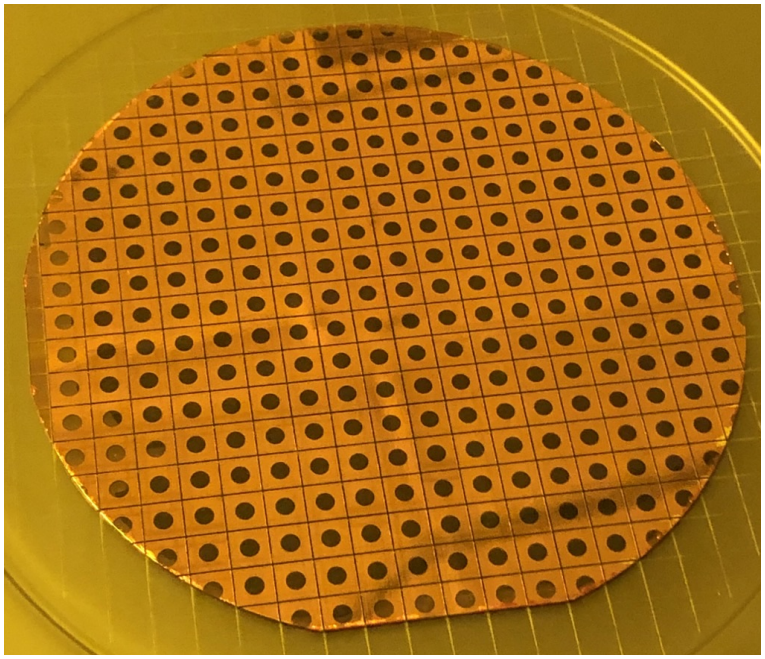

Figure 2.7: Fully processed MECSEL wafer after dicing step.

For the bonding process, parameters used for transferring epitaxially grown crystalline mirrors to fused silica substrates served as a starting point. Applying crystalline Bragg structures to optical substrates enables the production of mirrors with very low phase noise at room temperature operation, since the Brownian motion of the mirror is significantly smaller than that of room-temperature oxide coatings [58].

In order to minimize the amount of handling and cleaning steps of the gain stack, the Silicon Carbide wafer is anti-reflection (AR) coating prior to performing

the optical contact bonding step with the GaAs structure, which was grown in a MOVPE chamber. Both materials are processed as four inch diameter wafers. The material is wet cleaned before bringing the material together. Given the low surface roughness of both GaAs structure and SiC crystal [56], van der Waals bonding does not require significant forces. After bonding, the majority of the GaAs substrate is removed using chemo-mechanical lapping, followed by chemical etching using NH_4OH:H_2O_2:H_2O to completely remove the substrate material until reaching a thin etch stop layer. In configurations using a single heat-spreading SiC wafer, the central area of each chip on the wafer is masked by photolithography, allowing the structure surrounding the active area to be chemically removed. This zone then is metallized with a Titanium as a contact material, Platinum as soldering mate and Gold for oxidation protection. The full wafer is then covered with a protective coating and diced into chips using a diamond wafer saw. This post processing was performed by Thorlabs Crystalline Solutions in Santa Barbara (CA, USA). Over the course of the experiments, many processing steps were optimized in order to maximize the gain and stability of the chips. Figure 2.7 shows a photograph of a fully processed 4-inch diameter wafer with more than 200 diced MECSEL gain chips.

2.4 Gain Stack Design Criteria

Despite the transmission and thermal characteristics of MECSEL chips, and the optimization of the standing wave pattern with regard to the Quantum Well positions in the chip and cavity, many fundamental design rules of VECSEL Multi-Quantum-Well designs can be applied for MECSEL technology. Gain and threshold calculations, the influence of the number of Quantum Wells in the structure, and fundamental material parameters are applicable based on published VECSEL research.

In order to approximate the basic dependencies of design parameters like total thickness of the Quantum Well stack and the number of Quantum Wells with regard to laser output parameters like threshold pump power, slope efficiency and total output power, the derivations provided by [59] have proven to be very

useful. Kuznetsov et al. summarized these fundamental relationships for the case of VECSEL systems. Considering the similarities in Quantum Well stack design, these can serve as a basis for MECSEL system designs. The following relationships do not take thermal effects into account, which becomes evident when comparing experimental data with these approximations at high pump power densities.

In a two-mirror Fabry-Perot resonator, the carrier density N_{th} at lasing threshold is derived from the laser cavity Quality, given by the end mirror reflectivities R_1, R_2 and the round-trip loss transmission factor T_{loss}, where all non-mirror losses are considered. In equation 2.2, a longitudinal confinement factor Γ is introduced for resonant periodic gain structures (RPGs), which is also targeted in the MECSEL configurations discussed in the following chapters. With the Quantum Well thickness L_W (which is designed in relation to the Indium content in InGaAs QWs to achieve the desired gain spectrum), the transparency carrier density (see table 2.2) and an approximated gain coefficient g_0, N_{th} is described in relation to the number of Quantum Wells in the structure N_W [59]:

$$N_{th} = N_0(R_1 R_2 T_{loss})^{-(2\Gamma g_0 N_W L_W)^{-1}} \tag{2.2}$$

From the threshold carrier density, the threshold power can be calculated:

$$P_{th} = N_{th}\frac{h\nu N_W L_W A_{pump}}{\eta_{abs}\tau_{th}} \tag{2.3}$$

Here, the effective pump area A_{pump}, absorbed with an efficiency of η_{abs} is derived from d_{pump} listed in table 2.2, and the pump frequency $\nu = c/\lambda_{pump}$ is considered with the carrier upper-state carrier lifetime τ_{th} at the threshold N_{th}, approximated using the monomolecular, bimolecular and Auger recombination (A, B and C), coefficient is:

$$\tau_{th} = \left(A + BN_{th} + CN_{th}^2\right)^{-1} \tag{2.4}$$

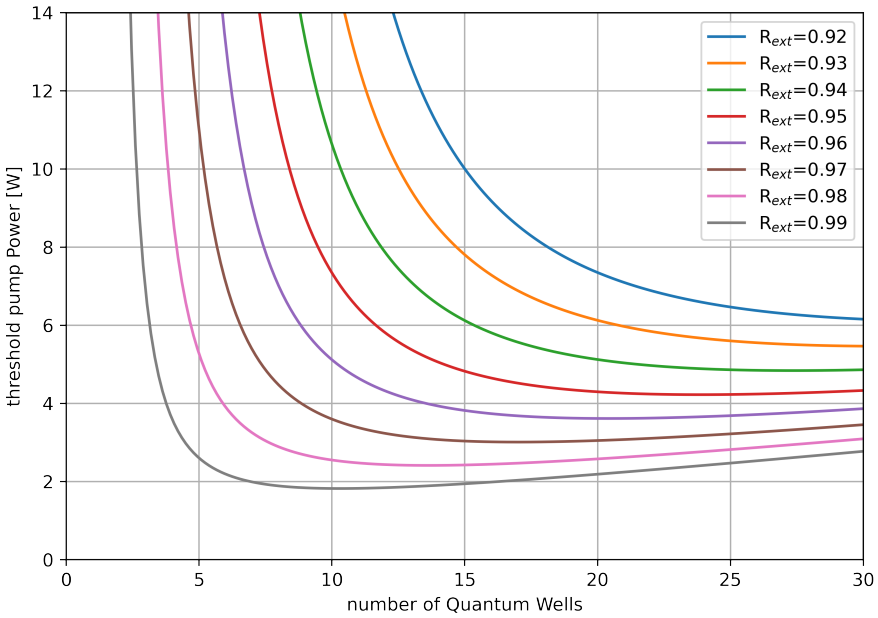

Figure 2.8: Theoretical threshold pump power with respect to the number of Quantum Wells and output coupling ratio.

Figure 2.8 shows the threshold pump power for different reflectivities of the outcoupling resonator mirror, plotted against the number of Quantum Wells. The calculation is based on the parameters summarized in table 2.2 at the end of this section.

With this analytical basis for approximating the threshold pump power, the output power is calculated as a function of the pump power and the laser differential efficiency η_{diff}, which consists of the output efficiency η_{out} (cavity reflectivities and losses), the quantum efficiency η_q (quantum defect between pump and lasing frequencies) and the absorption efficiency at the pump wavelength η_{abs}. In addition to the form published in [59], a radiative efficiency η_{rad} is introduced by Kuznetsov in [60]:

$$\eta_q = \frac{\lambda_{pump}}{\lambda_{laser}} \tag{2.5}$$

$$\eta_{out} = \frac{\ln(R_2)}{\ln(R_1 R_2 T_{loss})} \tag{2.6}$$

$$\eta_{rad} = \frac{BN_{th}}{A + BN_{th} + CN_{th}^2} \tag{2.7}$$

$$\eta_{diff} = \eta_{out}\eta_{quant}\eta_{rad}\eta_{abs} \tag{2.8}$$

Summarizing these efficiencies, a simple form of output power calculation is provided in equation 2.9:

$$P_{las} = (P_p - P_{th})\eta_{diff}. \tag{2.9}$$

In a representative configuration, the output power as a function of the number of Quantum Wells is is shown for different output coupling mirror reflectivities in figure 2.9.

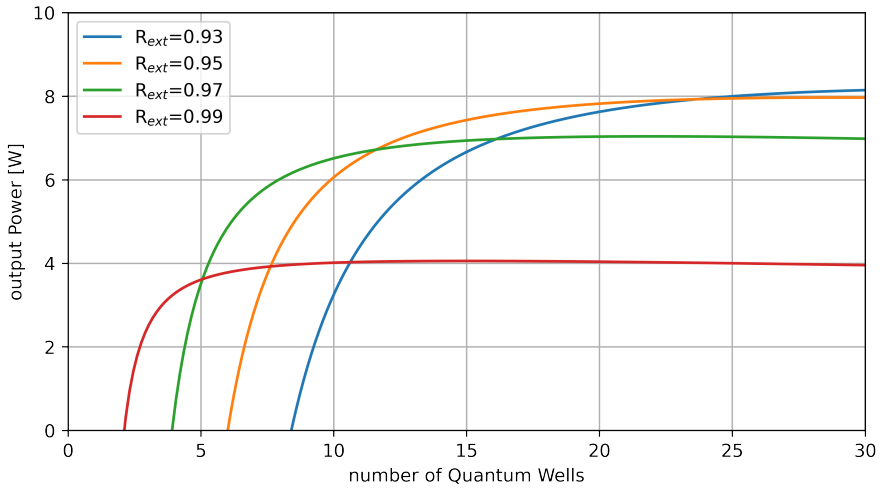

Figure 2.9: Theoretical output power at 25 W pump power with respect to the number of Quantum Wells and output coupling ratio.

Based on these approximations, the theoretical results were compared with experimental data from a simple MECSEL two-mirror Fabry-Perot cavity with an output coupling mirror of $R_{out} = 97\,\%$ at 1060 nm. The cavity was set up as a confocal cavity with two $R = 100\,\text{mm}$ concave mirrors (Laseroptik GmbH, custom) with a MECSEL chip containing a periodic set of eleven Quantum Wells, spaced at

half-wavelength distance. Its InGaAs Quantum Wells are designed to provide an emission of near 1060 nm. SiC heat spreaders, 500 m thick, were bonded on both sides of the membrane gain stack, stabilized at 18 °C using an indium foil interface (100 µm thickness) to a copper heat spreader and TEC cooling (Thorlabs ITC4020). The gain was centered in the cavity and aligned perpendicular to the lasing axis. The chip was pumped with a $d_{pump} \approx 330$ µm pump spot of 808 nm, arising from a 105 µm core diameter fiber-coupled pump source (bwt K808DA5RN40.00W) providing a maximum output power of 40 W. The pump fiber was collimated with an $f = 8$ mm collimator (Thorlabs F240SMA-780) and focused with an $f = 25$ mm lens (Thorlabs LA1560-AB-ML) at an incidence angle of approximately 15 °.

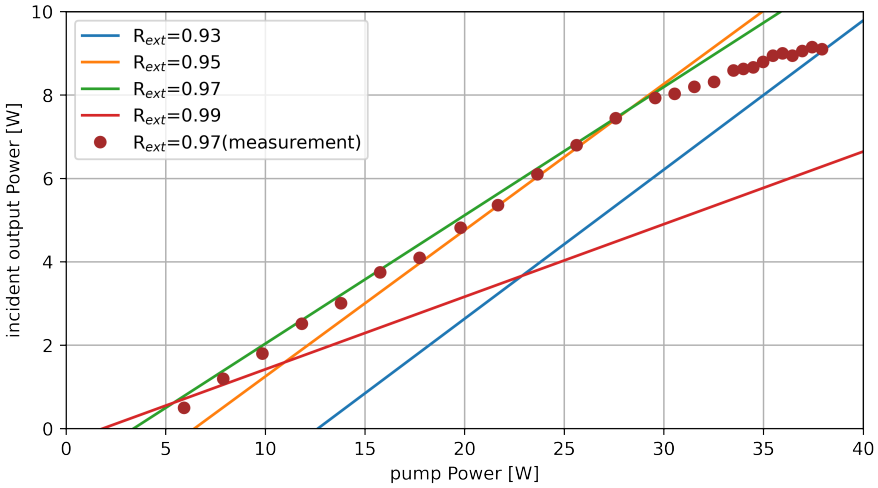

Figure 2.10: Theoretical output power slopes with respect to output coupling ratio compared with experimental results of MECSEL emission at 1060 nm with 97 % output coupling mirror.

At lower pump powers, the analytical values are in very good agreement with the theoretical data (derived from data published in [60]), depicted in the comparison shown in figure 2.10. In the graphical comparison, it becomes evident that the model described in this chapter is insufficient for conditions that induce significant heating of the gain structure. The model does not incorporate heating effects that reduce lasing efficiency and lead to "thermal rollover", starting in this example at pump powers below 30 W.

Parameter	Description	Value
g_0	Material gain coefficient	$2000\,\mathrm{cm}^{-1}$
N_0	Transparency carrier density	$1.7 \cdot 10^{18}\,\mathrm{cm}^{-3}$
Γ	RPG longitudinal confinement factor	2
L_w	Quantum well thickness	8 nm
T_{loss}	Round-trip transmission factor	0.99
λ_{laser}	Laser wavelength	1060 nm
λ_{pump}	Pump wavelength	808 nm
d_{pump}	Pump diameter	330 µm
η_{abs}	Pump absorption efficiency	0.85
A	Monomolecular recombination coefficient	$1 \cdot 10^{7}\,\mathrm{s}^{-1}$
B	Bimolecular recombination coefficient	$1 \cdot 10^{-10}\,\mathrm{cm}^{3}\mathrm{s}^{-1}$
C	Auger recombination coefficient	$1 \cdot 6^{-10}\,\mathrm{cm}^{6}\mathrm{s}^{-1}$

Table 2.2: Laser and material parameters for power and threshold approximation; all values except pump parameters and emission wavelength from [59].

These theoretical approximations, derived from previous VECSEL work, provide useful guidance to the design of the gain stack for MECSEL resonators.

3

Single-Frequency MECSEL Cavity

In this chapter, frequency filtering with birefringent filters and etalons is introduced, targeting single longitudinal mode operation of MECSEL setups. Coupled-cavities theory is summarized and applied to practical three-mirror Fabry-Perot MECSEL-laser design, followed by introducing a matrix method for the longitudinal computation of many-element optical systems. Another matrix method, used for the transverse optimization and description of laser radiation resonance in a cavity, is introduced and birefringent distortion within the gain element is covered. A cavity layout is proposed and analyzed concerning the lateral and efficiency performance. Single-frequency operation and continuous tuning are presented, along with a description of phenomena that increase the need for relatively large contrast longitudinal mode selection.

3.1 Frequency Filtering

In Quantum Well laser operation, the wells support optical transitions in various quantized states. Depending on the width of the Quantum Wells, these optical transitions can have relatively large energy difference, resulting in a broad gain spectrum of MECSEL chips. As an example, a $\lambda = 1112\,\mathrm{nm}$ centered InGaAs device with 22 Quantum Wells supports a full-width half-maximum (FWHM) range of

46 nm. In figure 3.1, the normalized output power measured at different tuning states is shown. This spectrum was determined in a linear two-mirror laser cavity with birefringent tuning, as described below. For the required $\Delta\nu < 100$kHz (or $\Delta\lambda < 0.4$ fm, see Equation 3.1) linewidth of the system, while targeting applications in laser cooling in the output power range of 1 W, several frequency-selective elements need to be included in the system.

$$\Delta\lambda = \Delta\nu\frac{\lambda^2}{c} \tag{3.1}$$

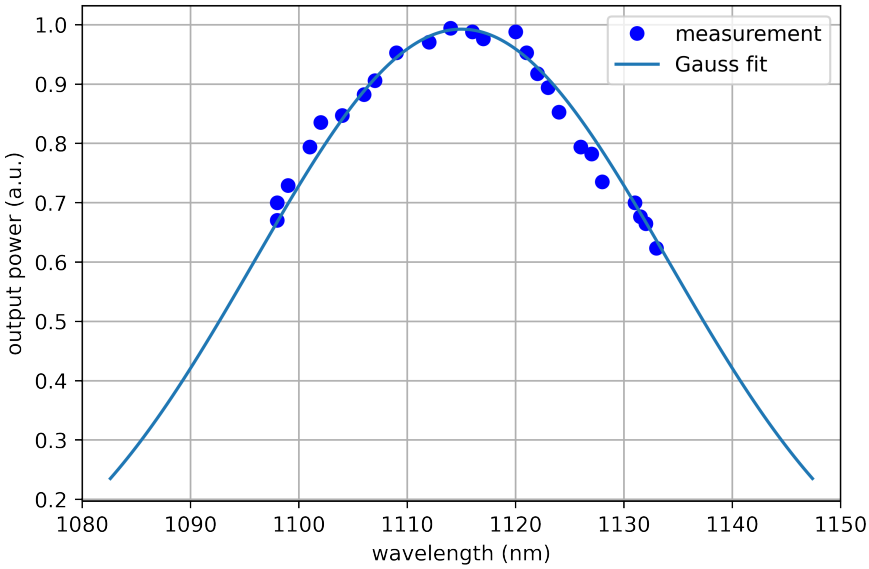

Figure 3.1: Normalized output power of a simple MECSEL linear laser tuned with a birefringent filter.

3.1.1 Birefringent Filtering

A versatile way of filtering polarized free-space lasers is the use of birefringent filters. These typically uniaxial crystals can be used as frequency-selective elements in combination with polarization filtering. They can be used at Brewster angle inside a laser cavity to simultaneously provide polarization filtering and wavelength selection. In the MECSEL setups, polarization filtering is required for efficient nonlinear interaction (see section 5.1), since apart from thermally induced birefringence

(compare section 3.3.2), the optical gain of the MECSEL chip assembly provides no polarization-dependent properties for perpendicular radiation incidence. For the MECSEL experiments in this work, the birefringent filter is used at Brewster angle inside the crystal $\beta = \tan^{-1}(\frac{n_2}{n_1})$, where n_1 is the refractive index of the surrounding environment and n_2 is the effective refractive index of the birefringent crystal at given incident polarization.

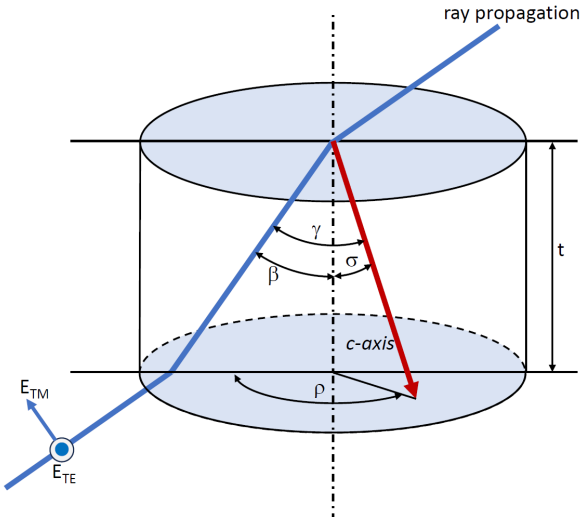

Figure 3.2: Light ray propagating through a birefringent crystal at an arbitrary angle of incidence, with the refraction angle of β, σ representing the tilt of the optic c-axis of the crystal with respect to the surface normal, the crystal axis rotation around the surface normal ρ, γ representing the angle between the ray propagation axis and c-axis, and a thickness t.

When propagating through the crystal, the incident ray experiences a relative phase change $\Delta\phi$ between extraordinary (TE) and ordinary (TM) polarization. A common mathematical description of birefringent filter properties at arbitrary angles of incidence is found in [61]. Following the argumentation of [62], this is a suitable approximation when the ratio between the ordinary refractive index n_o and the extraordinary refractive index n_e is significant:

$$\Delta\phi = \frac{2\pi}{\lambda}\frac{t}{\cos\beta}(n_e - n_o)\sin^2\gamma. \tag{3.2}$$

The internal angle, typically the Brewster angle, is represented by β. The angle θ is defined between the p-polarized unit vector inside the plate and the ordinary

unit vector inside the birefringent material:

$$\theta = \cos^{-1}\left(-\frac{\sin\sigma\sin\rho}{\sin\gamma}\right). \tag{3.3}$$

The crystal axis rotation around the surface normal ρ and the tilt angle of the optical c-axis of the birefringent crystal σ is described by the relative angle γ between the propagation axis and the c-axis:

$$\gamma = \cos^{-1}\Big(\cos\beta\cos\sigma + \sin\beta\sin\sigma\cos\rho\Big), \text{ and} \tag{3.4}$$

$$\gamma = \cos^{-1}\left(\cos\beta\cos\rho + \sin\beta\sin\sigma\cos\rho\right). \tag{3.5}$$

In order to calculate the influence of birefringence and polarization dependent loss, the use of Jones calculus is very convenient. For the simplest case, where a birefringent filter is used at an angle with respect to a single polarization state, the electric output fields in both polarization states, $E_{p,out}$ and $E_{s,out}$ can be obtained by matrix multiplication of a Jones Matrix representing the loss $M_{BRF_{loss}}$ of the s-polarization at a single surface and the transmission matrix M_{BRF} through the birefringent material ([63], [64]):

$$\begin{bmatrix} E_{p,out} \\ E_{s,out} \end{bmatrix} = M_{BRF_{loss}} \times M_{BRF} \times M_{BRF_{loss}} \times \begin{bmatrix} E_{p,in} \\ E_{p,in} \end{bmatrix}, \text{ where} \tag{3.6}$$

$$M_{BRF_{loss}} = \begin{bmatrix} 1 & 0 \\ 0 & q \end{bmatrix}, and \tag{3.7}$$

$$M_{BRF} = \begin{bmatrix} \cos^2\theta + \sin^2\left(\theta e^{i\Delta\phi}\right) & \cos(\theta) + \sin\theta\left(e^{i\Delta\phi} - 1\right) \\ \cos(\theta) + \sin\theta\left(e^{i\Delta\phi} - 1\right) & \sin^2\theta + \cos^2\left(\theta e^{i\Delta\phi}\right) \end{bmatrix}. \tag{3.8}$$

In Equation 3.7, q represents the loss parameter, calculated from the average refractive index as $q = 2n/(n^2+1)$ when operating the filter at the Brewster

angle. As an example, the transmission of a crystalline Quartz birefringent filter of $t = 5\text{mm}$ at the Brewster angle, with $\sigma = 90°$ and $\rho = 40°$ is plotted in figure 3.3. The Sellmeier coefficients are taken from [65].

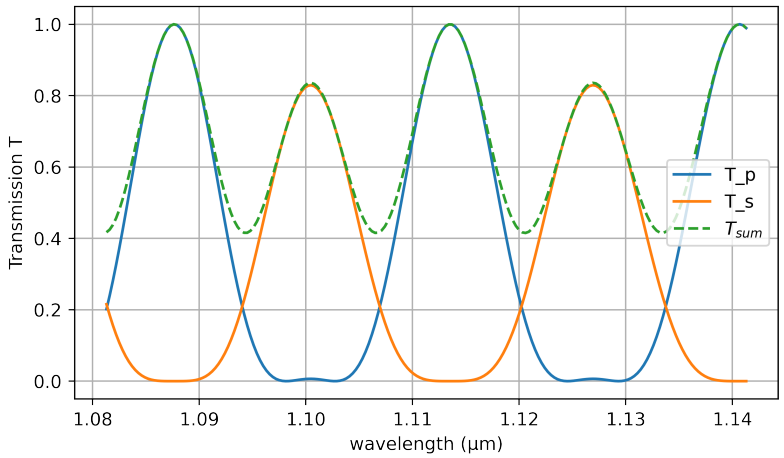

Figure 3.3: S-polarized, p-polarized and sum output of p-polarized radiation after passing a crystalline quartz birefringent filter of $t = 5$ mm at Brewster angle, with $\sigma = 90°$ and $\rho = 40°$.

Figure 3.3 depicts how p-polarized light passes through a birefringent filter, plotted for wavelengths around 1.05 µm. At certain wavelengths, full transmission in p-polarization occurs, while other wavelengths are suppressed. The free spectral range of the birefringent filter (FSR_{BRF}, the range in between two transmission maxima) is one important parameter for choosing the proper crystal material and dimension. This parameter can also be calculated from the parameters described above, without using Jones calculus, as shown in Equation 3.9 [66].

$$FSR_{BRF} = \frac{\lambda^2 \cos\beta}{t\Delta n \sin^2\gamma}. \tag{3.9}$$

The filter function can be spectrally tuned by rotation of the birefringent crystal around ρ, while maintaining Brewster condition. Figure 3.4 shows the sum of s- and p-polarization transmission values for incident p-polarization at various tuning angles. In order to maximize the FSR of the filter at a given thickness, the crystalline c-axis needs to be perpendicular to the propagation direction of the light passing

through the crystal. In the experiments of this work, however, all crystals are cut with the c-axis parallel to the incident surface, which still provides significant birefringent contrast. The crystal parameters need to be selected so that the FSR of the filter sufficiently exceeds the accessible tuning bandwidth of the gain material.

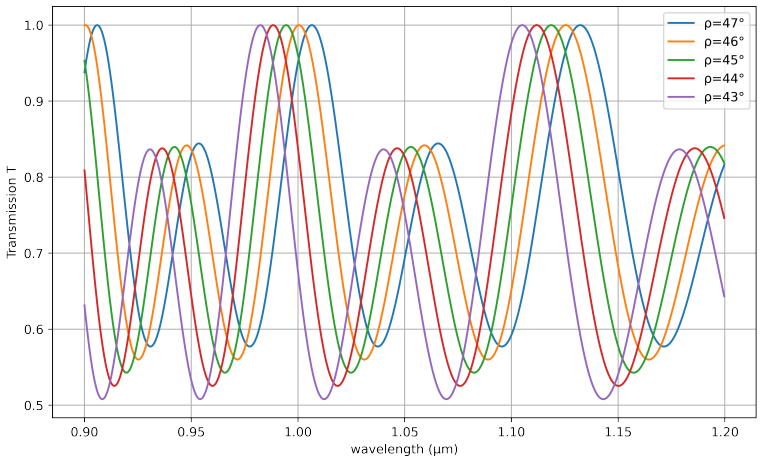

Figure 3.4: Sum transmission of p-polarized radiation after passing a crystalline quartz birefringent filter of $t = 5\,\text{mm}$ at Brewster angle, with $\sigma = 90°$ and various angles of ρ.

When choosing a material for the birefringent filter, low absorption at the operating wavelength and environmental stability (sensitivity to humidity for instance) are key parameters. Another important aspect is the total thickness of the crystal. While for the transverse cavity design (see section 3.3), a thin crystal is beneficial for minimizing astigmatism, the interference of multiple reflections inside the crystal needs to be controlled or sufficiently suppressed. For a plano-parallel filter element at an angle, the displacement d of the internal double-reflex for an incidence angle of α is given by

$$d = \frac{t \sin(2\alpha)}{\sqrt{n^2 - \sin^2 \alpha}}. \tag{3.10}$$

By simulating the complex amplitudes of two Gaussian beams, this interference phenomenon is shown in figure 3.3. In this example calculation, the beam diameter (1/e) is equal to the displacement d, with a reflected beam amplitude of 50 %.

Both destructive and constructive interference cases are shown. While this is an exaggerated scenario, it makes the influence of this interference on the shape and center of mass location clear. As a practical rule of thumb, a factor of three between diameter and displacement was incorporated as a minimum.

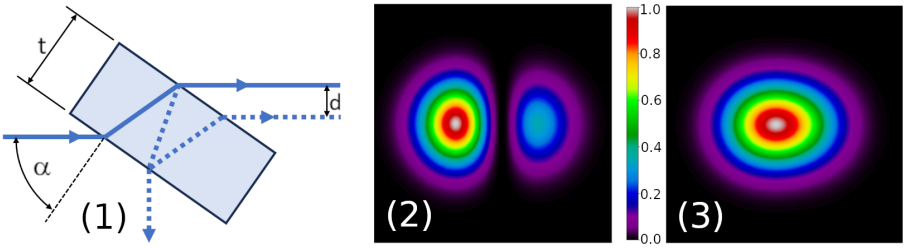

Figure 3.5: Plano-parallel plate with internal reflexes (1) and simulated amplitude distributions, with a beam diameter (1/e) as large as the displacement d, for the cases of destructive (2) and constructive (3) interference.

The same phenomenon needs to be taken into account when considering tilted etalons.

3.1.2 Cavity Modes and Off-Axis Etalon Filtering

Unless noted otherwise, all cavity setups in this work are stable "standing wave" resonators. The term "standing wave" is commonly used, since in a resonator with two fixed ends (cavity end mirrors with reflectivities of R_1 and R_2), interference of the resonant light traveling back and forth leads to a static wave pattern with nodes at the cavity end mirrors. The transmission T (see equations 3.11 and 3.12) of a standing wave cavity, also known as Fabry-Perot interferometer (FPI), is large in resonance condition, where the round-trip phase delay ϕ through the resonator equals a multitude of π. The following formulas are given in [67]. Here, E_i represents the amplitude of the electric field vector on the incident side of the interface, while E_t gives the equivalent amplitude behind the interface.

$$T = \frac{|E_t|^2}{|E_i|^2} = \frac{(1-R_1)(1-R_2)}{\left(1-\sqrt{R_1R_2}\right)^2 + 4\sqrt{R_1R_2}\sin^2\phi}, \text{ where} \tag{3.11}$$

$$\phi = \frac{n\omega L}{c}, \text{ and} \tag{3.12}$$

$$\Delta\nu_{FSR} = \frac{c}{2nL} \tag{3.13}$$

For cases of equal reflectivities of R_1 and R_2, and ideal mode coupling (equal mode shape before and after a round-trip through the cavity), some example transmission spectra are shown in figure 3.6. In cases where $R_1 \neq R_2$, the transmission maxima do not reach the theoretical value of one.

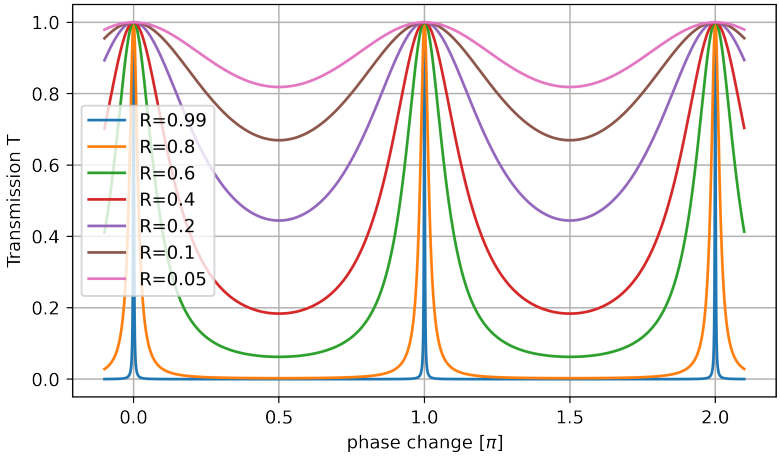

Figure 3.6: Transmission of an etalon with respect to the phase shift ϕ with $R_1 = R_2 = R$.

The FPI formulas are applied to calculate the free spectral range ($\Delta\nu_{FSR}$ in frequency domain) of a standing wave laser cavity, as well as to analyze the influence of tilted etalon filtering, where, for instance, a tilted plano-parallel plate is placed inside a laser cavity.

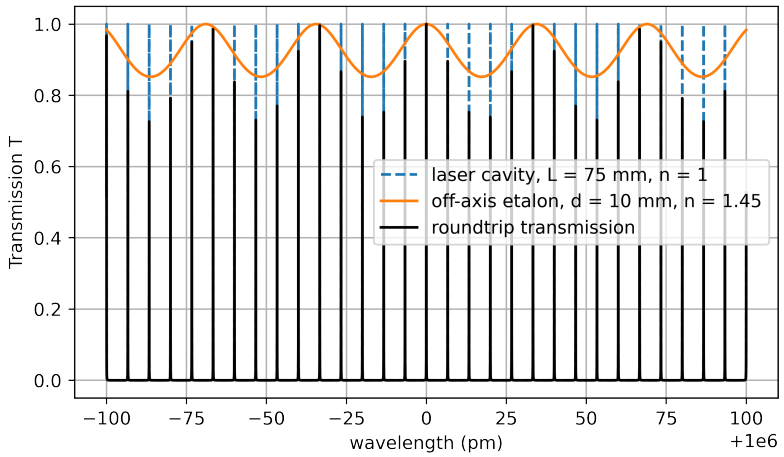

Figure 3.7: Transmission of a 75 mm air-spaced cavity, an etalon filter and the round-trip transmission of both, calculated for a center wavelength of 1 µm.

3.1.3 Coupled Cavity Theory

For optical resonators that include more than two mirrors, several cavities are formed and coupled, interfering with each other. For these cavities, the simple Fabry-Perot interferometer formula (as discussed previously) does not suffice. From transmission matrices (section 3.1.4), equations for the transmission calculation of three- and four-mirror cavities can be derived [68]. For the special case of a three-mirror resonator with interfering reflections, having mirror reflectivities of r_i and mirror transmissions of t_i, the denominator D_3 is determined. This results in the transmission T, with ϕ depending on the lengths between the mirrors in relation to the wavelength of interest:

$$\begin{aligned} D_3 = 1 + (r_1 r_2)^2 + (r_2 r_3)^2 + (r_1 r_3)^2 + 2r_1 r_2 (1 + r_3^2)\cos(2\phi_1) \\ +2r_2 r_3 (1 + r_1^2)\cos(2\phi_2) + 2r_1 r_3 \cos(2\phi_1 + 2\phi_2) \\ +2r_1 (r_2^2) r_3 \cos(2\phi_1 - 2\phi_2) \end{aligned} \tag{3.14}$$

$$T = \frac{(t_1 t_2 t_3)^2}{D_3} \tag{3.15}$$

$$\phi_i = \frac{2\pi L_i}{\lambda} \tag{3.16}$$

A three-mirror cavity offers interesting filter features that are depicted in figure 3.8. Depending on the reflectivity ratio of the three mirrors, a sharp filter function can be achieved. In these examples, the spectral transmission function of a cavity of $R_2 = 30\,\%$ and $R_3 = 98\,\%$ is simulated, with lengths of $L_1 = 60\,\text{mm}$ and $L_2 = (2mm + \lambda/4)$ at a wavelength of $1\,\mu\text{m}$. For this setting, transmission values of $R_1 > 94\,\%$ yield a poor filter function with a multitude of transmission maxima. Values of $R_1 \ll 92\,\%$ yield low total transmission, which, in an active cavity, would lower the quality of the resonator, with low or no resonant power achieved. There is an optimum setting, with maximum suppression of the adjacent cavity modes, around $R_1 \approx 92\,\%$. This is the setting where the center wavelength achieves unity transmission.

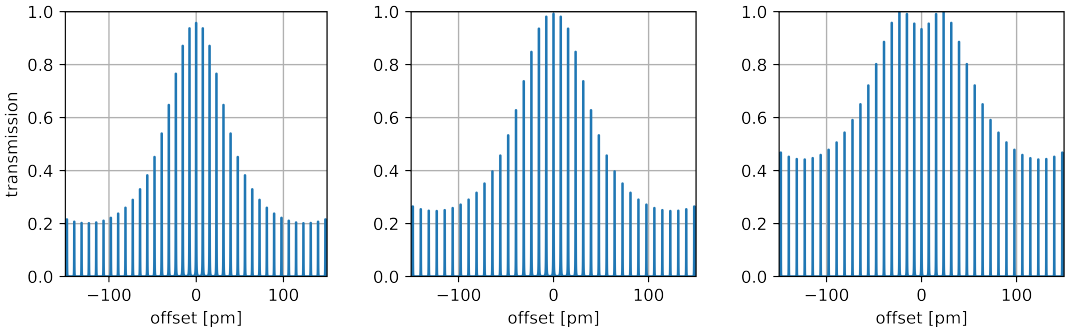

(a) $R_1 = 0.90$ **(b)** $R_1 = 0.92$ **(c)** $R_1 = 0.96$

Figure 3.8: Three-mirror cavity transmission spectra for $R_2 = 30\,\%$ and $R_3 = 98\,\%$, with various reflectivities of R_1. The cavity setup is calculated for a center wavelength of $1\,\mu\text{m}$. The plots show the spectra relative to the center wavelength.

Following the derivation in [68], the reflectivity dependence of the unity transmission can be simplified as:

$$r_{1,unity} = \frac{r_2 - r_3}{1 - r_2 r_3} \tag{3.17}$$

Figure 3.9 depicts the relationship for various reflectivity values of R_3. For unity transmission, very contrasting reflectivity values at the ends of the cavity (R_1 and R_3) are possible. This is a remarkable feature of multi-mirror cavities, since this means that the quality, or enhancement, of the sub-cavities can be designed

toward an optimum in each sub-cavity. In contrast to the well established 2-mirror Fabry-Perot settings, this allows operation of a laser system when only a part of the cavity yields the threshold condition. A coupled cavity may be designed in a way that the gain exceeds the losses in one part of the cavity, while another part of the cavity may introduce a loss that is larger than the gain. Hence, components with relatively large optical transmission losses may be placed inside the cavity part of lower quality and smaller end mirror reflectivity. When carefully chosing the correct ratio of reflectivities, unity transmission (ideal resonance condition) and maximum spectral filtering can be achieved. In figure 3.9, a typical operation point is marked. This setting is being utilized in the work described below. In an idealistic description, the reflectivity values are $R_1 = 92\,\%$, $R_2 = 30\,\%$ and $R_3 = 98\,\%$. In a more realistic consideration, the $8\,\%$ loss at R_1 are the combined "losses" of spectral filtering, scattering and intended nonlinear outcoupling of the cavity. R_3 is affected by thermally induced aberrations. These losses are further described in the following sections.

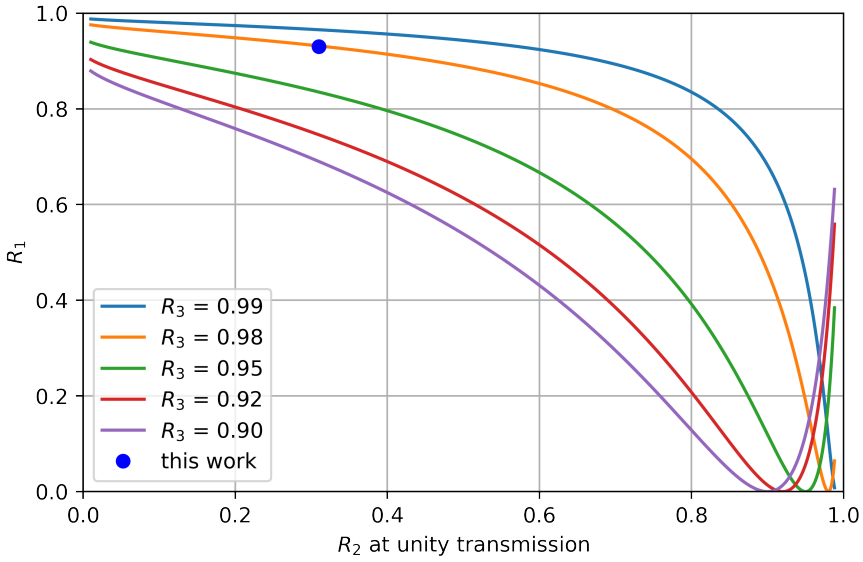

Figure 3.9: Reflectivity relations in a three-mirror Fabry Perot cavity that yield unity transmission. Marked "this work" is the setting that was simulated in the plot before, and was utilized in the experimental work.

3.1.4 Multi-Mirror Cavity Simulation with TMM

In order to better understand the impact of the reflectivity values on the energy density in the sub-cavities, as well as allowing for the simulation of additional (typically undesired) reflections, for instance, from anti-reflection coatings of intra-cavity optical elements, the transmission matrix method (TMM) enables versatile computation. Furthermore, the multi-layer thin-film coatings of the MECSEL and the intensity of the standing wave field around the Quantum Wells can be simulated.

The Transfer Matrix Method (TMM), as described by [69], was utilized in this work. In this approach, the transverse characteristics of the laser radiation are neglected. The optimization in the transverse direction is discussed in section 3.3.

Since this simplification is reduced to a single spatial axis, a simple definition of the travel direction of electromagnetic waves is used. The direction can either be "to the left", indicated by the electric field E_l, or "to the right", indicated by E_r. As depicted in figure 3.10, the material space in between interfaces has a refractive index of $n_0 ... n_m$. This counter is also included in the nomenclature, as well as an indicator of whether the electromagnetic wave is described at the left interface of the material (A) or at the right interface (B). Hence, for instance, a rightward traveling electromagnetic wave at the right-hand side of material 1 is defined as $E_{r_{1B}}$. The physical length of the travel through material with a refractive index n is L_n.

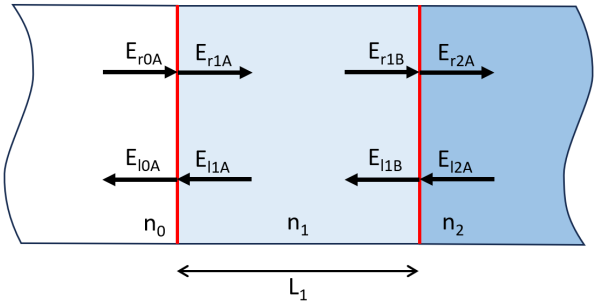

Figure 3.10: Nomenclature for matrix formula

The transition of the electromagnetic field at an interface in both directions, can be written in matrix form, with the transmission matrix D, referring to figure 3.10 at the interface from n_0 to n_1, this is D_{01}:

$$\begin{bmatrix} E_{r_{0A}} \\ E_{l_{0A}} \end{bmatrix} = D_{01} \begin{bmatrix} E_{r_{1A}} \\ E_{l_{1A}} \end{bmatrix}, \tag{3.18}$$

The propagation from interface to interface is defined by the propagation matrix P, again referring to figure 3.10 at the left and right interface of n_1, this is P_1:

$$\begin{bmatrix} E_{r_{1A}} \\ E_{l_{1A}} \end{bmatrix} = P_1 \begin{bmatrix} E_{r_{1B}} \\ E_{l_{1B}} \end{bmatrix} \tag{3.19}$$

In a structure with a number of m layers of different refractive index, the incident electric field E_{in} is equal to $E_{r_{0A}}$, and the reflected field E_{refl} is $E_{l_{0A}}$ and the transmitted field E_{trans} is equal to $E_{r_{mB}}$. Assuming that the light enters only from the left, the electric field entering from the rightmost side of the structure toward the left $E_{l_{mA}}$ is zero. The full transfer matrix M, from the left side of the structure to the right side, can be calculated by multiplying all transmission and propagation matrices from left to right:

$$\begin{bmatrix} E_{r_{0A}} \\ E_{l_{0A}} \end{bmatrix} = M \begin{bmatrix} E_{r_{mA}} \\ E_{l_{mA}} \end{bmatrix}, \text{ or} \tag{3.20}$$

$$\begin{bmatrix} E_{in} \\ E_{refl} \end{bmatrix} = M \begin{bmatrix} E_{trans} \\ 0 \end{bmatrix}, \text{ where} \tag{3.21}$$

$$M = D_{01}P_1D_{12}...D_{(m-2)(m-1)}P_mD_{(m-1)m}. \tag{3.22}$$

From equation 3.21, simple solutions for the relationship between the incoming field and the reflected and transmitted fields can be derived:

$$E_{in} = M_{11}E_{trans} \tag{3.23}$$

$$E_{refl} = M_{21}E_{trans} \tag{3.24}$$

The transmission matrix D at an interface, for instance, D_{01} from n_0 to n_0, accounts for the reflection r_{01}=r_{10} and the transmission t_{01}=t_{10}. For the transition from left to right and right to left, this is:

$$E_{r_{1A}} = t_{01}E_{r_{0A}} + r_{10}E_{l_{1B}} \tag{3.25}$$

$$E_{l_{0A}} = r_{01}E_{r_{0A}} + t_{10}E_{l_{1B}} \tag{3.26}$$

When taking into account that $t_{01}t_{10} - r_{01}r_{10} = 1$, the transmission matrix D_{01} from equations 3.18, 3.25 and 3.26 can be simplified as:

$$\begin{bmatrix} E_{r_{0A}} \\ E_{l_{0A}} \end{bmatrix} = \frac{1}{t_{01}} \begin{bmatrix} 1 & r_{01} \\ r_{01} & 1 \end{bmatrix} \begin{bmatrix} E_{r_{mA}} \\ E_{l_{mA}} \end{bmatrix} \tag{3.27}$$

$$D_{01} = \frac{1}{t_{01}} \begin{bmatrix} 1 & r_{01} \\ r_{01} & 1 \end{bmatrix} \tag{3.28}$$

The propagation matrix P through a medium with the refractive index n, for instance, P_1, propagating through material with n_1, the phase of the electric field is modified. With $k = \frac{2\pi}{\lambda}$, the light at left-hand side (traveling to the right) to the right) can be described as:

$$E_{r_{1A}}(x) = E_0 e^{-j(\omega t - kx)} \tag{3.29}$$

The phase increases by kL, yielding:

$$E_{r_{1A}}(x+L) = E_0 e^{-j(\omega t - k(x+L))} = E_0 e^{-j(\omega t - kx)} e^{-jkL} = E_{r_{1A}}(x) e^{-jkL} \tag{3.30}$$

With L being subtracted from x in the leftward traveling case, the propagation matrix is written as:

$$\begin{bmatrix} E_{r_{1A}} \\ E_{l_{1A}} \end{bmatrix} = \frac{1}{t_{01}} \begin{bmatrix} e^{-jk_1L_1} & 0 \\ 0 & e^{-jk_1L_1} \end{bmatrix} \begin{bmatrix} E_{r_{1B}} \\ E_{l_{1B}} \end{bmatrix}. \tag{3.31}$$

This method is applicable for both parallel (p) and perpendicular (s) polarizations. For an angle of incidence, θ, this is given by:

$$r_s = \frac{n_1\cos(\theta_1) - n_2\cos(\theta_2)}{n_1\cos(\theta_1) + n_2\cos(\theta_2)}, r_p = \frac{n_2\cos(\theta_1) - n_1\cos(\theta_2)}{n_2\cos(\theta_1) + n_1\cos(\theta_2)} \tag{3.32}$$

$$t_s = \frac{2n_1\cos(\theta_1)}{n_1\cos(\theta_1) + n_2\cos(\theta_2)}, t_p = \frac{2n_1\cos(\theta_1)}{n_2\cos(\theta_1) + n_1\cos(\theta_2)} \tag{3.33}$$

All complex reflectivity and transmission calculations throughout this work have been performed using this method. It provides the possibility to compute thin film coating reflectivity spectra, as well as the frequency response of coupled cavity structures in laser resonators.

In order to investigate the power building up inside plano-parallel structures, the normal component of the Poynting vector $\mathbf{S}\cdot\hat{\mathbf{z}}$ can be derived as normalized power from equation 3.33. For better readibility compared to the previous definitions, the fields traveling to the right are defined as E_r, and those in the opposite direction as E_l. For s-polarization, the following relationships are obtained:

$$\mathbf{E} = E_r\hat{\mathbf{y}} + E_l\hat{\mathbf{y}} \tag{3.34}$$

$$\mathbf{H} \propto nE_r(-\cos\theta\hat{\mathbf{x}} + \sin\theta\hat{\mathbf{z}}) + nE_l(\cos\theta\hat{\mathbf{x}} + \sin\theta\hat{\mathbf{z}}) \tag{3.35}$$

$$\mathbf{S}\cdot\hat{\mathbf{z}} = \frac{1}{2}\,\mathrm{Re}\left[\hat{\mathbf{z}}\cdot(\mathbf{E}^*\times\mathbf{H})\right] \propto \mathrm{Re}\left[(E_r^* + E_l^*)\,(E_r - E_l)\,n\cos\theta\right], \tag{3.36}$$

which yields a Poynting vector, normalized to incident power, as:

$$s-polarization: \quad \mathbf{S}\cdot\hat{\mathbf{z}} = \frac{\mathrm{Re}\left[n\cos\theta(E_r^* + E_l^*)(E_r - E_l)\right]}{\mathrm{Re}\left[n_0\cos\theta_0\right]} \tag{3.37}$$

For calculating parallel p-polarization the following relationship is provided:

$$\mathbf{E} = E_r\left(-\sin\theta\hat{\mathbf{z}} + \cos\theta\hat{\mathbf{x}}\right) + E_l\left(-\sin\theta\hat{\mathbf{z}} + \cos\theta\hat{\mathbf{x}}\right) \tag{3.38}$$

$$\mathbf{H} \propto nE_r\hat{\mathbf{y}} + nE_l\hat{\mathbf{y}} \tag{3.39}$$

$$\mathbf{S}\cdot\hat{\mathbf{z}} = \frac{1}{2}\,\mathrm{Re}\left[\hat{\mathbf{z}}\cdot(\mathbf{E}^*\times\mathbf{H})\right] \propto \mathrm{Re}\left[(\cos\theta)^*\left(E_r^* - E_l^*\right)(E_r + E_l)n\cos\theta\right], \tag{3.40}$$

which results in the z-component of the Poynting vector for p-polarization as:

$$\mathbf{S}\cdot\hat{\mathbf{z}} = \frac{\mathrm{Re}\left[n\cos\theta(E_r + E_l)(E_r^* - E_l^*)\right]}{\mathrm{Re}\left[n_0\cos\theta_0^*\right]} \tag{3.41}$$

The Poynting vector distribution along the laser cavity provides crucial information about the enhancement of all sub-resonant cavity parts. As an example, the absolute value of the Poynting vector distribution is calculated, using the same parameters as the simulation of figure 3.8 with $R_1 = 92\,\%$. In figure 3.11, this distribution is shown. In the plot, the limited resolution does not correctly display the sinusoidal standing-wave pattern of the Poynting vector, since the computation sampling rate was lower than the frequency of the resonant light, resulting in undersampled information displayed at a lower frequency. The cavity enhancement is ~ 7.5 in the cavity part with $R_1 = 92\,\%$ and ~ 13.9 in the cavity part with $R_3 = 98\,\%$. Considering an active laser with a gain of $\sim 4\%$, placed in the cavity at R_3, this simplified scheme would permit active laser resonance, since the condition gain $>$ loss is fulfilled. This proves that in a multi-mirror cavity, other parts of the cavity (at R_1 in this example) can introduce losses that exceed the gain ($T_1 = 8\,\%$), while still supporting laser operation above threshold.

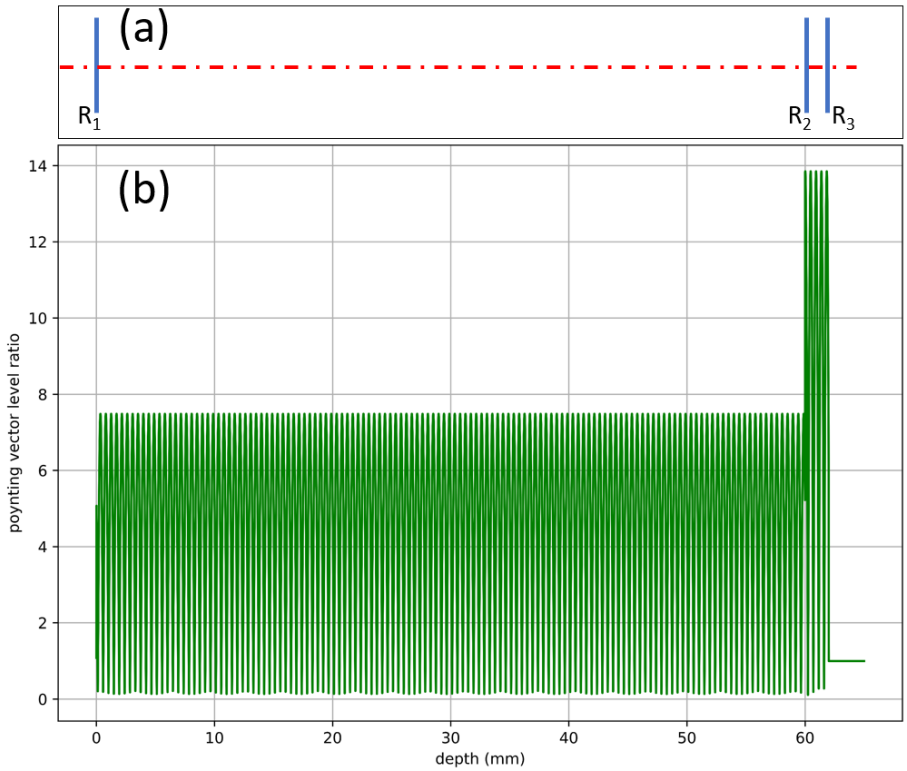

Figure 3.11: (a) Schematic of a three-mirror cavity and (b) relative Poynting vector distribution in an example three-mirror cavity.

3.2 Longitudinal Optimization of a Three-Mirror MECSEL

In order to minimize non-radiative recombination at the outer interfaces of the gain stack, a very thin layer of higher bandgap material is grown at the outer boundaries of the MECSEL gain stack. The gain stack itself is designed in a way that the Quantum Wells, or closely spaced multi-Quantum-Well packets, are placed at an optical distance of half the resonant wavelength. Similar to the resonant periodic gain design approach [70], this allows the anti-nodes of the resonant light to overlap with the thin gain region in the Quantum Wells. The resonant periodic gain design has significant advantages in optimizing the available pump-to-output-power conversion efficiency, as well as minimizing the lasing threshold. The resonance condition, though, can only be ideal for a specific wavelength. Among other parameters, this limits the available gain bandwidth. For the intended applications of this work, where a narrow linewidth at very well defined wavelengths is targeted,

the resonant periodic gain approach offers advantages. In a different target design, the Quantum Well distance could be layed out with a thickness chirp to increase the available wavelength range, but this method has not been investigated.

In VECSEL technology, the Quantum Well stack and one cavity end mirror are monolithically integrated. With the DBR providing a static phase condition and thus defining the position of the anti-nodes relative to the DBR stack, the lateral positions of the Quantum Wells can be designed to exactly overlap. In a MECSEL, where the end mirrors are typically placed with a variable air gap length, the fixed longitudinal position of the anti-nodes needs to be carefully optimized when targeting narrow linewidth, single longitudinal mode operation with high output power stability. One approach is to use the MECSEL chip as an intra-cavity etalon. Due to the limited repeatability of the absolute thickness of the available Silicon Carbide wafers, this approach has significant limitations in MECSEL chip designs, where a transparent heat spreader is placed on both sides of the MECSEL gain stack. It is viable for single heat spreader designs, where the optical thickness of the SiC piece is tuned to an optimum resonance condition through temperature. With the temperature-dependent refractive index $dn/dT = 3.87 \cdot 10^{-5} K^{-1}$ [71], and a thermal expansion coefficient of $\alpha_{33} = 3.09 \cdot 10^{-6} + 2.63 \cdot 10^{-9} T - 1.08 \cdot 10^{-12} T^2 K^{-1}$ [49], an SiC thickness of 500 µm, this yields an optical length change of 19.5 nm/K. Hence, for instance, for a fundamental wavelength of 1127 nm, a temperature tuning of ±14.4 K would be required to fully tune the SiC etalon through the free spectral range by changing the optical pathlength by $\lambda/4$ (see section 3.3.3 for experimental data).

One embodiment that received increased attention in the experiments described in the following chapters is using one semiconductor surface as the middle mirror of a three-mirror cavity. In this arrangement, SiC is only placed on one side of the gain stack, serving as a sufficient heat spreader for Watt-level SLM lasers (experimentally analyzed in section 3.3.3). When the lengths of the two sub-cavities formed in a three-mirror FP setup are well-controlled to allow maximum intracavity power (equivalent to maximum transmission when analysing the passive throughput of the Fabry-Perot setup), then the center mirror has a well-defined longitudinal

relationship to the standing wave pattern of the electric field. To optimize the relative position of the resonant standing field mode in the Fabry-Perot cavity, the computation of the Poynting vector distribution is crucial and can be simulated using the transmission matrix approach described above. For better visibility and simplification of the simulation, the front (R_1) and end mirror (R_3) do not necessarily have to be computed as a DBR stack, though this is easily possible using TMM. Instead, the infinite environmental refractive index at the front can be defined to produce the desired reflectivity through the normal Fresnel reflection.

$$R = \left| \frac{n-1}{n+1} \right|^2 . \tag{3.42}$$

Taking the values of $R_1 = 92\,\%$ and $R_3 = 98\,\%$, the computation is processed with $n_1 = 48$ to represent the front mirror, and $n_3 = 200$ to represent the back mirror. For better visibility of the standing wave's position, the total length of the sub-cavities, as well as the SiC heat spreader is numerically shortened from realistically practical lengths by subtracting an arbitrary number of half wavelengths of optical path length. An example setup, computed by TMM, is depicted in figure 3.12.

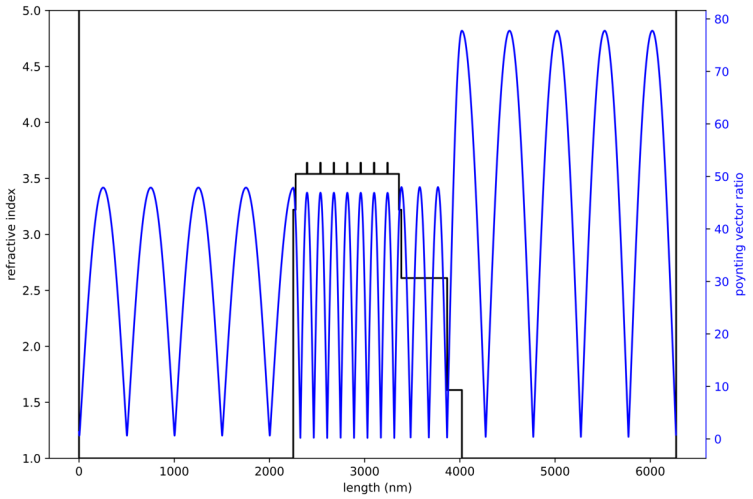

Figure 3.12: Simplified MECSEL three-mirror cavity with anti-nodes of the standing wave electric field overlapping with the Quantum Wells

The plot also shows the refractive index of the material along the shortened laser cavity, so that the seven Quantum Wells are visible as small peaks with the highest

refractive index in the setup. The GaAs barrier, followed by the thin capping layers, are the next lower refractive index materials. The Silicon Carbide heat spreader is attached to the semiconductor stack on the right-hand side, covered with a single anti-reflection layer ($SiNO_x$) with $\lambda/4$ optical thickness.

In the design depicted in figure 3.12, the outer GaAs barriers are tuned in thickness toward ideal overlap with the standing wave pattern. Throughout the optimization of the practical setup, TMM has served as an important tool to help identify parasitic etalon behavior, for instance, with practically non-ideal AR coating on the SiC.

Utilizing these design approaches, a laser was set up and tested for single frequency operation and tunability. More details on the setup are summarized in section 3.3.1. The laser operated in a single longitudinal and transverse mode under all conditions tested within the tuning range of the piezoelectric elements.

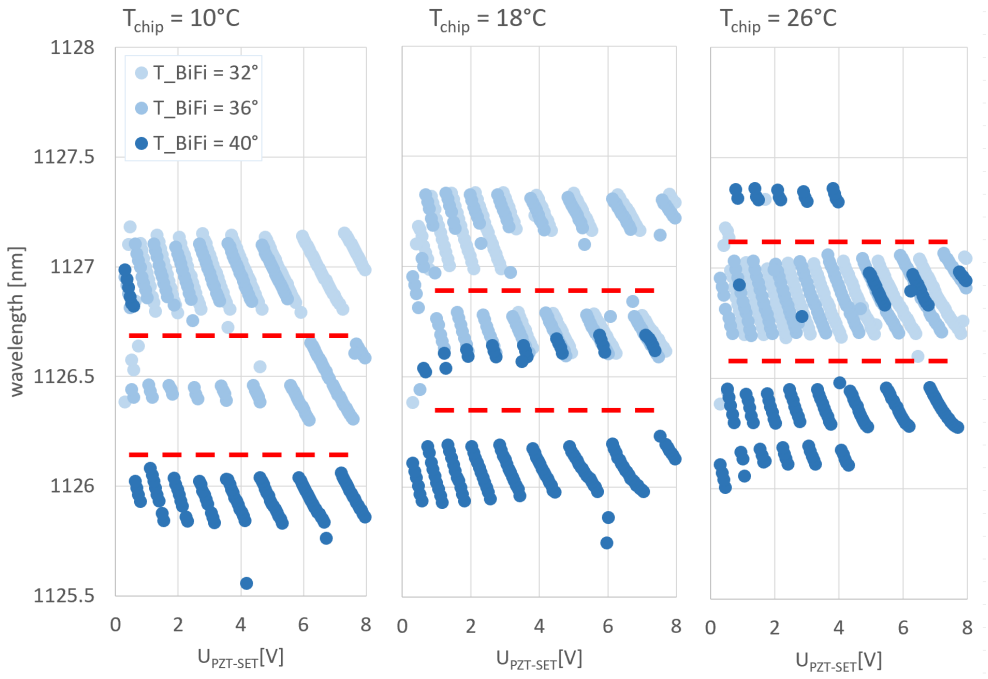

Figure 3.13: Tuning the short etalon arm of a three-mirror cavity shows the impact of SiC temperature in a parasitic etalon formed by residual reflexion off the AR coating on the SiC plate. The dashed red lines show the temperature dependent shift of the etalon spectrum, induced by thermal expansion and the temperature dependent refractive index of SiC.

In figure 3.13, the laser emission wavelengths upon changes of the short cavity

length, with different temperatures of the gain element and birefringent filter crystal are plotted. In the graphs, $U_{PZT\text{-}SET}$ is the set voltage of a high voltage amplifier with an amplification of 150, connected to the cavity-end mirror PZT. The data show that there are wavelength regions where the laser does not emit radiation. Though the Silicon Carbide surface is coated with a dielectric anti-reflective coating, a residual reflection appears to create enough distortion to the transmission profile to disturb seamless wavelength tuning. As indicated by dashed red lines in figure 3.13, the wavelength regions preferred by the practical laser setup depend on temperature and have a well defined free spectral range. Both the free spectral range and the temperature dependence match the results given by the optical path length of the SiC chip and its FSR when considering it acting as an etalon (compare equation 3.13) with the temperature-dependent refractive index of SiC (see table 4.1).

3.3 Transverse Resonator Design

The design and optimization of the transverse resonant laser radiation inside the cavity was performed separately from the longitudinal cavity design described above. In order to maintain longitudinal narrow linewidth operation, the design aim is to operate the laser device very close to the transform limit, with a Hermite-Gaussian TEM_{00} transverse mode. For this free-space laser type, all angles θ_n of the propagation direction with respect to the optical center axis of the cavity are very small. Hence, the paraxial approximation ($\theta \approx \tan\theta \approx \sin\theta$) is used to perform ray tracing and eigenvalue computation using the ABCD matrix representation (see, for instance, [72] and [73]). In this formalism, the beam vector at each optical element is represented by the angle θ_n and a transverse radius of r_n at each element of the optical system. With the $1/e^2$ beam radius w, the wave number $k = 2\pi n\lambda^{-1}$ and the radius of curvature R of the Gaussian beam, the complex beam parameter q [74] at a position z along the beam propagation axis is defined as

$$\frac{1}{q(z)} = \frac{1}{R(z)} - i\frac{\lambda}{\pi w(z)^2}, \text{ with} \tag{3.43}$$

$$R(z) = \mathrm{Re}\left(\frac{1}{q(z)}\right)^{-1}, \text{ and} \tag{3.44}$$

$$w(z) = \sqrt{\frac{\lambda}{\pi\,\mathrm{Im}\left(\frac{1}{q(z)}\right)}}. \tag{3.45}$$

The ABCD matrix approach provides an efficient method of transferring fundamental Gaussian properties through propagation and refracting elements. The most important ABCD elements, that were used in the transverse cavity optimization, are summarized in table 3.1. An individual ABCD matrix can be applied to transfer the beam, defined by the q parameter, as

$$q(z') = \frac{Aq(z) + B}{Cq(z) + D}. \tag{3.46}$$

Description	Matrix	Representation
Tilted Spherical Mirror	$M_T = \begin{bmatrix} 1 & 0 \\ -\frac{2}{R\cos\alpha} & 1 \end{bmatrix}, M_S = \begin{bmatrix} 1 & 0 \\ -\frac{2\cos\alpha}{R} & 1 \end{bmatrix}$	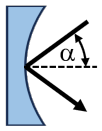
Perpendicular Plate of Matter	$M = \begin{bmatrix} 1 & \frac{d}{n} \\ 0 & 1 \end{bmatrix}$	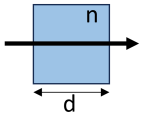
Brewster Plate	$M_T = \begin{bmatrix} 1 & \frac{d\sqrt{n^2+1}}{n^4} \\ 0 & 1 \end{bmatrix}, M_S = \begin{bmatrix} 1 & \frac{d\sqrt{n^2+1}}{n^2} \\ 0 & 1 \end{bmatrix}$	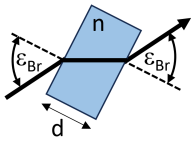
Tilted Thin Lens	$M_T = \begin{bmatrix} 1 & 0 \\ -\frac{1}{F\cos\alpha} & 1 \end{bmatrix}, M_S = \begin{bmatrix} 1 & 0 \\ -\frac{\cos\alpha}{F} & 1 \end{bmatrix}$	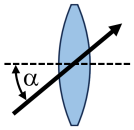

Table 3.1: ABCD matrices for the optical elements required in the cavity calculation [75].

Some elements in table 3.1 have a different impact on the transverse and sagittal direction of the electric field, represented by the individual matrices M_T and M_S.

In cases where the tilt of the object is perpendicular to the direction depicted in table 3.1, the M_T and M_S definitions need to be interchanged.

The ABCD matrix formalism is used to simplify beam propagation in the paraxial approximation by multiplying the matrix elements

$$M = M_N ... M_3 M_2 M_1 \tag{3.47}$$

and then applying the combined matrix M on the input beam parameters.

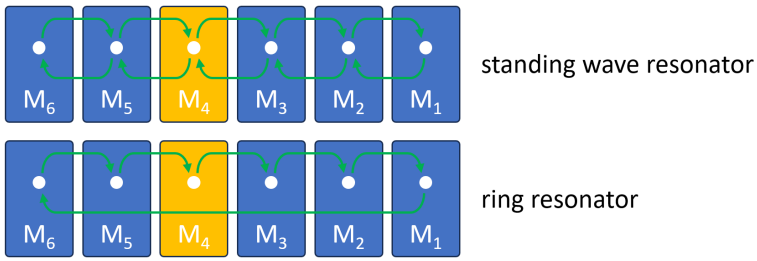

Figure 3.14: Schematic calculation scheme for the round-trip matrix of a standing wave Fabry–Perot cavity and a ring cavity.

This method is utilized in the beam propagation approximations throughout the following chapters. For resonator optimization, the same method can be applied to find the eigenvalues of a stable cavity. To derive these, the round-trip matrix for a cavity needs to be calculated. In a Fabry-Perot cavity, the calculation may start at any optical element, through all elements of the laser cavity to the other end mirror, and back through all elements of the laser cavity in the reverse direction. In a ring-type configuration, the round-trip matrix is calculated by multiplying all matrix elements once (see figure 3.14). From the ABCD elements of this round-trip matrix, the eigenvalue of the resonator can be derived in all cases where the resonator offers a stable solution. This is the case when $|(A + D)/2| \leq 1$. The equation has two solutions, which in stable resonance case are a pair of complex conjugates. In this case, the waist radius at the longitudinal position where the combined matrix M is created is given by:

$$w^2 = \frac{\lambda}{\pi} \frac{2B}{\sqrt{4 - (A + D)^2}}, \tag{3.48}$$

and the radius of the wavefront by

$$R = \frac{2B}{D - A}. \tag{3.49}$$

With these initial parameters, equations 3.43 through 3.45 allow for plotting and analyzing the beam size development (caustic) throughout the resonator.

3.3.1 Design Implementation

The design goal for the cavity setup is dominated by several key aspects: The pump and emission radii at the gain membrane need to be appropriately set to provide an optimum balance between gain creation (dependent on pump power density), maximum temperature (which has a significant impact on laser efficiency) and temperature-induced aberrations leading to acceptable losses (compare chapter 4). While incorporating all necessary frequency filter elements (see chapter 3.1), the cavity should be as short as possible to maximize the free spectral range of the cavity while maintaining transverse single-mode operation. The mode spacing $\Delta\nu$ is inversely proportional to the cavity length L:

$$\Delta\nu = \frac{c}{2L} \tag{3.50}$$

Consequently, a short cavity relieves the requirements for the sharpness of the frequency narrowing elements. The implementation of an intra-cavity frequency doubling element requires a sufficiently small beam waist near the nonlinear crystal (details in chapter 5.1).

Additionally, the transverse mode confinement needs to suffice. This can, in part, be realized by cavity design (sufficiently different from confocal operation), and proper mode matching between the pump beam size and the resonant beam size. When a sufficient portion of the Gaussian beam extends into the unpumped perimeter of the gain membrane, this results in a "soft" aperture. The unpumped region around the optically excited area absorbs the resonant beam and thus can be configured to enforce single transverse mode operation.

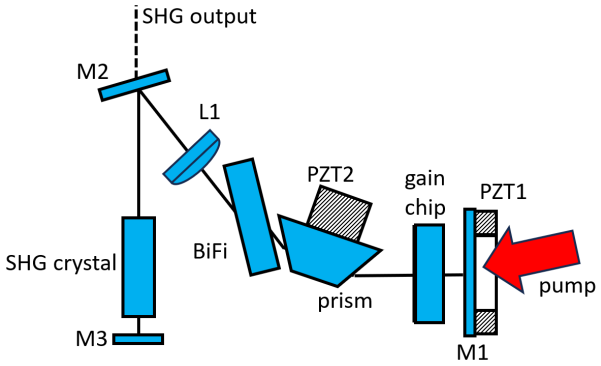

Figure 3.15: MECSEL configuration in a three-mirror design approach with tunable cavity lengths and intra-cavity second harmonic generation.

In a preferred setup, the ratio of cavity lengths in a three-mirror Fabry-Perot configuration is set to approximately 30. The choice of optimum pump beam diameter in the semiconductor gain provided the foundation for the transverse resonator design. The pump beam diameter in the gain membrane should be minimized, in order to minimize the threshold laser power (compare section 2.4). However, the aberrations introduced by the thermal lens, as well as the maximum gain temperature, set a limit to this parameter (see chapter 4 for further details). The pump diameter was set to 395 µm, and based on thermal lens simulations and experiments, a DBR-coated mirror with a convex radius of curvature (ROC) of $R - 750\,\mathrm{mm}$ was chosen to pre-compensate for the thermal lens arising from the pump radiation. Based on this selection, considering the limitation of the required optical path lengths of the birefringent and SHG crystals, a configuration with an intra-cavity lens was optimized using the ABCD approximation. Since the birefringent crystal is used at the Brewster angle, an astigmatism is introduced to the cavity. This is pre-compensated by tilting the intra-cavity lens by several degrees. The intended outcoupling from this resonator is induced by nonlinear frequency conversion, further described in 5.1.

Figure 3.15 depicts the setup that was used throughout further experiments. M1 is convex, while M2 and M3 are plano mirrors (LaserOptik GmbH, custom design). The thin-film coating stack on M1 is designed to transmit the pump radiation well, which is transmitted through this mirror. This mirror is mounted on a ring-type

piezoelectric element (Thorlabs PA44M3K). The gain membrane (various designs) is bonded on one side with 500 µm thick SiC. The SiC itself is coated with an anti-reflection stack to minimize reflections at the fundamental wavelength and the pump wavelength at the interface to air. The gain stack is not AR-coated, so that it provides a significant reflection ($R \approx 30\%$) in the interface to air, which acts as the center mirror in this three-mirror Fabry-Perot resonator configuration. Since M1 is mechanically tunable along the z-axis of the resonator, the filter function of the short-cavity part of the three-mirror configuration can be spectrally tuned.

As depicted in figure 3.15, the length variation of the longer arm of the three-mirror cavity is implemented by shifting a fused Silica prism, cut for Brewster angles of entrance and exit, into and out of the resonant laser beam. This movement changes the optical path length of the resonator, while maintaining the beam position and transmission angle through the prism. This design approach was first implemented in external-cavity resonant frequency doubling (see [76]). It is favored because all piezoelectric elements have not only a longitudinal expansion in the intended direction, but also are prone to angular deformation upon the application of a drive voltage. This angular error scales linearly with the total stroke of the piezoelectric element. Since the prism is a transmissive optical element, a significantly lower angle of piezo-stroke-induced tilt is transferred to the resonant radiation, compared to a mirror mounted on the same PZT.

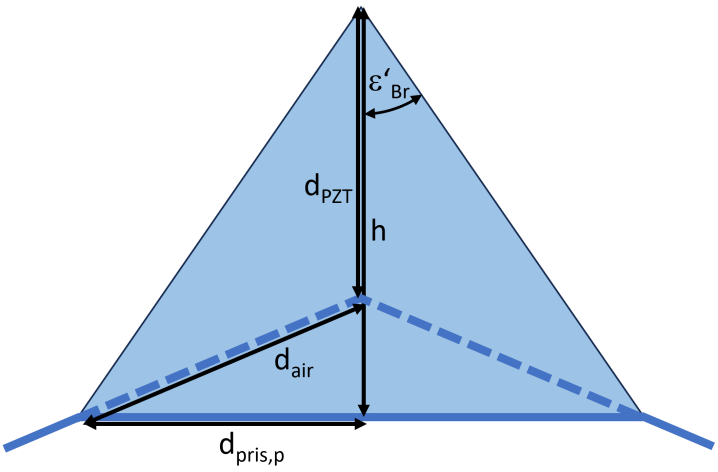

Figure 3.16: Sketch of a Brewster prism for calculation of the optical path length (blue solid line) change upon inward and outward translation of the prism.

For estimation of the tuning range of the long arm, the free spectral range $\Delta\nu_{FSR}$ is calculated with an intra-cavity optical path length of $nL = 75\,\text{mm}$ to be $\Delta\nu_{FSR} = 2.1\,\text{GHz}$ (see equation 3.9), incorporating the refractive indices within the resonator. With an intended mode-hop-free tuning range of $\Delta\nu_{total} = 21\,\text{GHz}$ at the fundamental wavelength, a frequency stroke of approximately $10 \cdot \Delta\nu_{FSR}$ is required. Since the round-trip cavity length (twice the physical cavity length) changes by one resonant wavelength from one transmission maximum to the next, thus, for driving through one FSR, the required stroke of cavity length change $\lambda = 1112\,\text{nm}$ is $\sim 10 \cdot \frac{\lambda}{2}$ in a Fabry-Perot type of cavity. Thus, the optical path length of the cavity needs to be altered by $\Delta nL = 5.5\,\mu\text{m}$. In a prism with Brewster angles for both in- and output, the apex angle α is defined by twice the internal Brewster angle:

$$\alpha = 2\epsilon_{Br'} = 2\tan^{-1}\left(\frac{n_1}{n_2}\right) \tag{3.51}$$

A fused silica prism in air ($n_1 = 1$) with a refractive index of $n_2 = 1.449$ ([77]) needs to be cut to an apex angle of $\alpha = 69.2°$ to achieve this condition (see figure 3.16). When shifting the prism along the height h toward the apex angle, the physical length through which the laser radiation penetrates the prism is defined as $2d_{pris,p}$, which, with equation 3.51 is:

$$\tan\epsilon'_{Br'} = \frac{d_{pris,p}}{h} = \left(\frac{n_1}{n_2}\right) \tag{3.52}$$

The optical path length $2d_{pris,o}$ becomes:

$$d_{pris,o} = hn_1 \tag{3.53}$$

When the prism is tuned out, so that the path length through the prism is infinitesimally small, the equivalent optical path length through air is then $2d_{air}$, defined as:

$$d_{air} = \frac{h n_1}{n_2 \cos\Big(\epsilon_{Br} - \epsilon'_{Br}\Big)} \tag{3.54}$$

The piezo travel d_{PZT} to move the prism from one extreme to the other is:

$$d_{PZT} = h - \tan\Big(\epsilon_{Br} - \epsilon'_{Br}\Big) d_{pris,p} \tag{3.55}$$

Hence, with the refractive index n_2 as given above, the ratio of piezo movement to effective path length change results in

$$\frac{d_{PZT}}{2\Big(d_{pris,o} - d_{air}\Big)} \approx 1.4, \tag{3.56}$$

so that the required piezo travel range is $d_{PZT} = 7.7\,\mu\text{m}$, in practice produced by a 150 V ring PZT stack (Thorlabs PK44RB5P2), which is mounted on a high-density metal rod to improve the dynamic performance of the assembly. The assembly has a resonance frequency of 42 kHz, sufficient to compensate for acoustic impact from the surroundings and the water cooling.

The intra-cavity lens (DD Optik GmbH, custom) is AR-coated for the fundamental resonant wavelength and optimized to achieve transverse resonator stability at a path length from lens to end mirror, that suits the choice of LBO (see chapter 5.1) and leaves sufficient space for the beam to travel over M2, which has a dichroic coating, reflecting the majority of the fundamental light, and offering transparency for the frequency-doubled light.

Figure 3.17 depicts the transverse beam radius under the stable resonator condition along the length of the cavity. The intra-cavity lens is tilted to compensate the astigmatism induced by the Brewster-cut elements. In the figure, this tilt is optimized for a thermal lens of $f_{therm} = 2.5\,\text{dpt}$ refractive power, realizing a symmetric radius in the gain chip at this effective focal length.

The astigmatism induced by the Brewster-cut elements, along with the position and tilt of the intra-cavity lens, is static. The thermal lens, however, depends on

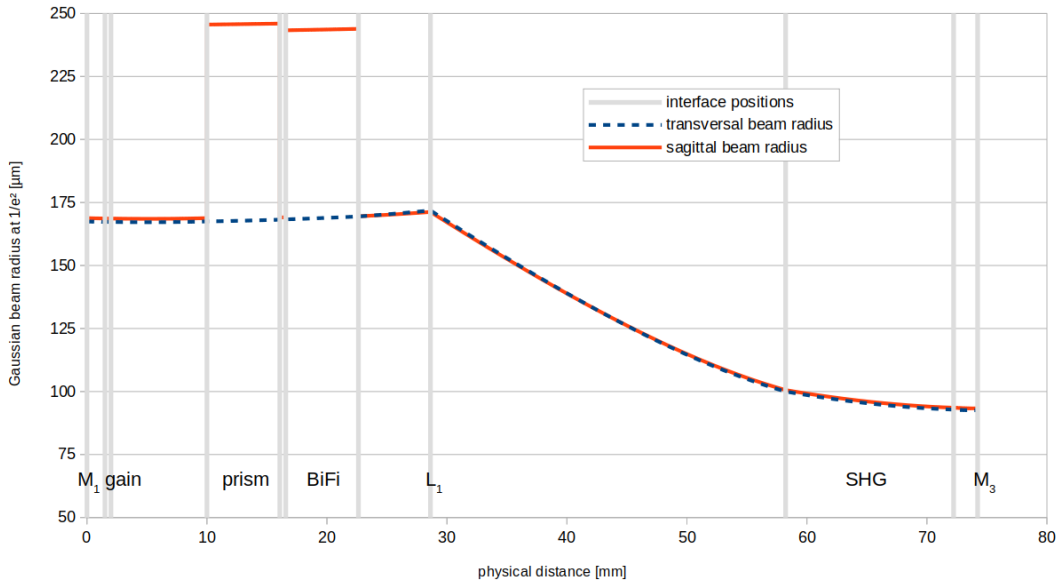

Figure 3.17: Caustic inside the resonator at $f_{therm} = 2.5\,\mathrm{dpt}$ thermal lens refractive power.

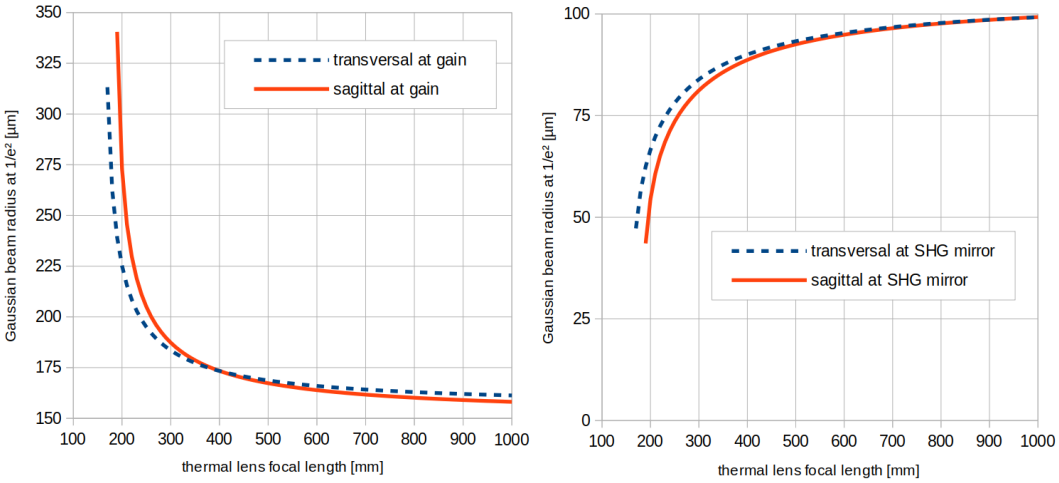

Figure 3.18: Beam radius at the gain membrane (left) and SHG end mirror (right) with variation of the thermal lens focal length.

the applied pump power. In order to evaluate the performance upon modification of the pump power, the beam radius at the gain membrane and the focus position at second harmonic generation (SHG) crystal were computed for various thermal lens refractive powers. Figure 3.18 shows the results. In the chosen setup, the beam size in the gain membrane and SHG stabilize for thermal lens refractive powers lower than the optimization point. Hence, a significant efficiency drop at pump powers higher than the optimization condition is expected, while the efficiency is

expected to remain comparably high at lower pump powers.

3.3.2 Thermally induced Birefringence

The thermally conductive SiC plate, or plates if bonded to both sides of the gain membrane crystal, is aligned with the optical axis perpendicular to the entrance surface of the resonant laser radiation. In a mechanically stress-free condition, the radiation penetrating along the optical axis will not experience a polarization-dependent phase delay. The bonding process to the gain material and bonding of the structure to a metal heat sink requires the application of mechanical forces. Also, the coefficients of thermal expansion (CTE) of the gain structure, heat spreader(s) and heat sink are not matched. Therefore, some strain is expected to be induced within the structure. Upon the application of thermal load, the CTE mismatch will induce a change in the strain.

An attempt to quantify the unloaded birefringence of the structure was undertaken in an experimental setup. In the same experiment, the reaction of the structure to loading with typical pump radiation absorption-induced thermal loads is analyzed. For the experimental setup, a double-side bonded 922 nm gain structure was soldered to a Ni/Au coated copper heat spreader using a low-melting point hard solder. The heat spreader was water cooled to 15°C. The chip assembly was then pumped with a $d_{pump} = 330\,\mu m$ pump diameter at 808 nm, emitted from a 105 µm core diameter fiber-coupled pump source (bwt K808DA5RN40.00W), providing a maximum output power of 40W. The pump fiber was collimated with an $f = 8\,mm$ collimator (Thorlabs F240SMA-780) and focused into the gain membrane with an $f = 25\,mm$ lens (Thorlabs LA1560-AB-ML) at an incidence angle of about 15°. For qualitative imaging of the birefringence, the superluminescent output of an unpumped fiber optic amplifier (Thorlabs BOA9113S) at around 1050 nm was collimated by an $f = 100\,mm$ lens (Thorlabs LA1251-B) to present a uniform large-area parallel beam to the chip area. The collimated beam was guided through a Glan-Laser calcite polarizer (Thorlabs GL10-B) perpendicularly onto the chip. Behind the chip, a polarizing beam splitter (Thorlabs CCM1-PBS252/M) was

installed as a polarization analyzer. The transmitted radiation was then high-pass filtered twice (Thorlabs FELH900 and FELH1000) in order to reject the amplified spontaneous emission from the gain structure, as well as potential stray light from the pump radiation. Glan-Laser polarizer and polarizing beam splitter (PBS) were aligned to minimize transmission with the MECSEL chip removed from the setup. The residual radiation then was imaged with a CCD camera (THE IMAGING SOURCE DMK 22BUC03) with a 25× imaging objective (Thorlabs MVL25TM23). Using this birefringent imaging setup, different pump powers were applied to the chip. The camera was used to record the light that was transmitted due to depolarization in the chip assembly. The right-hand side of figure 3.19 shows the results. There is noticeable birefringence even in the unpumped setting. This feature appears to be induced by a point-like disturbance, likely due to a surface feature within one surface bond.

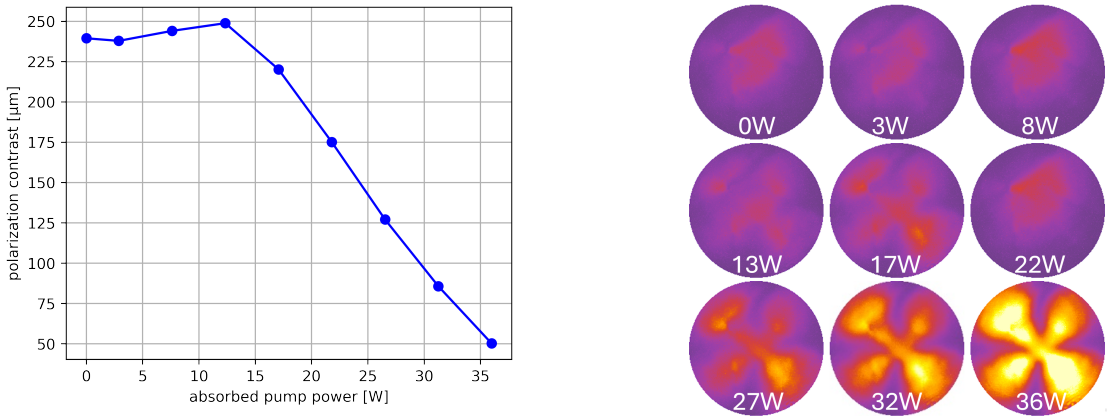

(a) Depolarization of a Gaussian beam **(b)** Crossed polarizer images

Figure 3.19: Analysis of thermally induced birefringence in a double-sided bonded MECSEL chip assembly.

For a more quantitative analysis, yielding practically useable values, the collimator of the broadband 1050 nm source was replaced by an $f = 12$ mm fiber optic collimator (Schäfter & Kirchhoff), which was adjusted to provide a beam diameter of 270 µm at the chip and guided through the center of the pump area in the gain element. Two power meters (Thorlabs PM100D) with Germanium detectors (Thorlabs S122C) were used at the transmitted and reflected output of the PBS to

determine the polarization contrast was determined. On the left-hand side of figure 3.19, the polarization contrast as a function of the absorbed pump power is shown. As indicated by the visual birefringence images, some depolarization of about 240:1 was detected even without any pump light absorbed. At low pump powers, the pump-induced depolarization rotates the polarization back, so that up to 13 W of absorbed power, the polarization ratio increases. Beyond this pump power, the pump-induced depolarization leads to a power-dependent decrease in polarization ratio.

Since the setup was not intended to be used beyond 20 W of absorbed pump power (with $>$ 170:1 polarization contrast), the birefringence is not expected to significantly degrade the laser performance or the performance of its birefringent filter element. When considering higher pump powers, the birefringence needs to be taken into account.

3.3.3 Experimental Evaluation

In an experimental setup, the simulated configuration was realized and the performance was analyzed. The laser remained in single frequency operation over the pump power range of 4 W to 14 W. This was verified by observing a continuously sweeping Scanning-Fabry-Perot (SFP) transmission intensity signal (Thorlabs SA30-120). In figure 3.20, the 556 nm output power is shown, having a pump-to-visible slope efficiency of $\eta = 24\,\%$. At pump powers above 13 W, the efficiency dropped due to the decrease in mode overlap in the gain element, and the core temperature in the gain element rising to a critical level (compare figure 4.10b).

Even though a single-frequency operation with large suppression of side modes indicates the absence of higher-order transverse modes, the transverse beam quality was verified. The 556 nm output beam was collimated and attenuated by multiple reflection passes over uncoated wedged fused silica plates. The beam was then routed into an M^2 measurement system (Thorlabs M2MS), which is capable of scanning the length between a focusing lens and a sampling camera, thereby taking data to compute the caustic through the focus of the lens.

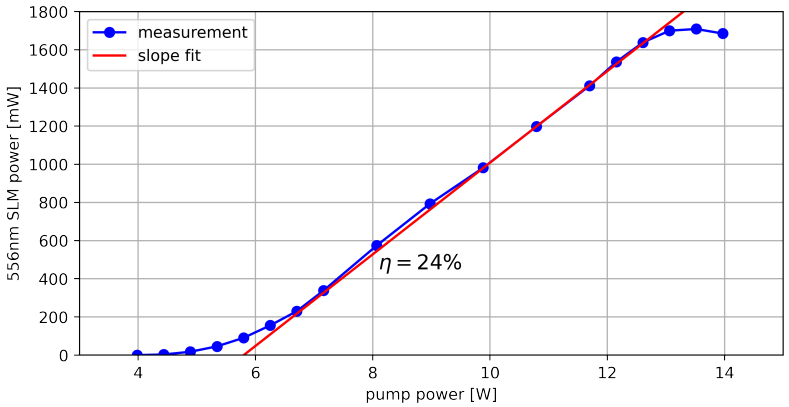

Figure 3.20: Single longitudinal mode output power of a three-mirror MECSEL cavity with intra-cavity frequency conversion to 556 nm.

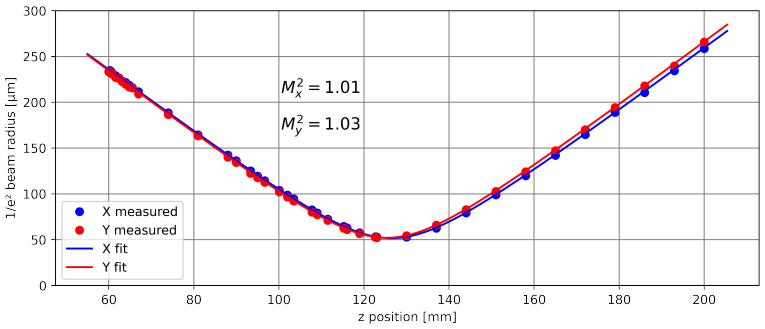

Figure 3.21: 556 nm caustic after a collimation and focusing lens, indicating beam parameters close to the diffraction limit.

The results are shown in figure 3.21, and indicate very good (close to the ideal $M^2 = 1$) beam parameters of $M_x^2 = 1.01$ and $M_y^2 = 1.03$. The beam is slightly distorted in the vertical (Y) direction, which can be explained by the birefringent walkoff that the 556 nm radiation experiences during its creation.

A portion of the fundamental light leakage was probed into an optical spectrum analyzer with a large signal-to-noise ratio (Yokogawa AQ6370D), and the signal-to-noise ratio was determined. Within the measurement noise limit, no amplified spontaneous emission (ASE) signal was detected, resulting in a very pure spectrum with $SNR > 60$dB. This is competitive with amplified ECDL systems (see, for instance, [78]) and is expected to be significantly greater than 60dB in the frequency-doubled spectrum, due to the nonlinear relationship between fundamental and SHG

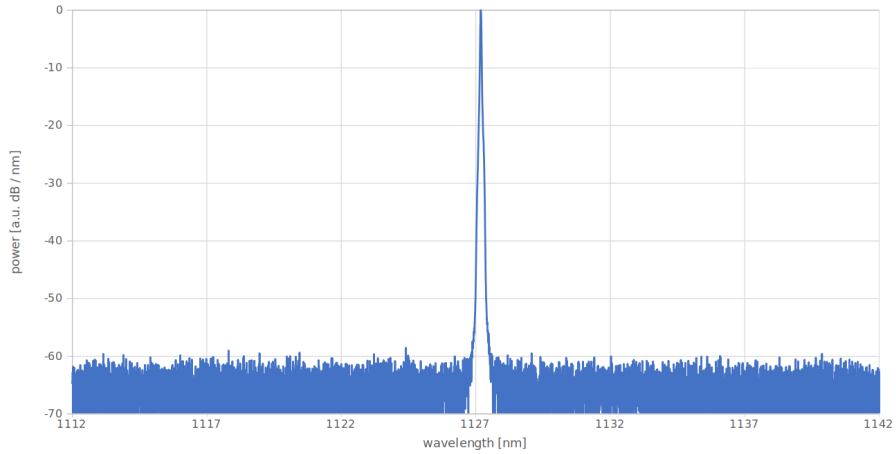

Figure 3.22: Spectral purity measured with an optical spectrum analyzer

power (see chapter 5.1). The SNR advantage of MECSEL compared to amplified ECDL systems can be explained by the relatively smaller gain per pass, and the absence of a cavity-external amplifying system. The external amplifier in ECDL systems provides large gain, which needs to be fully saturated in order to minimize ASE background signal.

3.4 Stable Single Frequency Operation

The laser system described above offers single-frequency operation in all conditions. It should be noted, however, that when the resonator is tuned off-resonance (whether by tuning the wavelength or due to environmental temperature impacts), the laser is prone to switching from one longitudinal mode to an adjacent one. To prevent such mode hopping events, one method is to optimize the length ratio of short and long resonator arms via dither optimization. With this method, a small modulation is induced in the short resonator arm.

3.4.1 Mode Hop Prevention

With a small sinusoidal stroke on M1 (as in figure 3.15), the frequency transfer function of the resonator is altered. In practice, the stroke can be as small as 1/2 nanometer for this method to operate well. Depending on the detuning of the cavity parts, the efficiency of the resonator shows different responses. Only the

AC portion of the signal (generated by an external photodiode) is required for the optimization. In figure 3.23, several interesting positions relative to the ideal position (maximum transmission in the plot) are labeled.

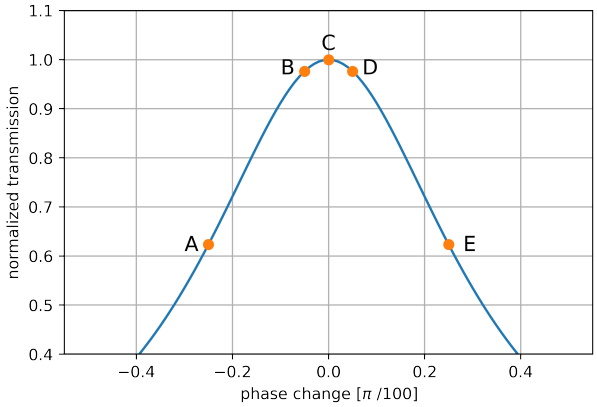

Figure 3.23: Cavity Transmission upon de-tuning of M1, showing labeled positions around ideal resonance.

Upon modulation of the filter function ("mod" in figure 3.24), the signal shows a strong in-phase response at a distant position on the left-hand side (A). Closer to the peak (B), the modulation is in the same phase, but with smaller amplitude. On the opposite side of the transmission maximum, similar signals are induced (D and E), but with 180° phase relative to the input modulation. Right at the peak, the phase is 90°, with twice the modulation frequency.

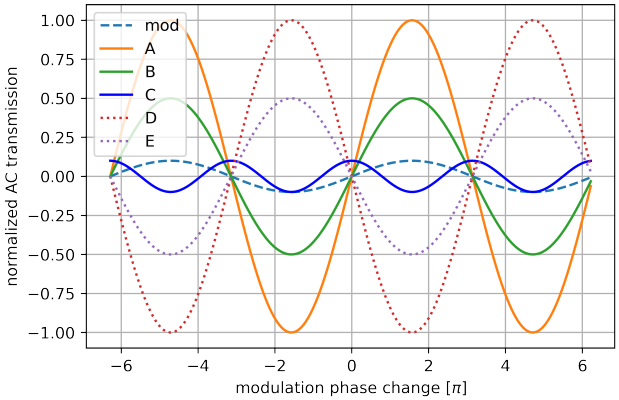

Figure 3.24: Transmission response on AC phase modulation (labeled "mod").

This type of modulation introduces a slight wavelength modulation of the laser output. Since the efficiency of the resonator is the parameter to be detected, the wavelength modulation can be compensated by precisely leveled counteraction in the opposing cavity portion. This is automatically achieved when the laser is externally locked to a frequency reference, using the longer resonator portion (via prism position) as locking-feedback motor.

3.4.2 Tuning Asymmetry

In the experimental setup of the single frequency MECSEL described above, it was observed that the laser had a spectrally asymmetric tuning behavior. When detuning the resonator from the lasing resonance, there is one distinct spectral direction in which this detuning caused the dominant lasing frequency to shift to an adjacent longitudinal mode. In the other direction, this also happened, but required stronger detuning away from the ideal resonance condition.

In order to visualize this effect, the laser (as described in section 3.3.1) was tuned over several longitudinal modes by modifying the length of the short-cavity end mirror of the three-mirror type FP configuration.

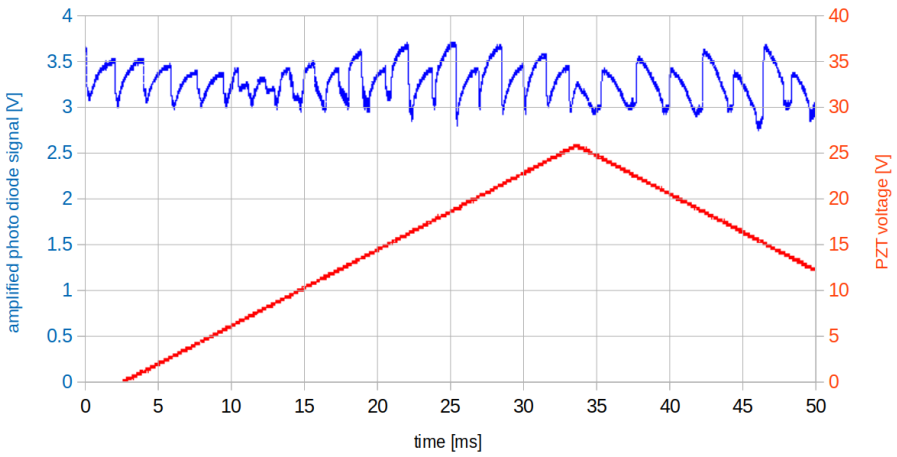

Figure 3.25: Laser output power signal (blue) of a three-mirror MECSEL cavity upon broad tuning of the shorter sub-cavity (red signal depicts PZT actuation voltage $U_{PZT} - l_2$). In this configuration, the spectral filtering is weak and the tuning curve shows spontaneous mode hops to longer wavelengths without power decrease before a mode "hop".

Figure 3.25 depicts the piezo drive voltage and the optical output intensity (at the fundamental wavelength), monitored by an amplified InGaAs photodiode

(Thorlabs DET01CFC/M). Though the plot appears symmetric at first glance, it proves that the tuning is asymmetric, as the data was taken over time. When tuning the piezo drive voltage upwards, the laser power increases until it reaches a point where the laser appears to hop to a different mode. This is remarkable, since when hopping into the next mode, the new lasing condition appears to be less efficient than the condition prior to the mode hop. In the opposite tuning direction (decreasing the piezo drive voltage over time), the behavior follows the expected pattern. The output intensity decreases while detuning from optimal resonance, until a mode hop into a favorable condition (with larger efficiency and output intensity) takes place.

To determine whether this effect is of a dynamic nature or related to nonlinear frequency doubling, a similar experiment was performed at very low speed. In this setup, the output power of a simplified setup was monitored using a power meter (Thorlabs PM100D) with a thermopile sensor (Thorlabs S425C). In the laser setup, the SHG crystal was replaced by an uncoated fused silica substrate of 4 mm thickness and an angle of incidence close to 45°. While tuning the laser more slowly than in the previous experiment, the center wavelength was monitored using a high-resolution diffraction grating spectrometer in Littrow configuration (moglabs MWM).

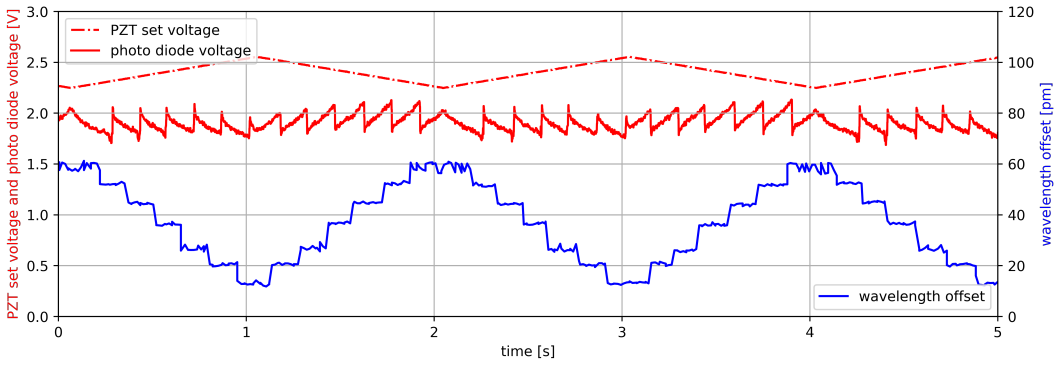

Figure 3.26: Slow scanning of the short cavity arm of a three-mirror cavity, observing center wavelength and power. The plot shows the tendency of the laser to hop toward lower output frequencies.

Even on a timescale of seconds, the simplified setup shows similar behavior. Apparently, the resonating photons experience a larger gain toward lower frequencies. Since the output power that stabilizes after the mode hop into the lower frequency

is lower than the output power before the mode hop, it is assumed that this asymmetric gain is related to the resonating radiation itself. Hence, after a mode hop, the increased gain with spectrally asymmetric distribution would correspond to the new wavelength, allowing a state to become resonant that seems unfavorable in terms of resonance conditions.

One potential explanation is a significant re-absorption of lasing photons inside the Quantum Wells. These would raise the energy in the Quantum Wells to a level where stimulated emission occurs at a lower energy than the energy stored by the absorption process. In a spectroscopic experiment, an unpumped gain chip (designed for 922 nm emission) was analyzed. The amplified spontaneous emission spectrum was detected by a grating spectrometer (Ocean Optics Maya 2000). Using a Titanium-Doped Sapphire Laser (Spectra-Physics 3900s, pumped by a Spectra-Physics Millennia V), a probe beam was directed through the chip. The spectrum from the chip, consisting of emission and scattering, showed a portion of the probe radiation, plus up-converted emission from GaAs (< 900 nm) and the Quantum Wells (900 nm to 930 nm).

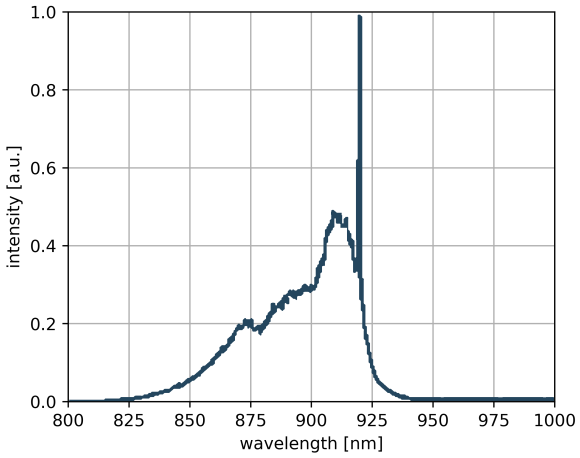

Figure 3.27: ASE and scatter spectrum of a MECSEL gain chip excited with 922 nm radiation.

Figure 3.27 depicts the measurement results, which do not indicate that re-pumping with the resonant laser radiation inside the Quantum Wells gives reason for the longer wavelength ("red-shifted") gain observed in the system.

Transverse modes of higher order than the resonant Gaussian beam cannot have such an impact, as they would appear at higher frequencies than the low-order resonance.

One plausible explanation found is the Bogatov effect. In 1975, Bogatov et al. explained and demonstrated, based on Fabry-Perot semiconductor lasers, an asymmetric effect on the laser gain spectrum, affecting non-lasing longitudinal side modes [79]. Intra-band beating of the resonant photons within the narrow line spectrum of a laser with a single longitudinal mode generates difference frequencies that lead to modulation of the dielectric constant of the semiconductor material. This modulation, initiated by a standing wave, creates a diffraction grating that generates a counter-propagating wave with a π phase shift relative to the resonant radiation, resulting in partial depletion of the resonant laser wave. Since the grating is dependent on the spontaneous carrier lifetime $\tau_s \approx \tau_{th}$ (see 2.4) in the semiconductor material, the grating disappears with frequencies rising above $1/\tau_s$.

In a work that developed rate equation models in semiconductor lasers with spatial hole burning, Lenstra et al. converted Bogatov's equation into gain equations [80]. While spatial hole burning is not a topic of interest in multi-Quantum-Well lasers due to the tight spatial confinement of the Quantum Wells, the derived equation can be applied to the case of MECSEL:

$$g_{Bog} = \frac{1}{4}\theta g_1 P \frac{\alpha\Omega - \frac{1}{\tau_s} - \theta P}{\Omega^2 - \left(\frac{1}{\tau_{th}} + \theta P\right)^2} \tag{3.57}$$

θ is the differential gain, and g_1 the linear gain. The value for the differential gain was taken from [80], and the linear gain was derived from a typical QW thickness of 44 nm, with 11 pairs, and the values given in 2.2. The linewidth enhancement factor α is taken as the ratio between the measured linewidth and the theoretical linewidth limit (see chapter 5.3 for details). $\Omega = \omega_0 - \omega_1$ is defined as the frequency difference. This is the definition as presented in the original paper [79], and subsequent publications by other groups. The definition is counter-intuitive, though, as an Ω_1 larger than the center frequency ω_0 corresponds to a larger

wavelength. In order to ease interpretation, $-\Omega$ is depicted in figure 3.28, so that larger frequencies Ω_1 plotted toward the right side of the graph.

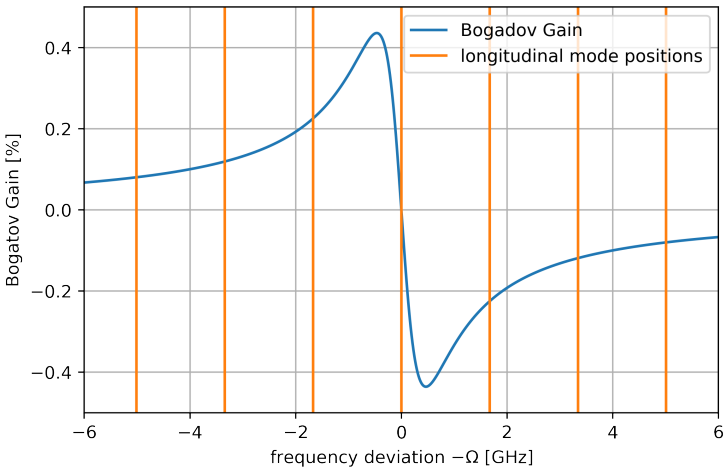

Figure 3.28: Asymmetric Bogatov gain spectrum and center and non-lasing side modes. Note that the x-axis is scaled with $-\Omega$, plotting elevating relative frequency with respect to the center frequency toward the right side.

At a laser power of $P = 2W$, the spectral distribution of the gain profile is shown around the center lasing frequency. In the plot, the positions of the center and non-lasing side modes (governed by the FSR of the laser cavity) is indicated, showing that a transition to the adjacent mode of longer wavelength is associated with the highest Bogatov g_{Bog}. The model explains the observed tuning behavior well, and gives an indication of the filter function quality needed to overcome the disadvantage created by the Bogatov effect. With a cavity resonance layout as described in section 3.2, and reflectivities of $R_1 = 92\%$, $R_2 = 30\%$ and $R_3 = 98\%$, the filter function is sufficient to cause a significant efficiency loss upon tuning toward larger wavelengths. Using this setting, tuning curves as depicted in figure 3.29 were recorded.

Figure 3.29 shows a nearly symmetrical power tuning into adjacent frequency modes, compared to the weaker frequency filtering applied when taking the data shown in figure 3.25. In this significantly more symmetric tuning configuration, the laser efficiency drops before a mode hop into either the higher or the lower frequency adjacent mode occurs.

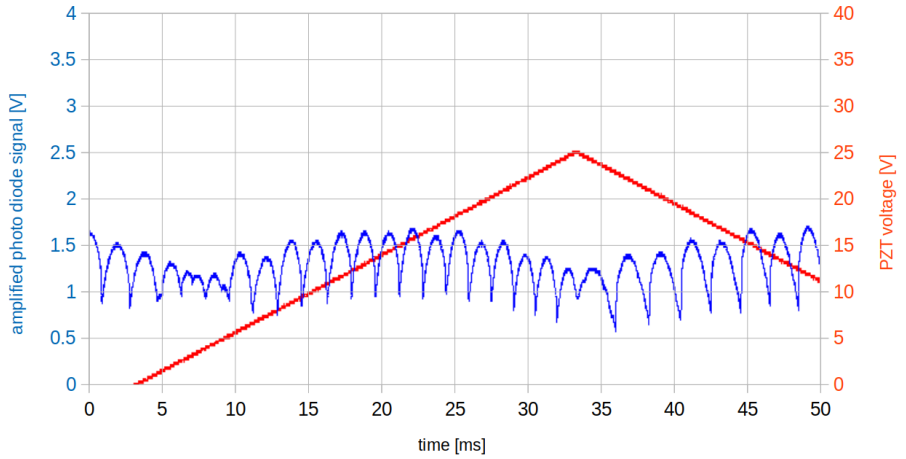

Figure 3.29: Laser output power signal (blue) of a three-mirror MECSEL cavity upon broad tuning of the shorter sub-cavity (PZT voltage in red). In this configuration, the spectral filtering is strong and the tuning curve shows power decrease before a mode "hop" in both tuning directions.

3.4.3 Continuous Tuning

Using the extremum seeking optimization described in section 3.4.1, the shorter laser arm distance is kept at approximately the position of highest laser efficiency, which is the setting furthest from a critical mode hop situation. When the long cavity arm length is tuned, the laser remains operating in a single longitudinal mode.

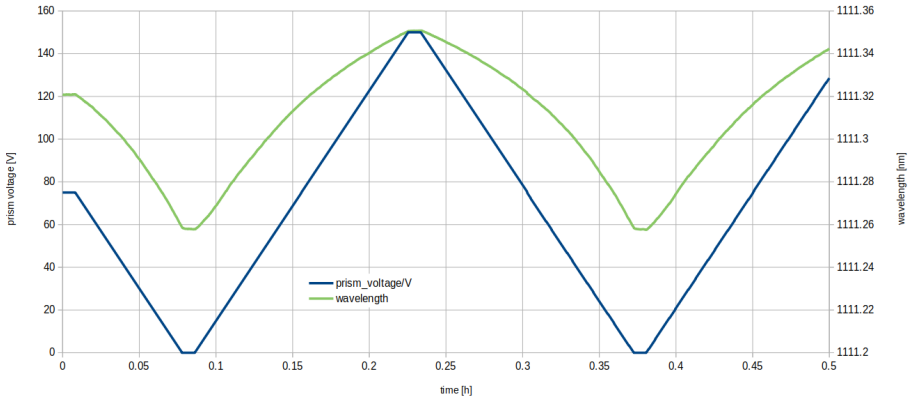

Figure 3.30: Single longitudinal mode wavelength tuning (measuring the fundamental wavelength of the resonator) with activated dither optimization of the short-length cavity arm, acquired with a three-mirror MECSEL cavity with intra-cavity frequency conversion to 556 nm.

Figure 3.30 shows the result of a slow tuning experiment spanning 90 pm. In the plot, both PZT voltage and wavelength (measured with Thorlabs OSA202C) are

plotted over time. The wavelength change shows some nonlinearity, which is related to the physical length response of the PZT upon voltage alteration. The tuning range limitation was determined by the stroke of the piezo element in the long cavity arm. Since, for the intended application, the tuning is more than sufficient to reach and maintain the critical cooling lines, no further optimization of the setup for broader tuning was attempted. In practice, the laser setup could operate for many days under usual laboratory conditions, without showing instabilities or mode hops.

4

Thermal Lensing and Dynamic Response

The MECSEL gain element, consisting of a Silicon Carbide heat spreader bonded to the gain material, and a heat sink unit, has limited thermal conductivity, so that absorbed pump light generates a temperature increase in the optically pumped region. Due to thermal expansion and a temperature-dependent refractive index of the material transmitting the resonant laser light, a phase distortion with radial dependence is introduced to the resonant laser beam. This is commonly referred to as "thermal lens".

In order to analyze the thermal lens developed in MECSEL in more detail, a finite element simulation was set up and analyzed, including derivation of Zernike terms. Additionally, the wavefront distortion was measured and compared with the simulated data.

Followed by the aberration analysis, the temporal dynamic response of the phase distortion was simulated using the same finite element model of the gain element. This dynamic phase response is considered of interest since frequency modulation, based on modulation of excitation pump intensity, could improve the frequency stability of MECSEL systems. Experimental data are created using feedback data from a MECSEL system stabilized to an external Fabry-Perot cavity.

4.1 Experimental Evaluation of the Thermal Lens

The measurement setup for the thermal lens analysis is depicted in figure 4.1. In order to measure the thermal lens developed in a MECSEL setup, a single side SiC (500 µm thickness) bonded gain assembly is mounted to a TEC-cooled water heatsink using compressed Indium foil of 100 µm thickness. The pump absorption in the test chip, centered at a 930 nm emission wavelength, is measured at 85 % of the light entering the chip. The SiC surface is coated with an anti-reflective dielectric stack, while the chip surface is uncoated, causing a reflection of 32.8 % of the unpolarized pump radiation. The MECSEL is excited using a fiber coupled 808 nm laser diode source (bwt K808DA5RN40.00W) with 105 µm core diameter and a maximum output power of 40 W. The pump fiber is collimated with an $f = 8$ mm collimator (Thorlabs F240SMA-780) and focused with several singlet lenses of various dioptric powers throughout the tests.

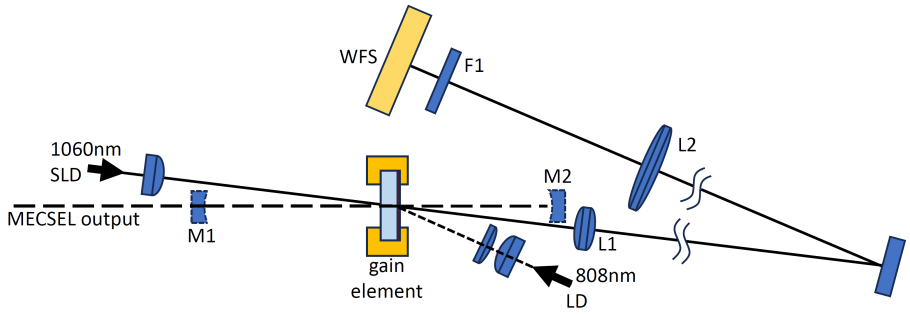

Figure 4.1: Thermal lens analysis setup with MECSEL cavity, optical pump and broadband probe beam directed into a Shack-Hartmann wavefront sensor

The MECSEL cavity is defined by two concave mirrors, M1 with $R = 150$ mm at 60 mm distance to the gain stack, and M2 with $R = 150$ mm at 90 mm distance to the gain stack. M1 is designed for 2 % transmission, while M2 is coated with a high reflectivity Bragg stack (both mirrors custom made by Laseroptik GmbH). The laser cavity is blocked or opened throughout the measurements. For the thermal lens analysis, a superluminescent diode (SLD), more specifically, the superluminescent output of a fiber optic amplifier (Thorlabs BOA9113S) at around 1050 nm is collimated by an $f = 12$ mm fiber optic collimator (Schäfter & Kirchhoff) and

guided through the pump area of the gain element. The emission exit surface is projected onto a Shack-Hartmann wavefront sensor (Thorlabs WFS30-5C/M) using a 4f configuration with $f = 75\,\text{mm}$ and $f = 400\,\text{mm}$ (Thorlabs AC254-075-AB-ML and LA1172-A-ML), in order to illuminate a sufficient amount of micro lenses of the wavefront sensor. These have a pitch of 150 µm (Thorlabs MLA150-5C). In order to suppress distortion of the wavefront measurement by pump or MECSEL emission photons, a filter unit F1 consisting of a high (transmission >950 nm) and low pass filter (transmission <1100 nm) was introduced, allowing transmission of the superluminescent emission beam (Thorlabs FELH950 and FEL1100).

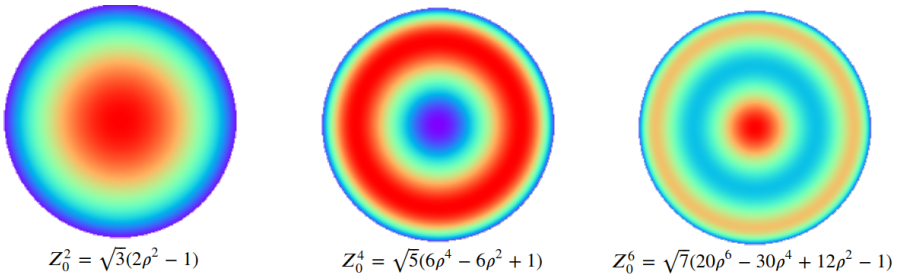

Figure 4.2: Radially symmetric Zernike terms "defocus" (left), "primary spherical" (center) and "secondary spherical" (right) with their equations, normalized to 2π and 1 in phase and extension

Since the pump beam, as well as the heat sink mechanics, has a round transverse shape, the relevant distortions are the radially symmetric Zernike terms. These are depicted in figure 4.2. The wavefront is described as the sum of Zernike terms, with the coefficients Z_n^m, where the radial terms are normalized by $\sqrt{n-1}$:

$$W(\rho,\theta) = \sum_0^\infty c_n^m Z_n^m(\rho,\theta). \tag{4.1}$$

The Zernike terms are defined according to the ANSI Standard Z80.28-210, and scaled to true dimensions based on a circular pupil diameter of 5 mm. In equation 4.1, ρ gives the radial distance from the center, and θ is the azimuth angle, with the (positive) term integers m and n.

Figure 4.3 depicts the major coefficients measured at 10.6 W absorbed pump power (395 µm pump spot diameter). The values provided by the wavefront

sensor used need to be scaled with the ratio of focal lengths of the 4f imaging configuration.Due to the probe beam entering the MECSEL chip at an angle, the Zernike tilt terms are apparent, but they are ignored in the analysis, as are the coma terms, which are directly related to the tilted thermal lens. In the following investigations, the radially symmetric terms of defocus, first and second order spherical aberrations (as depicted in figure 4.2) are highlighted as major impact factors for thermal lensing and aberration losses in the laser cavity.

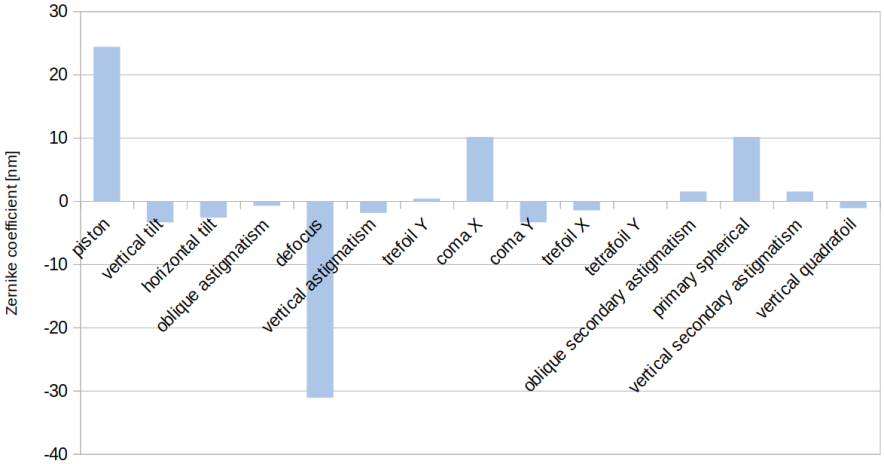

Figure 4.3: Zernike coefficients measured at 10.6 W absorbed pump power, with 395 µm pump spot diameter

The wavefront measurement is performed in lasing and non-lasing conditions, with the results summarized in figure 4.4. Up to lasing threshold, the data are identical. The absorbed pump power in this regime is dissipated through the SiC plate, black-body radiation and ASE. When lasing action occurs, additional power is extracted from the pumped area of the Quantum Well stack, leading to a reduction of the thermal lens power compared to the non-lasing thermal lens. During the exploration of laser configurations, this difference became apparent when operating the laser close to stability limits for large thermal lens powers. The laser could still be operated at such a point, but only by tuning the pump power up, so that the depletion of the thermal lens due to the thermal load reduction in the stimulated emission case occurs. Upon blocking the laser resonance, the thermal lens can be too high to allow stable resonance to initiate.

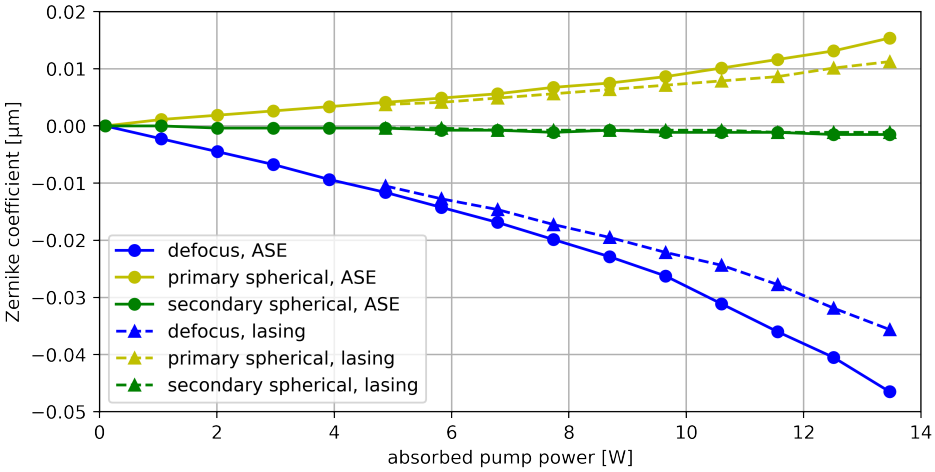

Figure 4.4: Radially symmetric Zernike terms measured at 395 µm pump spot diameter on a 930 nm MECSEL assembly: defocus (blue), primary spherical (red) and secondary spherical (yellow) are displayed with a µm scale. The solid line represents the measurement without laser action, while the dashed line shows the results under lasing conditions.

The laser setup provides no means of frequency stabilization, hence the output spectrum provides several longitudinal modes. The output power of pump radiation with respect to the pump current, as well as the output power of the MECSEL, is measured with a thermal power detector (Thorlabs S322C). This laser setup is not intended for the highest output efficiency. It was chosen because the waist diameter of the laser matches the pump diameter well, while also showing little beam diameter change (at the position of the thermal lens) over the expected thermal lens dioptric power range. This is important to simplify the comparison to the modeled scenario, where the laser beam radius is expected to be fixed. Figure 4.5 shows the measurement results with a slope efficiency of $\eta = 16\,\%$. Using the ABCD matrix approach (see section 3.3), the $1/e^2$ beam radius at the gain element is approximated and also plotted in figure 4.5.

The rate of amplified spontaneous emission is determined in non-lasing operation, using a photodiode detector (Thorlabs S120C) with a 9.7 mm diameter aperture and a filter that suppresses the transmission of pump photons (Thorlabs FELH0850). The sensor was placed at a distance of 45 mm along the optical axis of the setup. Under the assumption that the amplified spontaneous emission is uniform in all

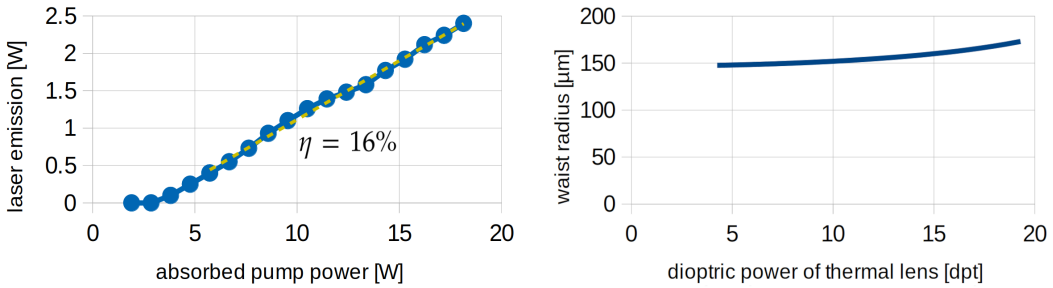

Figure 4.5: Laser emission slope of a 930 nm linear MECSEL cavity (left) and calculated waist radius of the cavity with respect to thermal lens power (right)

emission directions, the total ASE power was calculated by the ratio of sensor area to the area of a sphere with 45 mm radius. Since the ASE efficiency needs to be related to temperature in the following analysis, the average temperature in the pump-affected zone was determined. Since direct contact with the affected zone cannot be made without introducing direct absorption of pump radiation into the temperature sensor, the temperature increase was determined by the shift of the ASE center wavelength, coupling some ASE light from the affected zone into a fiber-optic spectrometer (Thorlabs CCS100), using a focusing lens (AC127-030-AB-ML) and a fiber-optic collimator (Thorlabs F240SMA-780). As a calibration for this measurement, the ASE center wavelength shift with temperature was analyzed at low (2 W absorbed) pump power while tuning the temperature of the heat sink (TEC-controlled). The results, with respect to the absorbed pump power, are plotted in figure 4.10a.

4.2 Finite Element Analysis

4.2.1 Model

A finite element model was implemented to study the thermal response of the MECSEL gain element, utilizing a 500 µm thick SiC plate, to pump light in more detail. The three-dimensional tetrahedral mesh generation was performed based on a stepped model with a 5 mm diameter, using SALOME [81]. The mesh optimization targeted a high mesh density in the pumped region (350 µm diameter), and lower spatial resolution in the outer areas.

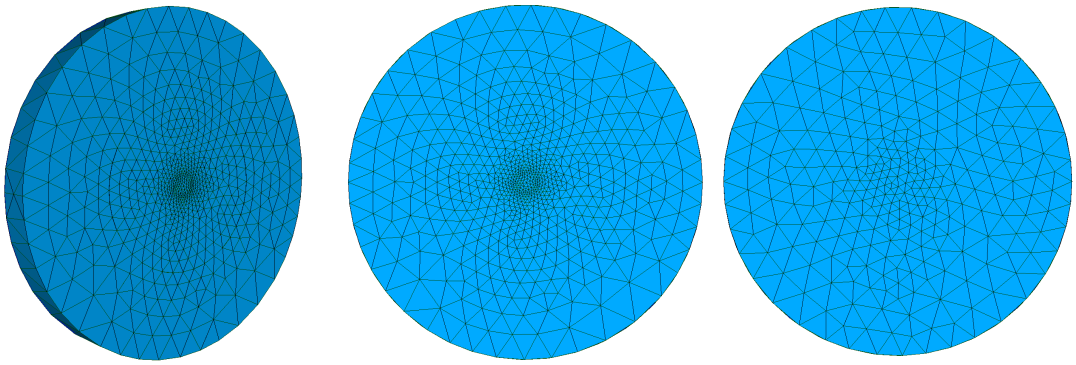

(a) Isometric view **(b)** Gain side **(c)** Back side

Figure 4.6: Mesh used in thermal evaluation of heat spreader

Figure 4.6 illustrates the results of the mesh generation. Temperature computations based on absorbed laser power, defined boundary conditions and various emission schemes were performed using the FEniCS computing platform, including DOLFINx [82], Basix [83] and UFL [84]. The FEniCS platform accepts C++ code for function definitions and is accessible through a Python interface. A representative example code is accessible in the appendix A.1.

The boundary conditions are defined such that an outer ring, ranging from a 2.5 mm to 5 mm diameter on the gain side, is held at a constant temperature (20°C Dirichlet condition), while the center region of the surface is loaded with a heat source shaped to represent the pump radiation absorbed by the Quantum Well structure.

The localized power distribution is modeled using a super-Gauss function in the transverse x and y directions, where w is the radius, and k determines the flatness

of the profile. In equation 4.2, $k = 1$ yields a standard Gaussian distribution, while higher values flatten the profile:

$$S(x) = A(w,k) \times e^{-\left|\frac{x}{w}\right|^k}. \tag{4.2}$$

The super-Gaussian function is normalized using the gamma function:

$$A(w,k) = \frac{k}{2w\Gamma\left(\frac{1}{k}\right)} \tag{4.3}$$

Since the pump beam is distributed from a multi-mode step-index silica fiber with a nominal diameter of 105 µm, the super-Gaussian order k was defined as $k = 50$, which yields an intensity distribution similar to that of single-mode fibers of the same material at the outer boundaries, while maintaining a flat distribution at the center. Perpendicular to the chip surface, the direction of pump absorption and travel direction of the resonant light, the pump distribution is modeled according to the Beer–Bouguer–Lambert law with an absorption coefficient μ. For simplicity, total absorption is assumed. This is not exact, since only approximately 0.85 % of the power is absorbed in a typical Quantum Well stack used in our tests. This deviation is approximately compensated by referencing the "absorbed pump power" when comparing to measured results. The two-dimensional super-Gaussian distribution and the normalized Beer-Lambert law yield the three-dimensional power distribution in the Quantum Well stack:

$$P(x,y,z) = \frac{P_{tot}A^2\mu}{\sqrt{2\pi}} \exp\left(-\left|\frac{\sqrt{(x^2+y^2)}}{w}\right|^k\right) \cdot e^{-\mu \cdot z} \tag{4.4}$$

In this equation, P_{tot} is the total power, A is the normalization factor for the super-Gaussian distribution with the super-Gaussian factor k, and w represents the $1/e^2$ radius of the pump beam in the x and y directions. The heat flux in the simulation is emulated according to Fourier's law of heat conduction

$$q_i = -\kappa G_i(x_i, t), with \tag{4.5}$$

$$G_i = \frac{\partial T}{\partial x_i}, \tag{4.6}$$

where κ is the thermal conductivity, G_i is the temperature gradient. The x, y, z spatial components are indexed from 0 to 2 in x_i. The temperature gradient lag τ_T and heat flux lag τ_q are not taken into account, as these values are expected to be in the ps range and are not significant for the analysis of temporal response in the sub-MHz regime.

The weak form of the energy distribution in the body can be described as [85]:

$$\begin{aligned} form = \int_{\mathcal{B}} \Bigg(& \tfrac{c}{\Delta t}(T - T_0)\delta T - q_i \tfrac{\partial \delta T}{\partial x_i} - P\delta T d\nu \\ & + \int_{\partial\mathcal{B}} \Big(h(T - T_a) + \epsilon\sigma(T^4 - T_a^4) \Big) \Bigg) \delta T da. \end{aligned} \tag{4.7}$$

The first integral integrates infinitesimal volume elements of the volumetric body, and the second integral is a surface integral. Here, c represents the specific heat capacity. h is the convective heat transfer coefficient, and the Stefan-Boltzmann law for black-body radiation is $P_{bb} = \epsilon\sigma \cdot A \cdot T^4$, with the emissivity ϵ and the Stefan-Boltzmann constant σ. The thermally induced emissivity of GaAs is about 0.06 in the temperature range of 20°C to 80°C [86], which with $\sigma = 5.67 \cdot 10^{-8}\,\mathrm{W/m^2}$ yields a total emission of $10\,\mu\mathrm{W}$ at an effective area in the pumped zone of $10^{-7}\,m^2$. This is insignificant compared to the multi-Watt level powers in our model. The heat convection is estimated to be in the same regime (based on $h \approx 15\,\mathrm{W/(m^2K)}$, see [87]), hence both are neglected. This simplifies the form to equation 4.8.

$$form = \int_{\mathcal{B}} \left(\frac{c}{\Delta t}(T - T_0)\delta T - q_i \frac{\partial \delta T}{\partial x_i} - P\delta T d\nu \right) \delta T da. \tag{4.8}$$

parameter	value	reference
specific heat capacity C	$750\,\mathrm{J/(kg \cdot K)}$	[88]
thermal conductivity κ	$480\,\mathrm{W/(m \cdot K)}$	[48]

Table 4.1: 4H silicon carbide thermal properties

The processing was performed based on the parameters listed in table 4.1. The temperature distribution was determined at steady state (1.5 seconds pumping duration), depicted in figure 4.7. The surface-near nodes around the pump absorption were exposed to a temperature rise of nearly 25 K with a sharp Gauss-like peak. Throughout the chip, there was an additional temperature decay induced by the limited thermal flow through the 500 µm thick SiC crystal.

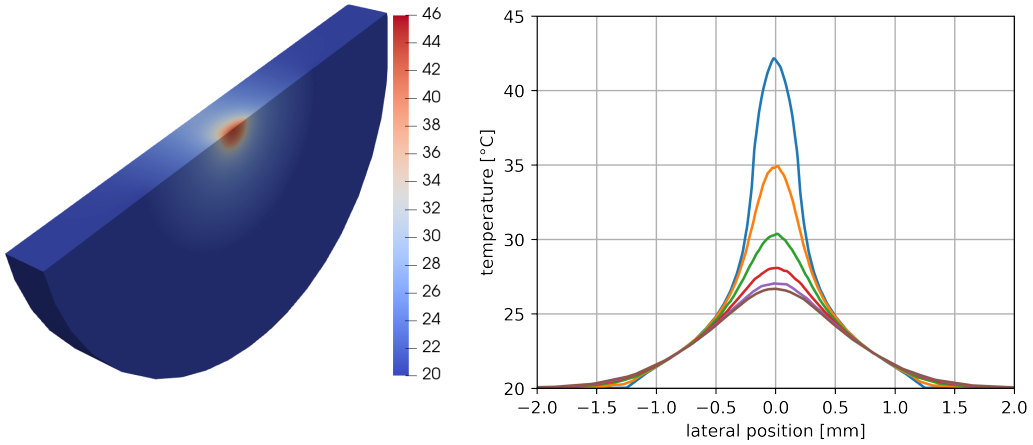

(a) 3D temperature distribution **(b)** Temperature cross sections

Figure 4.7: Image on the left: sliced view of the temperature distribution in a 5 mm diameter SiC plate of 500 µm thickness with 10 W of pump light absorbed near the surface. The plot on the right depicts the lateral temperatures across the center at 100 µm spaced depths from the absorbing surface into the crystal.

In section 4.2.2, further pumping scenarios are plotted, including amplified spontaneous emission and laser operation induced power depletion.

For analysis of the thermo-optical impact of the temperature distribution calculated over the three-dimensional tetrahedal mesh, the data are interpolated to Cartesian coordinates. After this step, the maximum temperature is extracted. The dataset is then averaged in temperature in the direction of the laser beam, perpendicular to the plano surface of the dataset, to create a two-dimensional

dataset of average temperature over the plane. This is cropped to the area of interest (1 mm x 1 mm). With the thickness $d_{SiC} = 500\,\mu\text{m}$ of the Silicon Carbide crystal, the temperature-dependent refractive index change dn/dt and the thermal expansion coefficient α_{33} of Silicon Carbide in the direction of the laser photon travel direction, the temperature-dependent change of the optical path length, derived as Δd_{opt} (in m), is calculated. The material parameters are listed in 4.2. Note that the refractive index n is not required to compute changes in the phase distribution. For steady-state analysis, the thermal simulation is computed at $t = 1.5\,\text{s}$ with $\Delta t = 500\,\text{ms}$ intervals to ensure that the lens is thermally stable.

parameter	value	ref
relative refractive index dn/dT	$3.87 \cdot 10^{-5}\,\text{s}^{-1}$	[71]
thermal expansion coeff. α_{33}	$\left(3.09 \cdot 10^{-6} + 2.63 \cdot 10^{-9} T/°\text{C} - 1.08 \cdot 10^{-12} T^2/°\text{C}^2\right) °\text{C}^{-1}$	[49]

Table 4.2: 4H silicon carbide thermo-optical properties

$$\Delta d_{opt} = T_{av} \left(\frac{dn}{dt} + \alpha_{33} \right) d_{Sic} \tag{4.9}$$

Due to the limited number of nodes in the mesh, the datasets have limited resolution. Since all aberrations of interest are radially invariant, radial averaging of the temperature distribution around the center of the simulated heat source is performed. Figure 4.8 depicts raw and averaged data from simulation of 14 W of absorbed pump power in a 395 m diameter spot.

The two-dimensional phase shift data describe a phase mask that can directly be used to fit Zernike coefficients according to the terms depicted in figure 4.2, using the method of minimizing the sum of squared errors. These terms can directly be compared to the wavefront sensor data. To evaluate the effective dioptric power of the simulated thermal lens, as well as to assess its effect on laser beam parameters, a virtual collimated Gaussian laser beam is guided through the phase mask and propagated over various distances to allow analysis of the effective focal length of the thermally induced phase mask. The size of the ideal Gaussian probe beam shape is taken to be approximately 1.14 times the pump spot diameter in

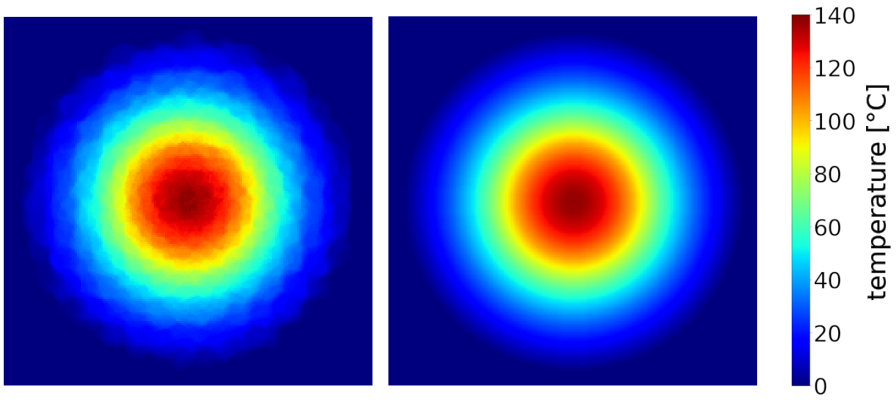

Figure 4.8: Relative phase shift (in nm) summed up in the z-direction through a simulated 1 mm x 1 mm field, computed by an FEM simulation of 14 W absorbed pump power with a 395 µm pump spot size and laser emission depletion. Raw data is shown in the left image, radially imaged data in the right image.

the absorption region (440 µm in the case of 395 µm pump diameter), which is a practically evaluated ratio that ensures diffraction-limited operation of the laser device while maintaining sufficient gain extraction. The computation of the virtual propagation is performed using a Fourier transform with the Fresnel approximation (see [89] and [90]). The intensity data of the two-dimensional Gauss distribution in x and y direction and the phase information taken from the phase mask provide a complex two-dimensional wave function $U(x, y, 0)$, which is transferred into Fourier space in directions α and β, yielding the wave functions $A(\alpha, \beta, 0)$ for the initial wave function and the wave function after propagation over the distance z, labeled $A(\alpha, \beta, z)$. These are related by the free space frequency transfer function H:

$$A(\alpha, \beta, 0) = \int \int_{-\infty}^{\infty} U(x, y, 0) e^{-ikz(\alpha x + \beta y)} dx dy \tag{4.10}$$

$$A(\alpha, \beta, z) = \int \int_{-\infty}^{\infty} U(x, y, z) e^{-ikz(\alpha x + \beta y)} dx dy \tag{4.11}$$

$$H = \frac{A(\alpha, \beta, z)}{A(\alpha, \beta, 0)} = e^{-ikz\sqrt{(1-\alpha^2-\beta^2)}} \tag{4.12}$$

Applying a thin lens to the light field is performed by a spherical shift of the phase term:

$$\frac{U_{out}(x,y)}{U_{in}(x,y)} = e^{-j\frac{2\pi}{\lambda}\frac{x^2+y^2}{2f}} \tag{4.13}$$

The Python toolbox Lightpipes [91] offers an efficient implementation of the above calculations and was utilized in the further analysis. For determination of the thermal lens refractive power in paraxial approximation, a virtual light field was propagated through the thermally induced phase mask of the MECSEL model. Then the computed caustic was compared with a caustic calculated with an ideal thin lens, optimized for minimum sum of squared errors of the Gaussian diameter.

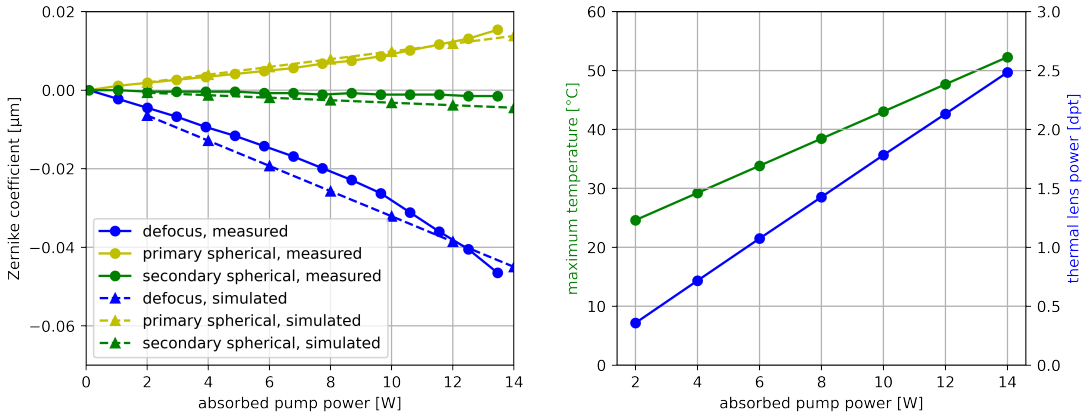

Figure 4.9: Left plot: Zernike coefficients simulated without ASE and lasing action: defocus (blue), primary spherical (red) and secondary spherical (yellow), with simulation as dashed line compared to measured data as solid line. Right plot: focusing power and maximum chip temperature computed under the same conditions.

Comparing the measured and simulated data, especially for the Zernike term for defocus, shows significant differences, as shown in figure 4.9. Since the parameters used in the above simulation are not significantly impacted by temperature, the finite element analysis is extended by the introduction of ASE and laser emission.

4.2.2 Representation of ASE and Laser Emission

For the simulation of the temperature T distribution with resonant lasing action, a Gaussian beam (with $k = 1$ according to equation 4.4) is subtracted from the

pump power distribution with a power relationship according to a typical slope efficiency value of $\eta_{laser} = 16\,\%$.

The ASE efficiency relationship with temperature (as depicted in Figure 4.10a) requires the form function of the finite element analysis to be modified. Several approaches to fitting the efficiency curve with potential or exponential equation caused the Newton solver used in the finite element analysis to omit convergence. Hence, a mathematically simpler approach was utilized, fitting the experimental dependency of ASE efficiency with temperature by a cosine function. Figure 4.10b compares two fit profiles with the measured data. A quadratic fit (4.14) is depicted in figure 4.10b along with the cosine fit (4.15) over the measured data. Here, $b = 0.11$ is the cosine fit scaling factor, and $\Gamma_{ASE} = 0.29$ is the rate of amplified spontaneous emission at 20°C.

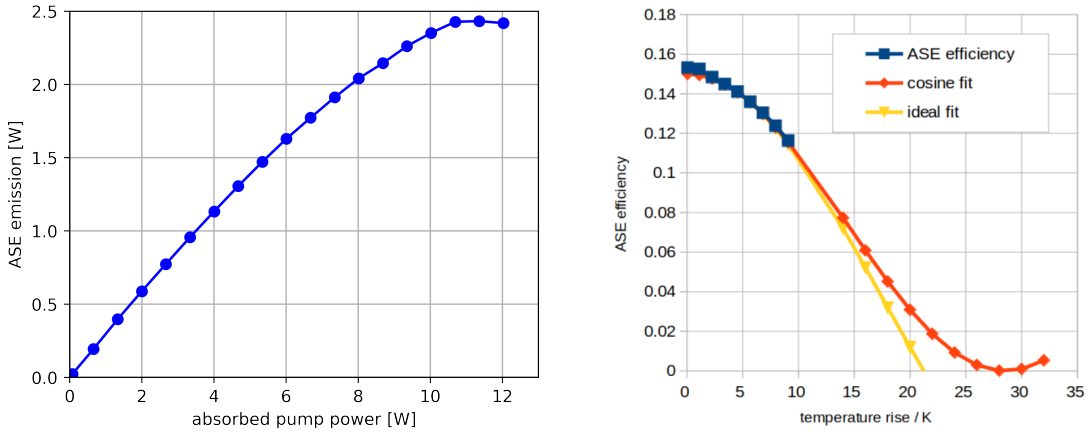

(a) ASE power **(b)** ASE efficiency vs. temperature

Figure 4.10: Determination of ASE efficiency and dependency on the average temperature of the pumped gain membrane area

$$\eta_{ASEsq}(T) = 0.29 - (0.025T)^2 \tag{4.14}$$

$$\eta_{ASEcos}(T) = \Gamma_{ASE20}\Big(1 + \cos(bT)\Big) \tag{4.15}$$

The ASE efficiency is expected to further collapse at larger average temperatures of the pumped area, so that the quadratic fit is expected to yield more realistic results at larger pump powers or smaller pump spot diameters. The implementation of the cosine fit function into the weak form for the finite element analysis reads:

$$\begin{aligned} form = \int_{\mathcal{B}} \Bigg(& \tfrac{c}{\Delta t}(T - T_0)\delta T - q_i \tfrac{\partial \delta T}{\partial x_i} - \Big(1 - \Gamma_{ASE20}\Big) P \delta T \\ & - \tfrac{1}{2}\Gamma_{ASE20} \Bigg(1 + \cos\Big(b(T - T_0)\Big) \Bigg) P \delta T \Bigg) d\nu) \delta T da. \end{aligned} \tag{4.16}$$

4.2.3 Thermal Lens Computation Results

Based on the form 4.16, the measured Zernike coefficients are compared to the simulated data, as plotted in figure 4.11.

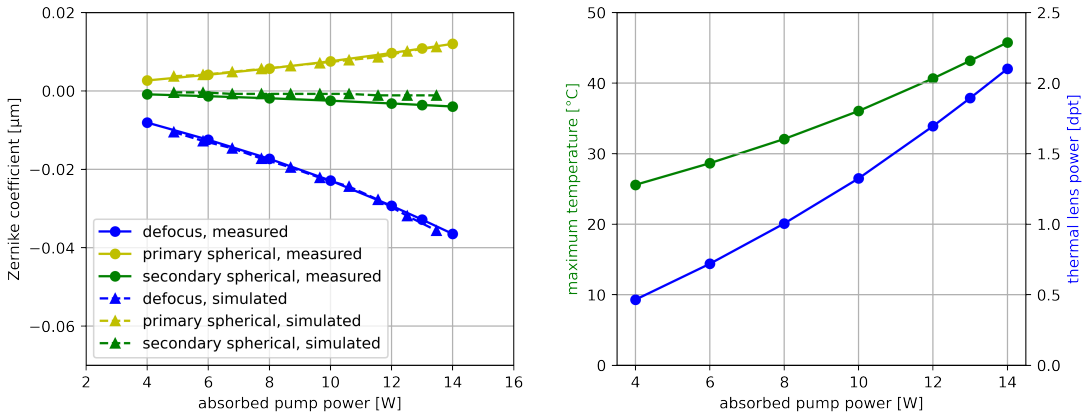

Figure 4.11: Left plot: Zernike coefficients with respect to pump power at 395 µm pump spot size, simulated with ASE and lasing action: defocus (blue), primary spherical (red) and secondary spherical (yellow), with simulation as dashed line compared to measured data as solid line. Right plot: focusing power and maximum chip temperature computed under the same conditions.

As in the previous simulation procedures, a pump spot diameter of 395 µm was chosen for the computation series. In the parameter space of interest, the cosine ASE fit is sufficient to provide a realistic similarity between measured and simulated data. The Zernike coefficients for defocus and primary spherical aberration are in agreement. The secondary spherical aberration is significantly off in comparison

to the model with experimental data and shows the resolution limit of the model with the chosen node density. At the front surface, where most of the heat is applied, the nodes have an average spacing of approximately 60 µm. Since the secondary spherical aberration includes radius terms of the order of four and six, very small deviations in the lateral dimension (resolved at approximately 1/7 of the Zernike fit diameter) impact the result. Since the secondary spherical aberration is very small compared to defocus and primary spherical aberration, no further optimization of the model was undertaken.

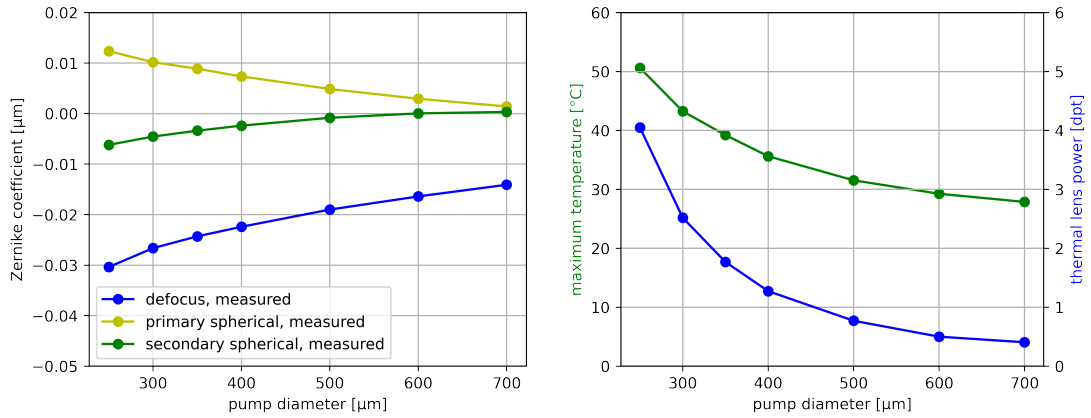

Figure 4.12: Left plot: Zernike coefficients with respect to pump focus size at 10 W absorbed power, simulated with ASE and lasing action: defocus (blue), primary spherical (red) and secondary spherical (yellow), with simulation as dashed line compared to measured data as solid line. Right plot: focusing power and maximum chip temperature computed under the same conditions.

The thermal lens approximation, based on the paraxial approximation of the computation result, served as the basis for optimization of MECSEL cavities. With the results from the simulation model, the dependency of thermal lens and aberrations on the pump spot diameter, was numerically determined. The results are depicted in figure 4.12 for an absorbed pump power of 10 W.

4.2.4 Aperture Size Dependency

The thermal lens is not an ideal lens, and due to the non-spherical temperature distribution across the center of pump absorption (compare figure 4.7b), the effective

focal length (EFL) for a Gauss beam penetrating through the thermal lens, is a function of its irradiated area. For the previous analysis, a $1/e^2$ ideal Gaussian probe beam of 440 µm diameter was simulated. In a resonant laser cavity with a thermal lens contributing to the stability of the resonant laser radiation, the Gaussian radius of the resonant radiation is a function of the focal length of the effective thermal lens inside the laser cavity. Figure 4.13 shows the dependency of the effective thermal lens on the beam radius, depicted for various pump powers levels.

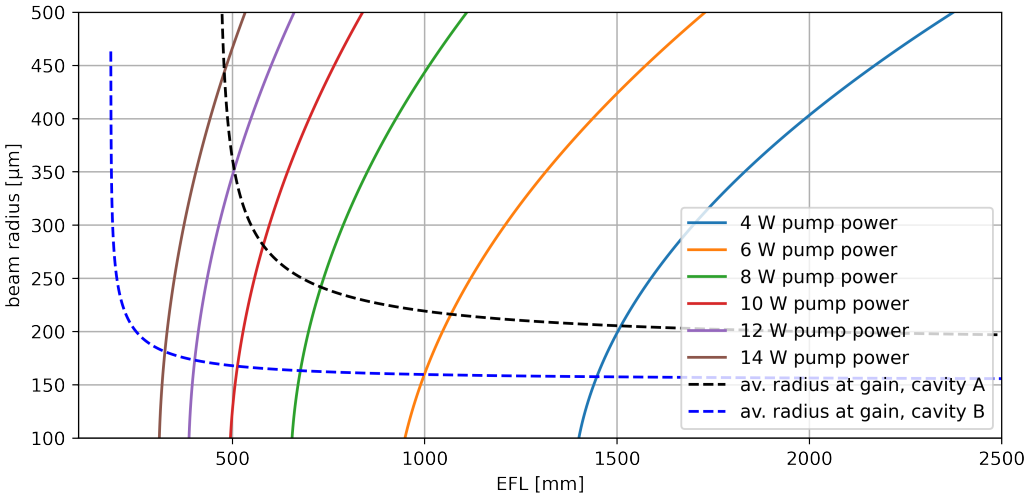

Figure 4.13: For various pump powers at 395 µm diameter, the effective focal length (EFL) is depicted as a function of Gaussian probe beam diameter. The EFL-dependent eigenvalues are plotted for example laser cavity close to stability limit at 14 W pump power (cavity A) and the results for the cavity under test in this work (cavity B) are plotted.

In cavity designs, where the laser is operated in proximity of a stability limit, the impact of the EFL on the size of the stable solution beam in the cavity can be very large. Depending on the cavity setup and the direction and rate of resonant beam diameter change with effective thermal lens, the size change of the Gaussian beam penetrating through the thermal lens can have a weakening or strengthening impact of the effective thermal lens values as a function of pump power. As an example, a laser cavity setup described in [92] was scaled by a factor of five in size to approximately match the pump spot size analysed in this work. The cavity setup of [92] and a the configuration used as comparison, are listed in table 4.3.

The linear standing wave cavity is configured with mirrors M_n and lengths L_n in direction towards the outcoupling mirror: M1 - L_1 - gain element - L_2 - M2 - L_3 - M3 with an angle of incidence of 5.5° at M2 in the transverse direction. The scaled cavity is referenced to as "cavity A".

parameter	reference cavity [92]	cavity A
M1	r = 250 mm	r = 1250 mm
M2	r = 300 mm	r = 1500 mm
M3	r = ∞	r = ∞
L_1	98 mm	1240 mm
L_2	197 mm	1490 mm
L_3	198 mm	1490 mm

Table 4.3: Cavity parameters of [92], and scaled "cavity A" values for comparison.

This cavity configuration has a strong dependency of resonant beam radius on the thermal lens focusing power around 500 mm effective focal length. The correct eigenvalue for the resonant beam (see section 3.3) is determined by the corresponding effective thermal lens. In figure 4.13, the beam radius dependency in the gain medium is plotted with respect to the effective focal length for both cavity setups described. Since the cavities are astigmatic, for the following simplification the average radii of sagittal and tangential beam extension are taken into account. The crossings of pump-dependent lines of beam radius vs. EFL and the eigenvalue indicate the effective focal length values that are dominant for the resonant beam. From this, the effective focal length inside this specific cavity configuration can be determined. The plot also shows the EFL results for the cavity configuration chosen throughout this work. These are labeled "cavity B".

The thermal lens increases its power in a non-linear fashion with increasing absorbed pump power. Figures 4.14 shows the computation results for various probe diameters. The plots also show the thermal lens refractive power (and focal length) in the resonant example cavity with scaled configuration values (cavity A), where an increasing focusing power induces a strong increase of the resonant beam size in the gain chip. In such case, the value of the effective focal length saturates with increasing pump power when approaching the stability limit at approximately

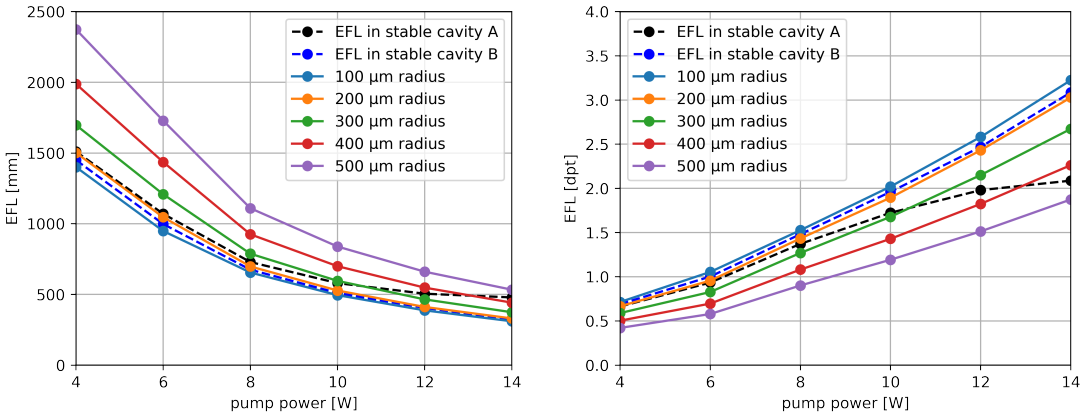

Figure 4.14: Effective focal length (EFL) values for 395 µm pump diameter and various static Gaussian probe beam radii. For comparison, the plots also show (dashed lines) the EFL for the respective (EFL-dependent) beam radius reached in the simulation of the example cavity A, that is configured close to a stability limit. The results for cavity B represent the EFL development based on the simulation of the cavity configuration chosen for the experiments througout this thesis. The left-hand plot shows the values as focal length, and the right-hand plot as focusing power.

465 mm effective focal length in this scenario. The cavity under test in this work (cavity B) is operated further from the stability limit. Consequently, the change of EFL within the pump power range of interest is not as significant.

4.3 Dynamic Response of the Thermal Lens

In electrically pumped edge-emitting laser structures, modulation of pump current is very commonly used for stabilization of the laser sources (see, for instance, [93] and [94]). This phenomenon, utilized in Fabry-Perot and ECDL cavities, relies on a carrier-density-dependent refractive index that induces a change in the optical path length through the gain medium ([95]) upon injection current modulation. In typical ECDL setups, the gain medium is 1 mm to 2 mm in length. Since the interaction length along the resonant laser radiation propagation in VECSEL and MECSEL is three orders of magnitude smaller, this effect alone is not expected to produce useful results. Along with the minimal impact of optical path length change, the relative change in cavity FSR is also comparably small, since membrane-type optically pumped setups of Watt-level power typically require

tens of millimeters of resonator length for sufficient transverse mode narrowing. Consequently, in order to achieve useful frequency modulation of the cavity, the current modulation would require a modulation amplitude that would significantly degrade the intensity noise performance.

In a MECSEL, the transparent intra-cavity heat spreader is additionally impacted by the pump intensity. This impact is purely thermal in nature, induced by the temperature-dependent refractive index. As of now, the dynamic response of the phase delay in MECSEL chip assemblies has not been described in the literature. In the following, a finite element model will be used to analyze thermal and optical response upon a sinusoidal modulation of pump power. These results are then compared with measurement results from a weakly locked MECSEL assembly with intra-cavity frequency conversion. Further details on the laser setup are given in chapter 5.

In contrast to piezoelectric actuators, a purely current-induced frequency modulation is advantageous, since it is not prone to mechanical vibration and resonances. This could potentially increase the feedback bandwidth compared to pure PZT actuation, while avoiding the need to introduce electro-optical modulators with large actuation voltages.

4.3.1 Numerical Analysis

The thermal finite-element model described in section 4.2 provides not only means of computing the steady state condition with a certain pump power and amplified stimulated, as well as spontaneous emission. It also is capable of providing time-dependent data of the thermal response upon modulation of the pump intensity.

The progress of thermal distribution in the chip, highly resolved in time (67 µs sampling interval), was calculated based on a step function from 0 W pump power to 12 W. Again, a 395 µm pump spot diameter inside the MECSEL membrane was considered. All further parameters are identical to the numerical analysis in the previous section. Figure 4.15 shows the computation results of the average temperature distribution along the laser propagation axis. Here, various radial

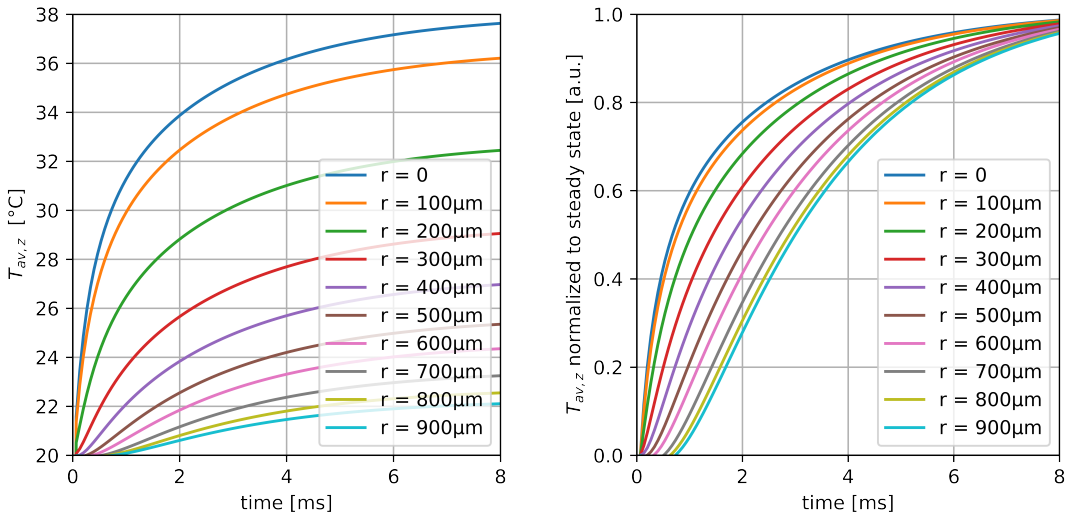

Figure 4.15: Left plot: Average temperature in beam propagation direction z ($T_{av,z}$), calculated for a step function from 0 W to 12 W pump power, plotted for the center axis and several radial distances from the center. Right plot: The same data, normalized to the steady state condition, indicating a radial dependency of the heating time constant.

distances from the center of pump and lasing radiation are plotted. The left-hand figure shows the absolute temperature development upon initiation of pump light absorption, while on the right-hand figure, the data at different radii are normalized to the steady state in thermal equilibrium. In this plot, it becomes obvious that the temporal response of the MECSEL structure is highly dependent on the distance from the center of the laser beams. In the center, where the largest temperature change occurs, the temperature rises to half of the steady-state value within about 500 µs. An almost identical results is seen at 100 µm radial distance from the center, where the readius is at the margin of leaving the absorption area of the MECSEL membrane pumped with 395 µm diameter. Outside of the directly pumped region, the temperature response is delayed in time. Since the laser beam is of Gaussian nature, the data outside the center area has an impact on the response of the resonant beam.

In order to evaluate the maximum laser output frequency control bandwidth, the phase delay of pump-induced thermal distribution the MECSEL assembly is an important indicator. From the thermal finite-element model described above, a

steady state is calculated at 10 W absorbed pump power. Based on this state, a sinusoidal modulation of pump power (10 % amplitude modulation) is processed over 150 time steps (10 periods of 15 data points). The input modulation is then related to the temperature modulation at the model's nodes. Similar to the process of thermal lensing analysis, the temperature is interpolated into Cartesian coordinates and averaged along the z-axis of the laser, at various distances from the center axis. The optical path length modulation is determined using equation 4.9 and values from the table 4.2.

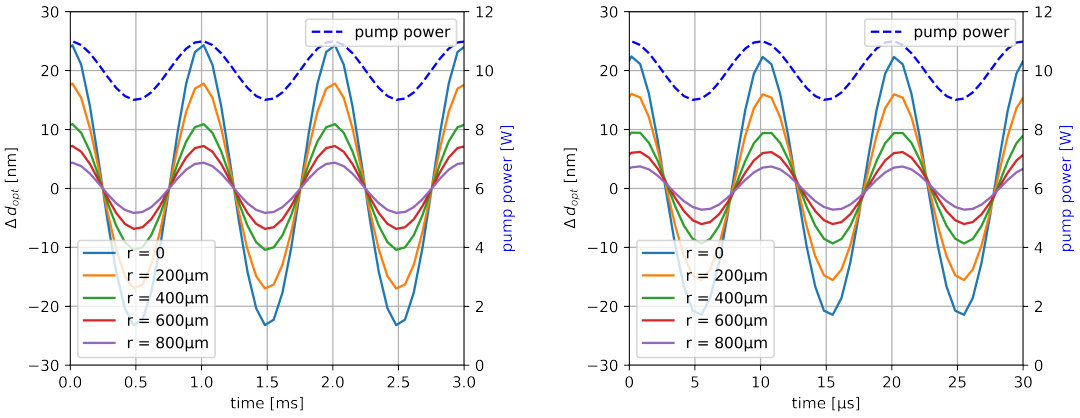

Figure 4.16: Modulation of the optical path length (single pass) modulation upon sinusoidal modulation of the pump power, plottet for different radii of distance from the center of the laser radiation. Left plot: Results for 1 kHz modulation frequency, showing a very small phase delay. Right plot: Results for 100 kHz modulation frequency, showing a significant phase delay, which increases with the distance to the pump excitation center.

In order to relate the optical length modulation of the chip to the laser frequency modulation, the dominant relationship is expected to be the change in resonance conditions due to the change in cavity length. However, two other potential influencing factors can be considered. Apart from shifting the frequency of the resonant photons by velocity-induced Doppler shift (see below), the emission frequency of the laser is prone to a temporal lag with the average time that photons of a specific frequency occupy the cavity while tuning. In section 2.4, it is shown that the gain of the MECSEL assembly is less than 5 % for efficient setups.

Hence, the effective outcoupling cannot exceed the value of 5 %, resulting in an average round-trip number of $n_{cav} = 20$. Given a round-trip time t_r of

$$t_r = \frac{2L_{opt}}{c}, \tag{4.17}$$

the round-trip time at an optical cavity length of $L_{opt} = 70\,\text{mm}$, multiplied by $n_{cav} = 20$, results in an average photon lifetime in the cavity of $t_{photon} = 467\,\text{ps}$ or a frequency of $f_{max} = 107\,\text{MHz}$. Due to the Doppler shift, the photon lifetime in the cavity is not a significant parameter: When tuning the cavity length by modifying the optical path length, the photons traveling through the changing optical path length observe relativistic Doppler shift. When tuning to shorter cavity lengths, this Doppler shift compresses the optical path and induces shift toward higher frequencies or lower wavelengths. Similarly, shortening the optical path length also shifts the resonance of the cavity to higher frequencies. With a tuning velocity of v and $\beta = v/c$, the initial frequency f_0 is shifted to f by the Doppler factor [96], assuming the velocity coincides with the direction of the traveling wave:

$$f = f_0 \frac{1 - 2\frac{v}{c} + \frac{v^2}{c^2}}{1 - \frac{v^2}{c^2}}. \tag{4.18}$$

For tuning velocities much smaller than the speed of light $v << c$ (i.e., a non-relativistic case), this equation is simplified to [97]:

$$f = f_0 \left(1 - 2\frac{v}{c}\right) \tag{4.19}$$

Calculating the Doppler-free change in resonance frequency when tuning a Fabry-Perot cavity, an identical equation can be derived [98]. Since the Doppler shift is applied to the photons each time it experiences the change in velocity (with every round-trip), the frequency slope scales with the cavity length, but the accumulated Doppler shift and change in resonance frequency remain the same. Therefore, it is independent of cavity length. Since the photons inside the cavity

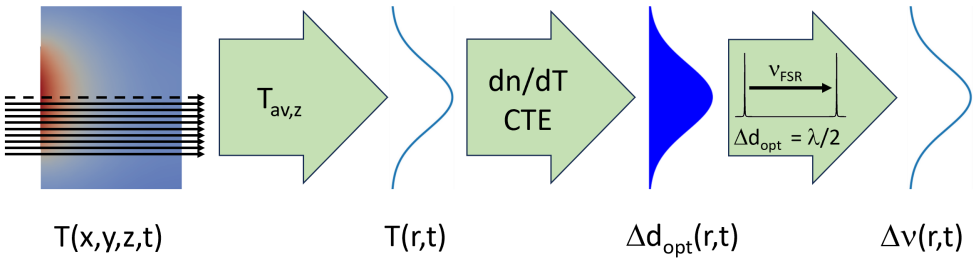

Figure 4.17: Processing pipeline from a time-dependent thermal model to time-dependent laser frequency deviation

are frequency-shifted along with the cavity resonance, the photon cavity lifetime does not limit the output laser frequency modulation bandwidth.

Following the processing path outlined in figure 4.17, the time-dependent temperature distribution along the propagation axis $T_{av,z}$, calculated at several radii from the center, is converted to an optical path length modulation Δd_{opt} (see equation 4.9). Here, the temperature-dependent refractive index and the coefficient of thermal expansion given in table 4.2 are utilized. In order to derive the laser frequency change induced by the optical path length change inside the laser cavity, the optical path length change is related to the shift in the free spectral range of the cavity. At a wavelength of $\lambda = 922\,\mathrm{nm}$, the free spectral range of the example cavity is $FSR = 1.62\,\mathrm{GHz}$. Upon a length deviation of half the resonant wavelength, the resonance of the cavity is shifted by one FSR. This relationship results in a laser output frequency shift of

$$\frac{\Delta\nu}{\Delta d_{opt}} = 3.53\mathrm{MHz/nm}. \tag{4.20}$$

Figure 4.18 depicts the response of the optical path length $\Delta d_{opt}(t)$ and the relative output frequency $\Delta\nu(t)$ upon a sinusoidal pump modulation at 1 MHz with a modulation amplitude of 2 W.

The resonant laser beam has a Gaussian distribution. Hence the radially resolved impact of the temperature induced optical delay needs to be taken into account at various radii from the center. In order to derive a meaningful average, the radial data

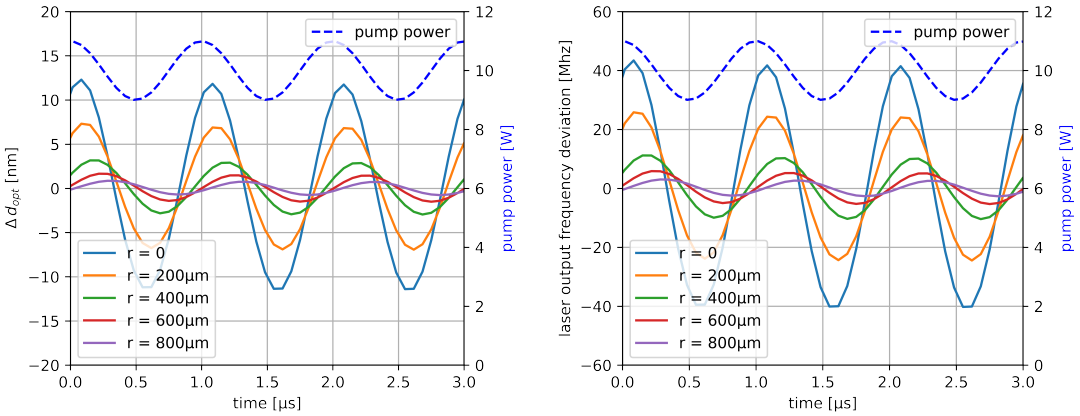

Figure 4.18: Modulation of the optical path length (left plot) upon sinusoidal modulation of the pump power, plottet for 1 MHz frequency and 2 W peak-to-peak power modulation. The right-hand plot depicts the corresponding change in cavity center frequency around the center wavelength.

were weighted by the intensity distribution of a Gaussian beam with $2w_0 = 360\,\mu m$, in disc buckets of 100 µm radial distance (0 µm to 50 µm radius, 50 µm to 150 µm, ...).

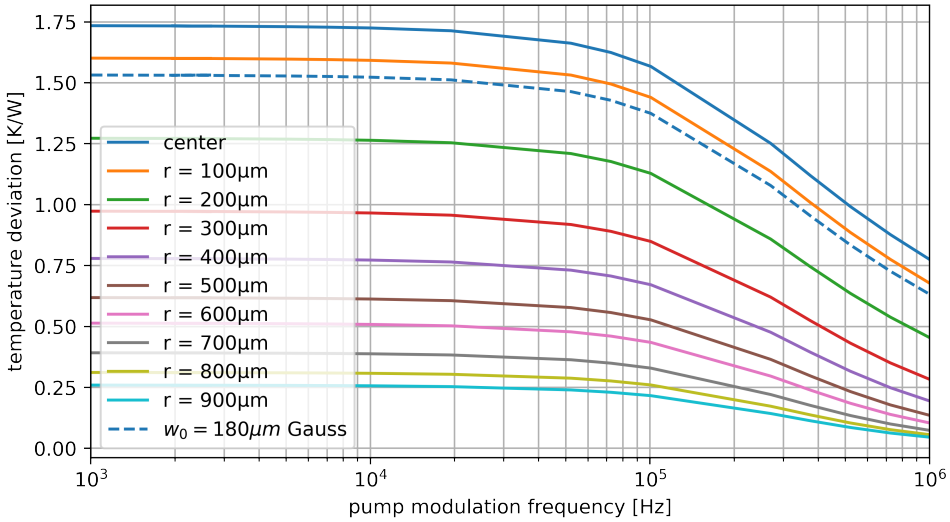

Figure 4.19: Amplitude of laser emission frequency modulation due to pump intensity modulation. The dashed lines show the simulation results for various distances from the beam center. The dashed line represents the averaged frequency modulation for a $2w_0 = 360\,\mu m$ Gaussian beam.

For numerous radii from the center, a set of pump modulation frequencies was computed in the processing pipeline described above. A fast Fourier transform

(FFT) of the data, which is also utilized in the analysis of the experimental data in the next section, provides intensity and phase information of the data sets calculated.

Figure 4.19 shows the simulated laser output emission frequency response at various radial distances from the excitation center. Following the gradient of thermal excitation, the frequency response decreases with increasing distance from the center. At the Gaussian distribution of interest, the frequency modulation amplitude still is significant above 100 kHz, indicating that the pump modulation method is capable of modulating beyond typical accoustic disturbance frequencies (in the <100 kHz regime). Also, the computed phase delay (plotted in figure 4.21 in the next section) is below 90° up to a frequency of 500 kHz.

4.3.2 Experimental Analysis

For the experimental analysis of the modulation transfer characteristics of induced pump current modulations, leading to a modulation in pump power and heat load, a MECSEL system was set up with a cavity length of approximately 70 mm. All detectors were chosen to have a bandwidth sufficient to measure beyond the maximum cavity modulation frequency, determined by the photon cavity lifetime. The pump beam diameter is approximately 395 µm, operating a MECSEL chip with single side Silicon Carbide heat spreader at 922 nm, with intra-cavity frequency conversion into 461 nm emission. For the experiments, a leakage of approximately 2 mW of fundamental resonant radiation was coupled into the single mode (SM) fiber of a 50 % fiber optic coupler (Thorlabs TW930R5A2). One output port of the coupler was connected to an InGaAs biased detector (Thorlabs DET01CFC/M) for monitoring of the laser output intensity. The other output port of the fiber optic coupler was collimated (Thorlabs F110APC-850) and focused (Thorlabs LA4158-B-ML) into a Fabry-Perot interferometer with a Finesse of $\mathcal{F} \geq 1500$ and a free spectral range of 1.5 GHz (Thorlabs SA30-95). The radiation transmitted by the FPI was focused (Thorlabs LA4647-B-ML) onto an amplified InGaAs photodiode with 150 MHz bandwidth (Thorlabs PDA05CF2). A simplified schematic of the measurement configuration is depicted in figure 4.20.

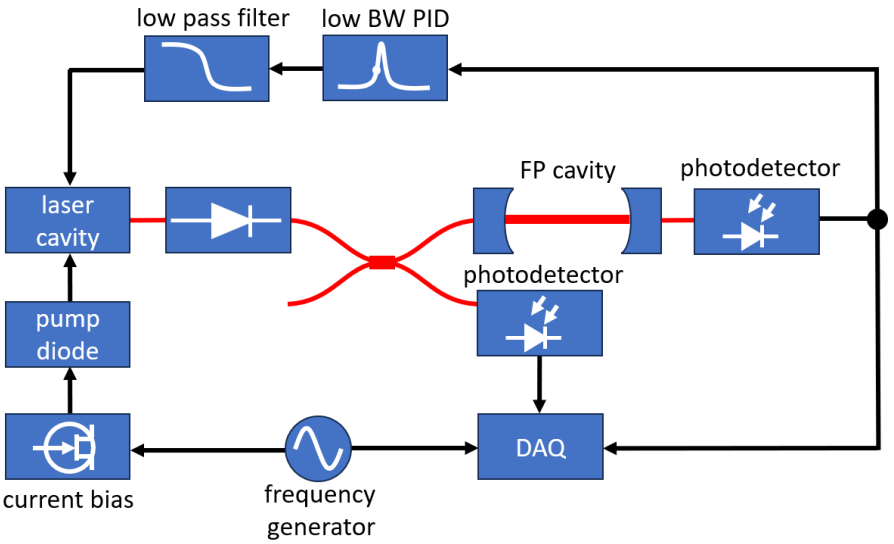

Figure 4.20: Arrangement of the experimental setup for frequency resolved delay measurement of the lasing frequency response to pump current modulation. A MECSEL setup with a low-bandwidth side-of-fringe lock to a Fabry Perot cavity is prone to pump current modulation, inducing laser frequency related intensity variation of the laser intensity transmitted through the FP cavity.

Current modulation of the pump diode supply was induced by introduction of an operational amplifier driven field-effect transistor (FET) that pulls an input-dependent bias current parallel to the constant current supply connected to the pump diode. The residual current through the pump diode was monitored through the voltage over a low resistance shunt, amplified by a non-inverting operational amplifier. The sinusoidal modulation signal was generated by an analog frequency generator (Hameg HM8030-4). All input and output signals were recorded by a 1 Gs/s digital oscilloscope (Tektronix TBS 2000).

The goal of the experiment was to measure the modulation frequency dependent phase delay from the laser system, which then is related and compared to the modeled dynamic response. This parameter is crucial to define the maximum possible control frequency bandwidth of a closed loop lock of the laser output frequency. One option to measure this is to create a beat signal and to analyze the frequency of this signal at high data acquisition rates. Alternatively, a weak (relatively low-frequency) lock onto a partial resonance ("side of fringe") of a Fabry-Perot interferometer was performed. When the frequency transfer function is known,

the transmitted amplitude signal is related back to the relative input frequency of the laser system. The experiment was set up and revised several times. Initially, a low finesse (< 300) Fabry-Perot cavity was chosen in order to ease the weak lock of the laser to the cavity. The need for large laser frequency modulation amplitude to overcome the noise of the transmission signal resulted in data with weak repeatability. The bandwidth of the feedback that holds the laser at the side of the resonance has to be carefully weighed against the lower bandwidth limit of the measurement. The side-of-fringe lock was kept active using a digital servo controller (TEM Messtechnik LaseLock digital) with the servo output low-pass filtered at 30 kHz. This reduces the impact of acoustic vibrations, while allowing a relatively undisturbed measurement of the modulation response at higher frequencies.

In order to verify the measured results, a comparison of data acquired by locking to either side of the resonance at identical target transmission signal heights. The results presented below showed a response shifted by 180° when swapping the sign of the feedback servo control. This was not the case when, for instance, the servo controller had a significant effect at the desired modulation frequency. For low-noise analysis of the data, a set of approximately 100 sinusoidal waves was acquired with 50 cycles of averaging. The data then was Fourier transformed, so that intensity and phase of the modulation input, the laser intensity output and the FPI transmission signals could be related.

In the experiment, the the amplitude modulation of the MECSEL output beam, introduced by the pump current modulation, the pump power and transmission signal through the FP cavity, locked to approximately 50 % of the transmission maximum level, were recorded. The data was acquired with the laser locked to the upwards and downwards voltage slope (or left and right side of the fringe when scanning the FP filter). Analysis of the data is performed with respect to the measured current modulation. In the experiments it became obvious that the current modulation circuit was introducing significant phase shift, with -90° reached at 150 kHz modulation bandwidth. The electronic circuit has not been optimized further within the course of this work.

4.3.3 Comparison of Theory and Experiment

For comparison of the numerical output of the computation with the experimental results, the data are scaled in amplitude to reflect the response per watt of pump power modulation. The phases of the laser frequency response are related to the phase of the input pump power modulation.

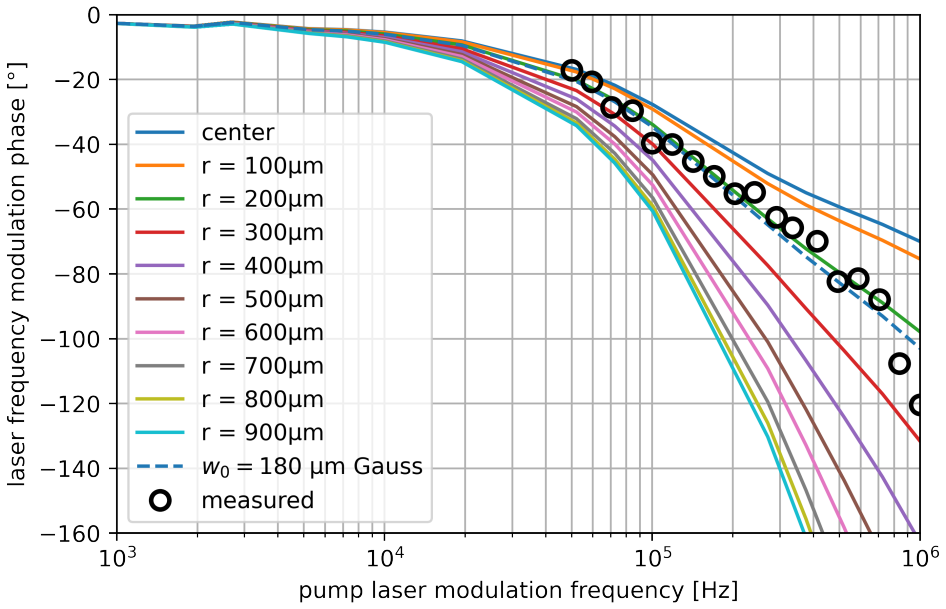

Figure 4.21: Phase of the simulated (dashed and solid lines) frequency modulation of the laser in response to pump intensity modulation, compared to measured data at approximately 180 µm Gaussian beam radius (green circles). The modeled data is plotted for various transverse positions from the pump and laser beam center axis outwards, and for a Gaussian intensity weighed distribution with 180 µm radius.

Figure 4.21 shows the computed phase delay, along with the measurement results. The phase delay is analyzed over various distances from the center of the absorption toward the periphery. The temperature response of the structure is more tightly related to the source of absorption in regions physically close to the heat source. Consequently, the temporal response is delayed in outer regions with respect to the beam center, and the dynamic response depends on the diameter of the intra-cavity radiation. For comparison with the experimental data, the phase delays, depending on the radial distance from the center, were averaged and weighted according to the intensity distribution of a Gaussian beam within defined radial slices. The data sets

at 720 kHz and 1 MHz showed a weak signal-to-noise ratio of about 1:1, so these results are not representative. In order to avoid potential changes of the phase delays in the measurement setup, the amplifications in the setup were not changed over the coarse of the experiment. The results plotted in figure 4.21 indicate that the simulation is in good agreement with the measured results at approximately $2w_0 = 360\,\mu m$ Gaussian beam size at the gain chip inside the cavity under test.

5

Narrow Linewidth Visible MECSEL

In this chapter, visible single frequency generation with harmonic light conversion is introduced, and the most important relationships are given for practical optimization of a laser system setup. Pound-Drever-Hall stabilization is explained and experimental data are provided, utilizing the stabilization technique to couple the MECSEL output radiation to a fixed or tunable external Fabry-Perot cavity. Linewidth and intensity noise are experimentally determined and compared with theoretical limits.

5.1 Harmonic Light Generation

When intense light propagates through material, it can change the optical properties of that material system. This intensity-dependent response of the optical properties of material is referred to as nonlinear optics. In linear optics, the polarization $\mathbf{P}(t)$ linearly depends on the strength of optical field $\mathbf{E}(t)$, which, in turn, linearly relates to the electric field, scaled by the linear susceptibility $\chi^{(1)}$ and the permittivity ϵ_0 [99]:

$$\mathbf{P(t)} = \epsilon_0 \chi^{(1)} \mathbf{E}(t) \tag{5.1}$$

In anisotropic materials, a quadratic nonlinear response to strong optical fields is possible. This nonlinear behavior was first demonstrated in 1961 [17], where the

generation of second-harmonic (SHG) light due to the distortion of the polarization response was experimentally confirmed. This effect can be described by adding a series of higher-order fields and susceptibilities to the polarization term:

$$\mathbf{P(t)} = \epsilon_0(\chi^{(1)}\mathbf{E}(t) + \chi^{(2)}\mathbf{E}^2(t) + \chi^{(3)}\mathbf{E}^3(t) + ...) \tag{5.2}$$

With the presence of the second term, harmonic frequencies of light penetrating through suitable optical media can be induced. Figure 5.1 depicts the simple relationship between the electric field and polarization in presence of the second-order nonlinear term. This term induces an oscillation at twice the frequency of the incoming light. Using this nonlinearity, laser light can be doubled in frequency when suitable material and sufficient light intensity are used.

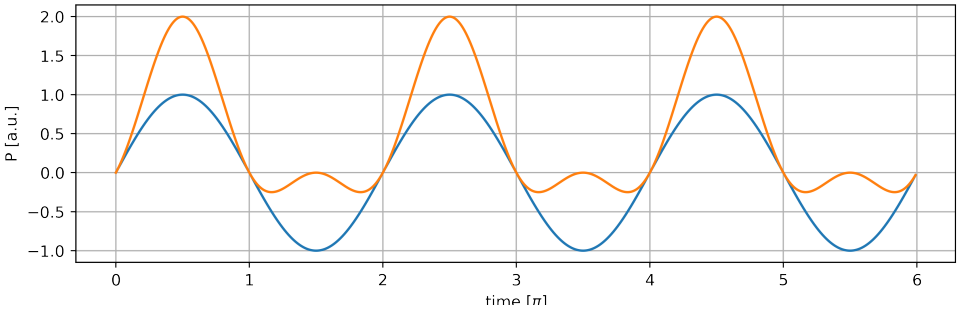

Figure 5.1: Linear (orange) and nonlinear (second order, orange) response of the polarization to the electric field

In MECSEL applications, this effect allows light generated in the infrared spectral regime to be converted into the visible spectrual range. For this conversion to be efficient, the fundamental and second-harmonic light need to be present in the nonlinear optical material with approximately the same relative phase. Due to dispersion in the material, specific configurations are required in order to fulfill this need. The design of material configurations to maintain fundamental and harmonic light at a fixed phase is referred to as "phase-matching". Two approaches for phase-matching are commonly used.

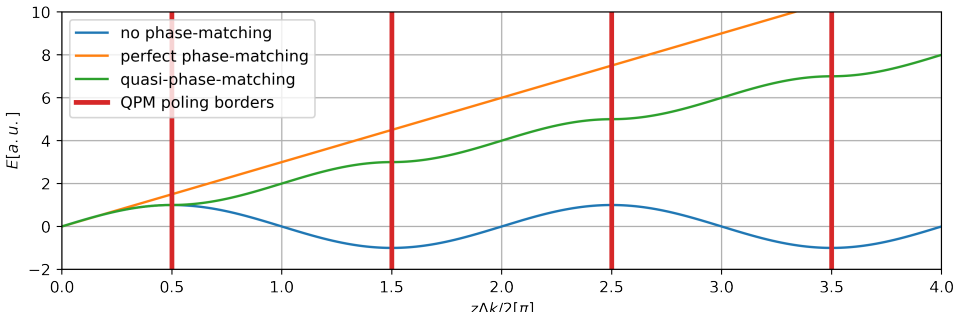

Figure 5.2: Illustration of the electric field development in nonlinear media for the cases of no phase matching, ideal phase matching and quasi-phase matching. The wide lines depict ideal locations for the polarization orientation swap borders in quasi-phase-matched configurations.

One approach is referred to as "quasi-phase-matching" (QPM). In this approach, the nonlinear coefficient is oriented in different directions with respect to the laser polarization, causing the phase mismatch factor Δk to change its sign periodically (see [99] for detailed description of Δk). Using this method, the phase mismatch is partially compensated. The advantage of this method is the possibility to use the nonlinear optical elements at the highest effective nonlinearity. This is rarely achievable in the second approach to phase-matching.

The second approach is utilizing the birefringence in nonlinear optical media, so that the fundamental light (at one polarization with respect to the crystal axes) experiences the same refractive index as the second-order harmonic light, oriented at a perpendicular polarization relative to the travel direction. Figure 5.2 shows the conversion evolution over the propagation distance for different scenarios (no phase matching, ideal phase matching, birefringent phase matching and quasi-phase-matching).

Birefringent phase matching is possible in two ways. In "type I" phase matching, the fundamental wavelength polarization (E_1 and E_2) and the polarization of the second-harmonic radiaton (E_3) is oriented perpendicular to each other. When the second-harmonic radiation polarization aligns with the ordinary (o) axis of the nonlinear medium, the phase matching is referred to as "positive" and as "negative" in the opposite case. "Type II" phase matching occurs when the fundamental

photons are polarized both along the extraordinary (e) and ordinary axes. This is illustrated in figure 5.3.

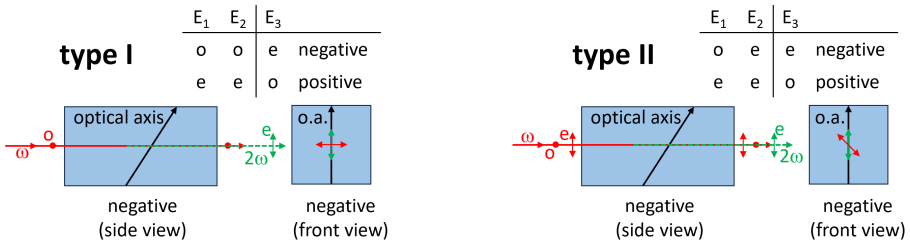

Figure 5.3: Phase-matching types in birefringent phase matching

The selection of a suitable nonlinear medium includes consideration of the transparency of the medium at both the fundamental and harmonic wavelengths, the effective nonlinear coefficient d_{eff}, damage threshold and phase-matching conditions. Additionally, the stability of the crystals with respect to environmental influences, especially humidity, must be taken into account. Significant tilt of the crystal axis in respect to the light propagation axis can lead to walk-off of the second-harmonic light ray, thereby reducing the transverse beam quality. This effect becomes most pronounced when the crystal axes must be rotated close to or at 45° relative to the polarization axis of the second-harmonic beam. The nonlinear coefficient is related to the second harmonic susceptibility $\chi^{(2)}$ with

$$d_{eff} = \frac{1}{2}\chi^{(2)}. \tag{5.3}$$

Material	Phase-matching type	Nonlinear coefficient d_{eff} [10^{-12}m/V]	Damage threshold [GW/cm²]	Absorption [1/cm²]
KD*P	II	0.37	0.5	0.005
KTP	II	3.18	0.5	0.010
LBO	I	1.06	2.5	0.005
BBO	I	1.94	1.5	0.005
$LiNbO_3$ (5 % MgO)	I	4.7	0.1	0.002
$LilO_3$	I	4.1	0.01	0.002

Table 5.1: Physical parameters of optically nonlinear crystals. Nonlinear coefficients listed for conversion of 1064 nm to 532 nm [100].

Table 5.1 lists some popular nonlinear crystals suitable for second-harmonic generation at the desired wavelengths. For the design and experiments of frequency-doubled MECSEL, lithium triborate (LiB_3O_5 or LBO) was chosen due to the large damage threshold, low hygroscopicity, relatively high effective nonlinear coefficient and small phase-matching angles.

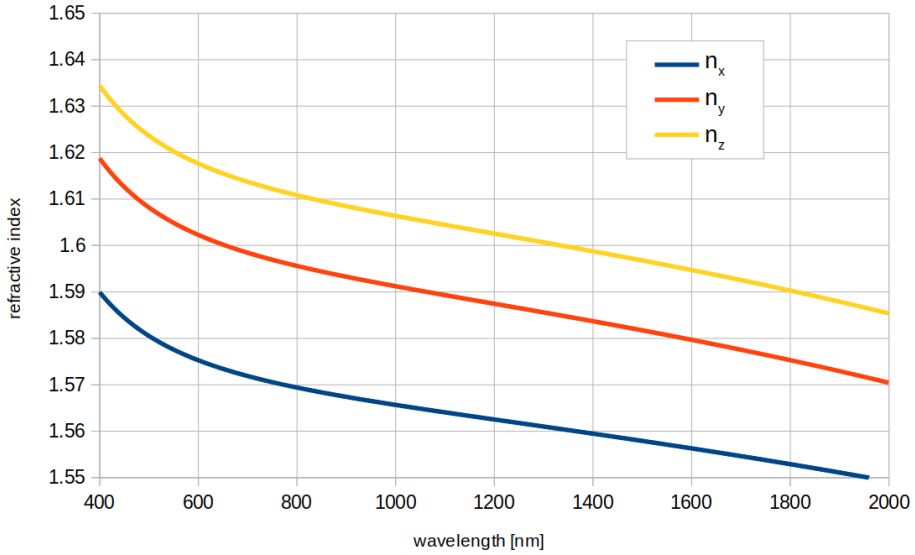

Figure 5.4: Refractive index in the three axes of LBO at 55°C (from [101])

The LBO phase-matching considered in the following is of type I. For the analysis of LBO phase matching properties, the temperature-dependent Sellmeier coefficients as provided in [101] are used.

In figure 5.4, the refractive indices of LBO at 55°C are depicted. Comparing the refractive index values for fundamental radiation in z-axis n_z and second-harmonic radiation in y-axis n_z, it is apparent that these show little difference (in the range of 900 nm through 1145 nm). Consequently, only a small fraction of the lower n_x refractive index is needed in order to fully phase-match these frequency pairs. In the case studied here, this is reached by tilt of the crystal axis around φ. The orientation of the crystal axes and the nomenclature of the angles of the fundamental polarization relative to the crystal axis system is depicted in figure 5.5. The crystal orientation chosen for the MECSEL experiments is the YZ plane with $\theta = 90°$.

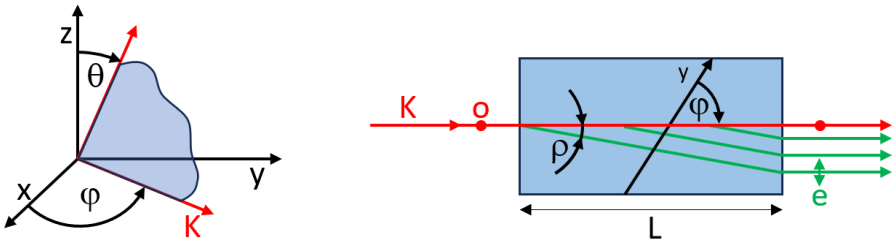

Figure 5.5: Definition of axes and angles in three-axial crystals like LBO (left) and an illustration of birefringent walk-off (right)

The resulting effective refractive index $n(\varphi)$, where in this case $n_o = n_y$ and $n_e = n_x$, is calculated from:

$$\frac{1}{n(\varphi)^2} = \frac{\cos^2(\varphi)}{n_o^2} + \frac{\sin^2(\varphi)}{n_e^2} \tag{5.4}$$

Based on equation 5.4, the angle φ for ideal refractive index matching is determined at a given temperature. The respective effective nonlinear coefficient d_{eff} is calculated with respect to the axis system using $d_{32} = (-0.89 \pm 0.09)\,\mathrm{pm/V}$ [102]:

$$d_{eff}(I) = d_{32} \cos\varphi \tag{5.5}$$

In birefringent material, the Poynting vector may differ from the vector of the wavefront, leading to an angle at which light polarized along the extra-ordinary axis propagates. This is the frequency-doubled radiation in the case considered, causing the frequency-converted photons to drift off the fundamental wavelength propagation axis. Since the frequency-converted photons are created at all longitudinal positions of the nonlinear crystal, this "walk-off" leads to a transverse broadening of the Gaussian beam distribution in the extra-ordinary axis, which decreases the beam quality. The walk-off angle ρ is determined by:

$$\rho = \arctan\left(\frac{n_o^2}{n_e^2}\tan\varphi\right) - \varphi \tag{5.6}$$

In figure 5.6, the phase matching conditions for various wavelengths with respective walk-off angles and the effective nonlinear coefficient are summarized.

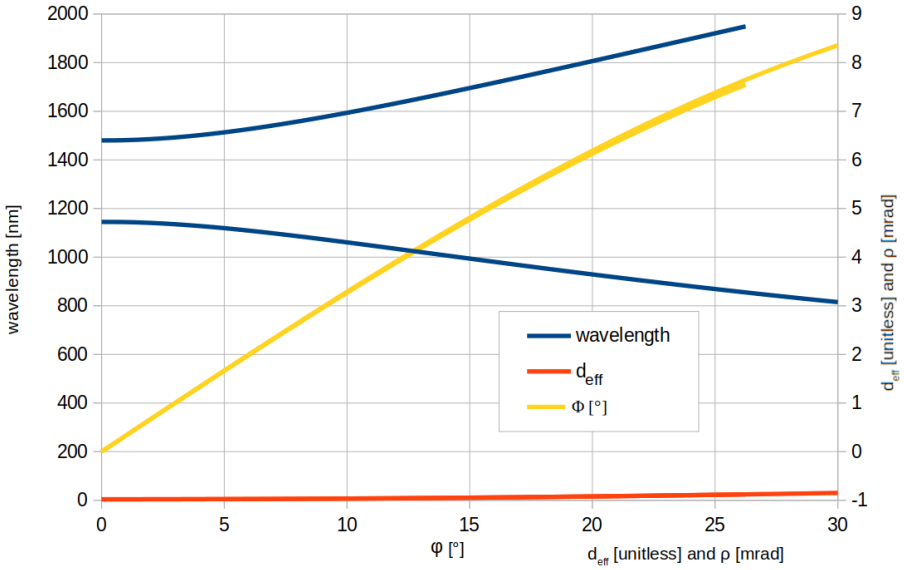

Figure 5.6: Phase-matching angles φ, effective nonlinear coefficient d_{eff} and walk-off angle ρ for LBO in Type I phase matching

Fundamental wavelengths in the range between 1145 nm and 1480 nm can also be phase-matched, but this requires orientation in the XZ plane, with $\theta = 0°$.

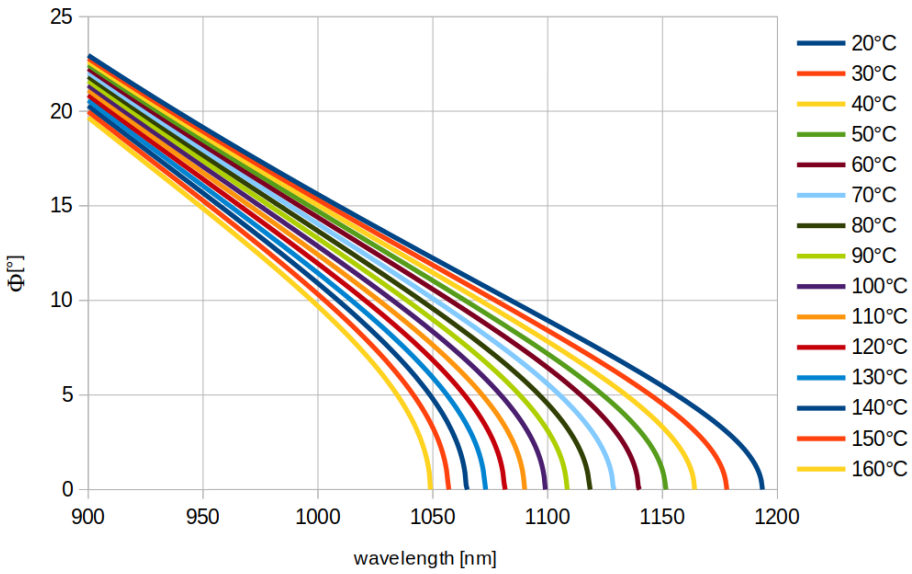

Figure 5.7: Temperature-dependent phase-matching conditions for a selected wavelength range in Type I LBO second-harmonic generation

In practice, the phase matching condition is optimized via adjustment of the phase-matching angle, or the temperature. The temperature dependency of the phase-matching condition is larger at higher values of φ. This is illustrated in

figure 5.7. The phase-matching plots also show the conditions for non-critical phase matching ($\varphi = 0°$). Though LBO has a low hygroscopy compared to other popular nonlinear crystals like BBO, operation well above room temperature has been used in order to prevent moisture from diffusing into the crystals.

The efficiency for the conversion of two photons at the fundamental wavelength into one photon in the frequency-doubled wavelength depends on the effective nonlinear coefficient, the phase matching condition and the power density of the incident light throughout the propagation through the nonlinear crystal. Boyd and Kleinman published an extensive paper [103] on the conversion efficiency with respect to the phase matching condition and beam parameters for ideal Gaussian beams. Their formulas are being utilized in the following, only extended by the beam quality factor M^2, which is a simplification to summarize lateral broadening of an ideal Gaussian beam waist. It can easily be determined in experiments by observing the difference between the ideal and measured value of w_0 for the respective beam divergence. The M^2 factor acts like an increase in wavelength, leading to a broadened beam waist diameter when $M^2 > 1$, as in the following relationship for the Gaussian beam waist distribution along the longitudinal axis z, with the waist position at z_0:

$$w = w_0 \sqrt{1 + \left(\frac{M^2 \lambda (z - z_0)}{n \pi w_0^2} \right)^2} \tag{5.7}$$

Therefore, the Boyd-Kleinman confocal parameter b is extended by M^2:

$$b = \frac{2\pi n_f w_0^2}{\lambda_0 M^2} \tag{5.8}$$

Figure 5.8 illustrates the definition of angles as described in [103]. In terms of conversion efficiency, the ideal longitudinal focus position f of the beam waist is centered in the crystal of length L ($f = \mathrm{L}/2$). The focusing parameter is defined as $\xi = \mathrm{l/b}$, and μ as $\mu = \frac{l-2f}{l}$. In the practical implementation of the MECSEL setup (as shown in figure 3.15, the SHG crystal is placed closely to a plano mirror that

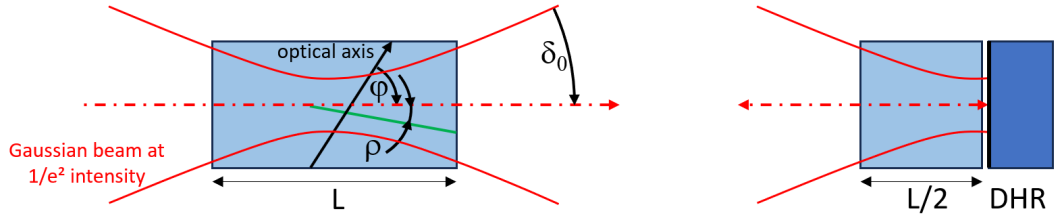

Figure 5.8: Crystal parameter definition as per Boyd and Kleinman (left) and the configuration implemented in the MECSEL setup, utilizing a plano mirror (DHR) very close to the crystal end facet (right)

reflects both fundamental and frequency-doubled light (dual highly reflective mirror "DHR"). Since the mirror is a flat end mirror of the cavity, the beam waist is forced to coincide with its surface. The SHG crystal is penetrated twice per round-trip in the cavity. Since the calculations are based on single-pass transmission, the effective crystal length considered is twice the physical length of the crystal. The following calculations still are valid. The calculation takes the walk-off angle ρ into account, but neglects depletion of the fundamental power. Hence, the calculations become less precise for high total conversion efficiencies. For the cases considered here, where the intended total loss in the cavity is less than 10 %, equation 5.8 offer a suitable approximation for optimization of the cavity layout concerning crystal length and waist diameter.

The absorption α is factored into $\kappa = 1/2\alpha b$ for the calculation of conversion efficiency. The vacuum speed of light is represented by c_0, the electric constant ϵ_0, and the refractive index n_f, the k-vector k_f and the frequency ω_f are defined at the fundamental wavelength. With the far-field divergence δ_0, β is defined, utilizing the walk-off angle ρ:

$$\delta_0 = \tan^{-1}\left(\frac{\lambda_0 M^2}{\pi w_0}\right) \tag{5.9}$$

$$\beta = \rho/\delta_0 \tag{5.10}$$

The calculation also allows the consideration of non-ideal phase matching with the phase mismatch factor σ, which in the following computations is set as 1,

indicating ideal phase matching conditions. Integrating over the intensities of the Gaussian distribution, the Boyd-Kleinman factor $h(\sigma, \beta, \kappa, \xi, \mu)$ is defined [103]:

$$h(\sigma,\beta,\kappa,\xi,\mu) = \frac{1}{4\xi} e^{\mu\alpha l} \iint_{-\xi(1-\mu)}^{\xi(1+\mu)} d\tau d\tau' \times \frac{\exp\left(-\kappa(\tau'+\tau)+i\sigma(\tau'-\tau)-\beta^2(\tau'-\tau)^2\right)}{(1+i\tau)(1-i\tau')} \tag{5.11}$$

Using the Boyd-Kleinman factor h, the normalized conversion efficiency η_{norm} is derived as:

$$\eta_{norm} = h \frac{2\omega_f^2 d_{eff}^2 k_f}{\pi n_f^2 n_{SHG} \epsilon_0 c_0^3} \tag{5.12}$$

The conversion efficiency $\eta_{SHG} = P_{SHG}/P_f$ is finally used to compute the efficiency of second-harmonic-generation configurations by:

$$\eta_{SHG} = \left(\tan^{-1}\left(\sqrt{\eta_{norm} l P_f}\right)\right)^2 \tag{5.13}$$

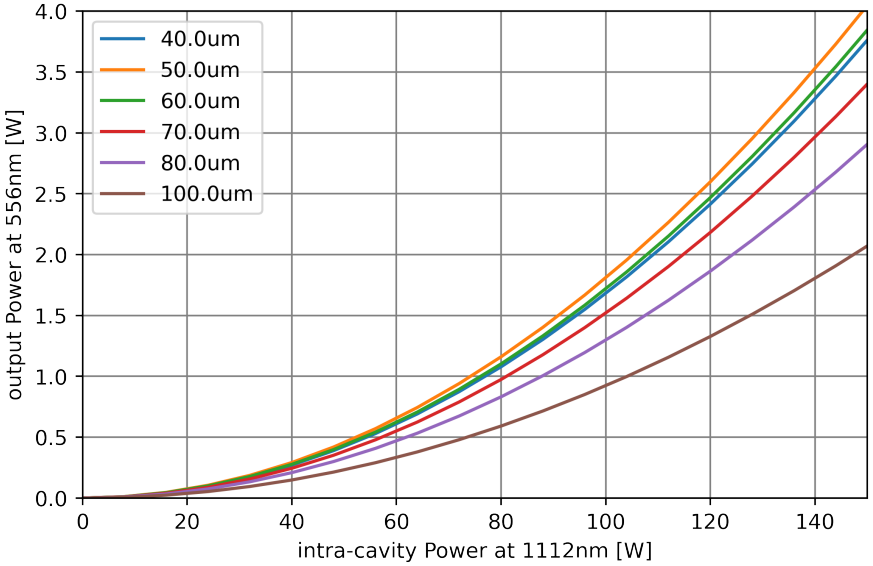

Figure 5.9: Calculated SHG conversion efficiencies as a function of fundamental power, for different waist diameters w_0 and a crystal length $L/2 = 16mm$

Implementing realistic values from the cavity setup (see section 3.3.1), the power-dependent conversion efficiency development for different fundamental beam sizes,

and crystal lengths, were computed. Figure 5.9 depicts a scenario utilized in the experiments described hereafter. The conversion efficiency increases with decreasing beam radius values, starting with $w_0 = 100\,\mu m$, reaches a maximum at $w_0 = 50\,\mu m$, and decreases again with even smaller beam diameters or larger divergence.

For the resonator design including intra-cavity frequency conversion, the different aspects - relatively large pump diameter, small beam size and short cavity length - require well-balanced compromise of intra-cavity dioptric powers, thicknesses of the filter elements and length of the SHG crystal. This was considered in the cavity setup optimization described in section 3.3.1, resulting in a conversion efficiency of $\eta = 24\,\%$ at a maximum single frequency output power of 1.7 W (see section 3.3.3).

5.2 Line Stabilization

The laser frequency was locked to the relatively fixed frequency of an external Fabry-Perot cavity in order to analyze the laser frequency phase response and to evaluate the frequency width and stability. The locking was performed either with a "side of fringe" method, where the laser frequency was held at a partial transmission through the Fabry-Perot cavity, or using the "Pound-Drever-Hall" (PDH) method [104],[105]). This method does not require intra-resonator elements, which are necessary in the alternative Hänsch-Couillaud method, [106], where polarizing elements are required. In both approaches, an error signal ϵ is created, which has a different sign depending on the sign of the frequency deviation of the laser frequency relative to a multiple of the Fabry-Perot free spectral range frequency.

Following up on the Etalon description in section 3.1.2, the spectral frequency distance in between two resonances of a Fabry-Perot cavity Δf_{FSR} is given by:

$$\Delta f_{FSR} = \frac{c}{2L} \tag{5.14}$$

Assuming the use of two mirrors with identical reflection coefficient r, the energy reflection ratio of the cavity with regard to the laser center frequency ω can be written as:

$$F(\omega) \equiv \frac{E_{ref}}{E_{in}} = \frac{r\left(e^{i\frac{\omega}{\Delta f_{FSR}}} - 1\right)}{1 - r^2 e^{i\frac{\omega}{\Delta f_{FSR}}}} \tag{5.15}$$

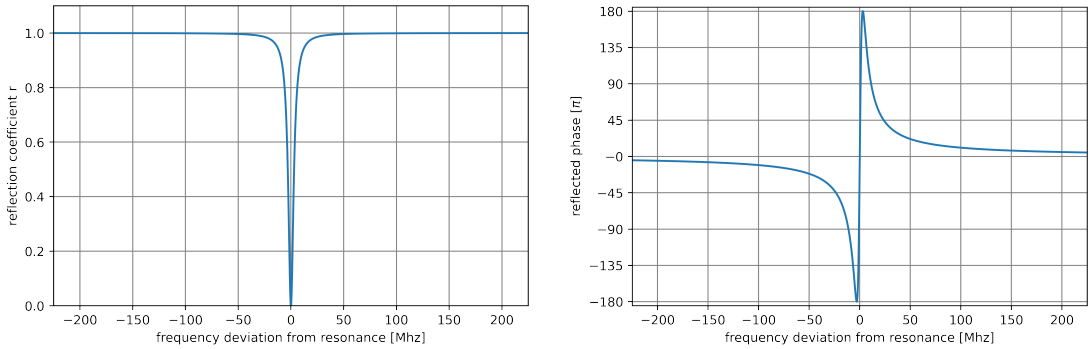

(a) Amplitude **(b)** Phase

Figure 5.10: Reflectivity of an ideal Fabry-Perot cavity with $r = 0.999$ and $\Delta f_{FSR} = 1.5\,\text{GHz}$

The result is a complex number, so that both the phase and the intensity of the reflected signal can be calculated. These are depicted in figure 5.10. An ideal cavity with identical reflectivities on both ends provides a perfect transmission in case of resonance. In practice, this is limited by intra-cavity losses like scattering and absorption, and refractive losses due to imperfect matching of the incoming transverse mode parameters relative to the ideal resonance parameters in the cavity. Also, spherical aberration could be a factor reducing the quality of the cavity resonance, especially in short cavities with small mirror radii of curvature.

The phase of the reflected signal changes its sign when tuning over the resonance. This is crucial for the generation of an error signal. In order to be able to measure the reflected phase, a phase modulation with the modulation depth β is added to the laser light entering the stabilization setup. The modulation frequency f_{mod} needs to be significantly smaller than the cavity free spectral range. In the examples computed, as well as in the experimental setup, the modulation frequency was chosen at $\Omega = 150\,\text{MHz}$. Using the center frequency and the modulation frequency, the term χ is formed. In the phase mixing process, both the addition as well as the subtraction of the modulation frequency are incorporated:

$$\chi = F(\omega)F(\omega+\Omega) - F(\omega)F(\omega-\Omega) \tag{5.16}$$

With χ, the reflected power $P_r(\omega)$ of the phase modulated light may be described, in this case ignoring the higher mixing of $2\,\Omega$:

$$\begin{aligned} P_r(\omega) = P_c|F(\omega)|^2 + \tfrac{1}{4}P_c\beta^2\Big(|F(\omega+\Omega)|^2 + |F(\omega-\Omega)|^2\Big) \\ +P_c\beta\Big(\mathrm{Re}\Big(\chi(\omega)\Big)\cos(\omega t) + \mathrm{Im}\Big(\chi(\omega)\Big)\sin(\omega t)\Big) \end{aligned} \tag{5.17}$$

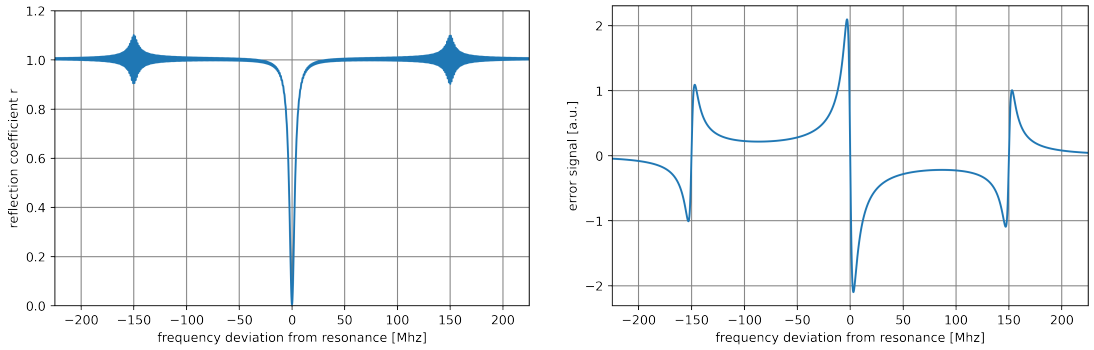

(a) Reflex intensity **(b)** Error signal intensity

Figure 5.11: Cavity reflex amplitude with phase modulation sidebands at $\Omega = 150\,\mathrm{MHz}$ and corresponding error signal

Though not resolved in the plot, the modulation frequency can be seen on the reflected signal shown in figure 5.11. To analyze the phase change induced by the cavity in the reflected signal, a fast photodiode detects the signal. The amplified photodiode signal then is mixed with the initial modulation frequency, so that a phase offset of the two identical frequencies initiates a DC offset of the mixed signal. In order for this DC offset to be zero exactly at resonance, the relative phase in between the optical detector signal and the initial modulation frequency needs to be controlled. The phase is adjusted by the use of phase-delay electronic circuits or a proper choice of electrical lengths. The modulation signal is also present in the output of the mixer, and filtered by an appropriate low pass filter, sufficiently cutting off the modulation frequency, but allowing sufficient frequency bandwidth for agile feedback control of the laser system. Figure 5.11 depicts a typical PDH

error signal, showing exactly one slope through the zero crossing with a negative sign. This signal can directly be taken as a feedback to a servo control loop in order to either stabilize the Fabry-Perot cavity to the laser or vice versa. The error signal can be derived to this form [105]:

$$\epsilon(\omega) = 2\sqrt{P_c(1+\beta)} \cdot \mathrm{Im}\Big(F(\omega)\overline{F(\omega+\Omega} - \overline{F(\omega)}F(\omega-\Omega)\Big) \tag{5.18}$$

Since the laser output is linearly polarized, and the polarization state entering the Fabry-Perot cavity is not relevant, the error signal can efficiently be detected in a "poor man's isolator" approach. In order to do so, the laser light is led through a polarizing beam splitter and then retarded to a circular polarization state using a birefringent quarter-wave plate or equivalent methods. The reflected signal is then transferred into a linear polarization again by the retarding element, but the returning light is reflected by the polarizing beam splitter, where it can be detected by a photodiode.

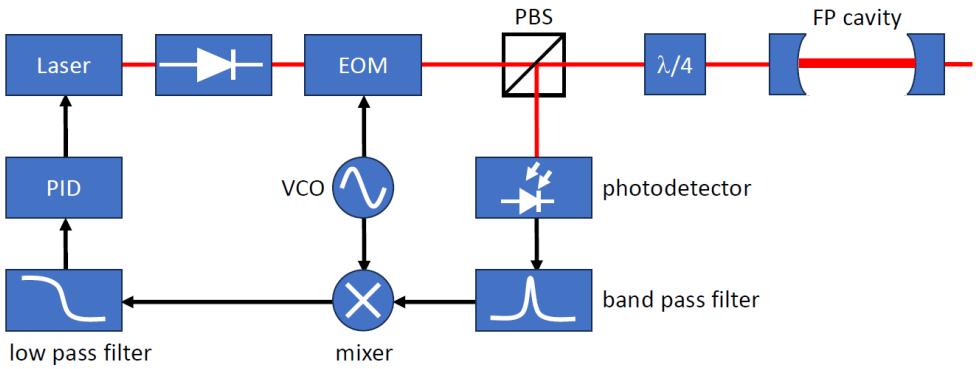

Figure 5.12: Pound-Drever-Hall locking setup using a voltage-controlled oscillator (VCO) and a band-pass filter to adjust the relative phase of the input signals of the mixer

In the frequency-locking experiments, as set up and depicted in figure 5.12, the fundamental light (922 nm) of a 461 nm MECSEL setup ($\sim$ 70 mm cavity length in air) was coupled into a PM850 fiber. The phase modulation is introduced by a fiber coupled lithium niobate phase modulator (Thorlabs LNY10D2A), driven by a voltage-controlled oscillator (VCO, Mini-Circuits ZOS-200+) set to $\sim$ 150 MHz

output frequency. Collimated by an $f = 6.3\,\text{mm}$ collimator (Thorlabs F110APC-850), the polarized light was directed through a polarizing beam splitter (Thorlabs CCM1-PBS255/M). The retardation into circular polarization was realized using a wavelength-independent Fresnel rhomb (Thorlabs FR600QM). The beam is focused by two 500mm lenses (Thorlabs AC254-050-B-ML) before entering the Fabry-Perot cavity (Thorlabs SA30-95). This cavity has a Finesse of $\mathcal{F} \geq 1500$. The full width half maximum (FWHM) resolution was determined from reflectivity measurements to be 600 kHz. The transmitted signal was monitored by a detector with switchable gain (Thorlabs PDA36A) and analyzed using a frequency-resolved intensity analyzer (Thorlabs PNA1). On the detection path, the light reflected off the polarizing beam splitter was focused (using Thorlabs AC127-019-B-ML) onto an amplified InGaAs detector with sufficient bandwidth (Thorlabs PDA05CF2). The photo detector signal was fed into a band-pass filter with 150 MHz transmission (Mini-Circuits BBP-150+). The band-pass filter served two purposes: By only transmitting the desired modulation frequency well, the signal is cleaned up from other frequency disturbance. Secondly, the phase response of the band-pass filter is frequency-dependent. By adjusting the exact value of the VCO, the relative phase delay can be modified, at acceptable cost of loss in the signal. Finally, the fundamental oscillation and the detected oscillating signal are mixed (Mini-CircuitsZX05-1LHW-S+) and low-pass filtered (Mini-Circuits SLP-30+) at a -3dB cut-off frequency of 32 MHz. As servo controllers for the PID loop, either a digital servo controller (TEM Messtechnik LaseLock digital) or an analog one (Vescent D2-125) were used.

5.3 Linewidth and Intensity Noise

The theoretical limits for frequency bandwidth and intensity noise in lasers have initially been derived by Schawlow and Townes [107]. Nineteen years later, Lax proved [108] that above lasing threshold, the noise limit is only half that of the derivation by Schawlow and Townes [109]. The frequency bandwidth limit $\Delta\nu_{min}$ depends on the full width half maximum of the laser resonator cavity function $\Delta\nu_c$ and the average output power measured P_{av}:

$$\Delta\nu_{min} = \frac{\pi h\nu(\Delta\nu_c)^2}{P_{av}} \tag{5.19}$$

This relationship assumes negligible coupling of intensity and noise, which is believed to be applicable for MECSEL, given the large ratio of total resonator length (tens of mm) and gain length (several µm). For analyzing the resonator cavity function, the TMM method (see section 3.1.4) was used to compute the transmission spectrum, in a configuration of $R_1 \approx 92\,\%$, $R_2 = 30\,\%$ and $R_3 = 98\,\%$, with cavity lengths of $L_1 = 60\,\text{mm}$ and $L_2 = (2\,\text{mm} + \lambda/4)$. This typical operation condition is referenced to throughout this chapter. The resulting transmission spectrum at the center wavelength at unity transmission condition is depicted in figure 5.13, showing an FWHM $\Delta\nu_c = 56.3\,\text{MHz}$.

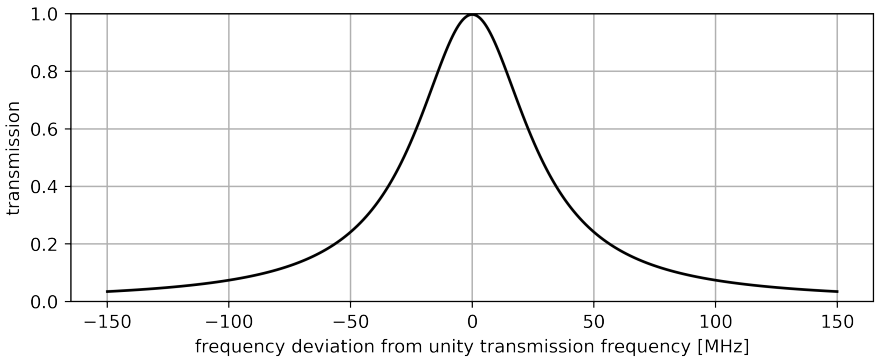

Figure 5.13: Calculated transmission function around cavity resonance in a typical MECSEL configuration, showing 56.3 MHz FWHM

With $P_{av} = 250\,\mu\text{W}$ at the detector, measured at a fundamental wavelength of 1112 nm, the expected lower linewidth limit is as low as $\Delta\nu_{min} = 7\,\text{Hz}$. The intensity noise limit (also referred to as "shot noise" limit) can be directly derived from the average power applied to the detection system:

$$S_{I,SN}(\nu) = \frac{2h\nu}{P_{av}} \tag{5.20}$$

Analysis of relative intensity noise (RIN) of the free-running laser system was performed using a MECSEL at 1112 nm (with intra-cavity frequency doubling),

coupling a portion of the cavity leakage radiation in to a PM fiber. The fiber output is detected by an amplified InGaAs photodiode (Thorlabs DET01CFC/M) with a detection bandwidth of 1.2 GHz. The output is acquired and analyzed using a digital intensity noise analyzer (Thorlabs PNA1) with 10 kΩ input impedance and an 18-bit analog-to-digital converter. The noise floor of the detection and analysis system ($<< -140$ dBc/Hz) was recorded and referenced to the full signal range of 10 V. The RIN of this data set, integrated over the measurement frequency spectrum, was subtracted from laser measurement data. Figure 5.14 shows the result and comparison with the shot noise limit.

It is apparent that the laser reaches shot noise limit above 300 kHz acquisition frequency. The largest specific frequency range that attributes to the laser noise can be seen around 2 kHz to 3 kHz. In acoustic experiments, where a frequency chirp was applied to sound emitted in vicinity of the resonator, this could be proven to be related to mechanical resonances of the optics mounting scheme. Comparison to the pump diode intensity noise spectrum (not depicted) was made. In this spectrum, the ∼2.5 kHz noise elevation is not present.

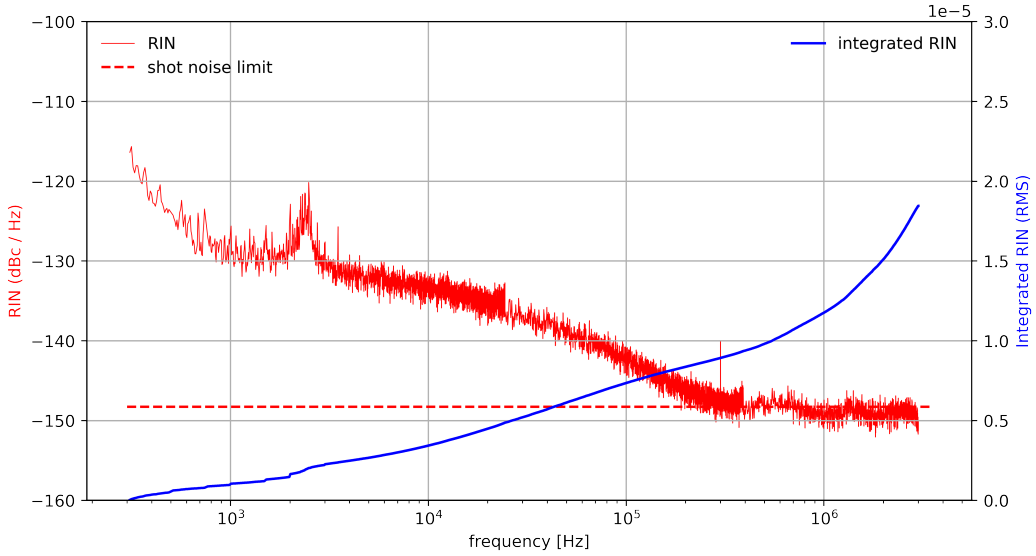

Figure 5.14: Relative intensity noise spectrum of MECSEL setup (left y-axis) and integrated RIN (right y-axis). The dashed line indicates the shot noise limit at measurement conditions, showing that shot noise is reached at ∼300 kHz.

The integrated RIN sums up to $< 2 \cdot 10^{-5}$, or $< 0.002\,\%$, which is comparable to scientific ECDL-seeded amplifier setup results (see, for instance, [110]), showing twice the RIN value, but integrating over a slightly larger range (10 Hz to 10 MHz compared to 300 Hz to 3 MHz in this study).

As a coarse analysis of the laser linewidth while ensuring the presence of only a single dominant longitudinal mode, a commercial scanning Fabry-Perot (SFP) system (Thorlabs SA30-120) was used. It provides a Finesse of $\mathcal{F} \geq 1500$ and a nominal resolution of <1 MHz. Using a 922 nm/461 nm MECSEL configuration, this system showed a side-mode suppression limited by the resolution of the measurement setup. This is expected from the theoretical model, where a fundamental frequency bandwidth limit of 7 Hz was derived. Zooming into the transmission function of the SFP, though, a center frequency jitter could be observed.

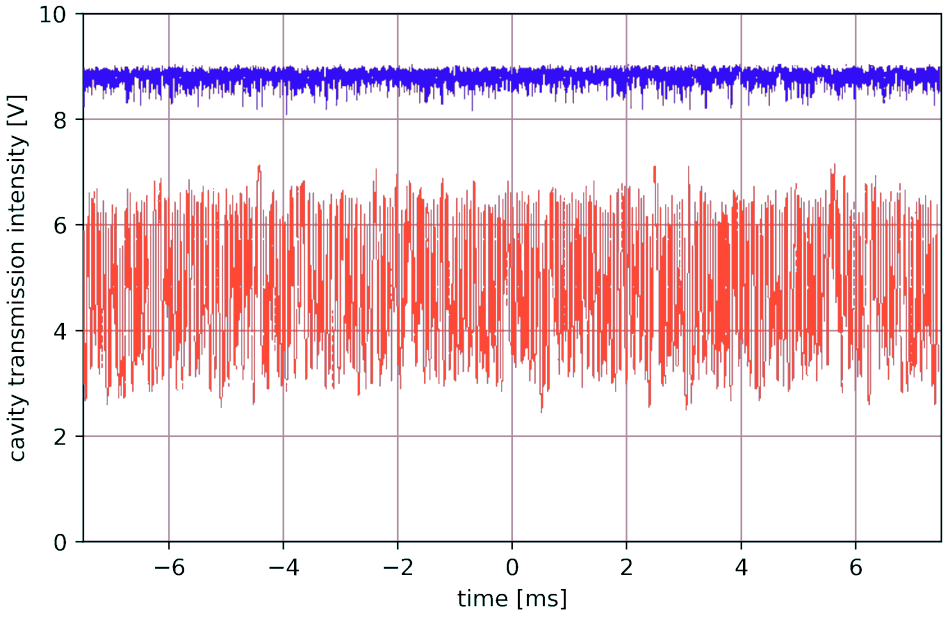

Figure 5.15: Comparison of the transmission intensity signals with low piezo feedback bandwidth (red) and higher bandwidth feedback (blue), measured through a 600 kHz FP cavity of 50 mm length.

The laser was put into a Pound-Drever-Hall lock, using the setup described in section 5.2. In the initial measurements, the lock to the 600 kHz cavity showed severe intensity fluctuations (see figure 5.15, plotted red). The root cause of this

large fluctuation could be related to the limited servo bandwidth applicable, initially limited by a 4.7 kHz resonance of the piezo-driven prism actuator. By stiffening this assembly, the resonance could be raised to 42 kHz, so that the control loop could operate in the acoustically sensitive region of 2 kHz to 3 kHz (see figure 5.14 as comparison) and provide a much smoother transmission function (see figure 5.15 , plotted blue). Relating the RMS noise of the transmission function to the theoretical Fabry-Perot transmission function of the 50 mm-long reference cavity, a long-term (20 ms) measurement indicates a laser line stability within a range of 40 kHz RMS. This, though, can only be considered a valid measurement if the short-term laser linewidth is significantly lower than this stability value, and the integrated width of laser linewidth measurements is substantially broadened by center frequency fluctuations.

A common method of measuring the short-term laser linewidth is creating a beat signal with the laser light output of a single laser system. This can be performed, with potential modifications of the setup, by delaying a portion of the laser light in time. For straightforward signal interpretation, the optical delay length should be chosen longer than the coherence length, L_{coh}, of the laser output. This delay usually is created by guiding one portion of the laser output through a low-loss single mode fiber.

$$L_{coh} = \frac{c}{\pi \Delta \nu} \tag{5.21}$$

The overlap of the two beam paths can be done directly (self-homodyne), which creates a beat node without a frequency offset. This makes the measurement difficult to interpret, as DC offsets directly influence the measurement results. In the self-heterodyne method, one optical path is frequency-shifted by passing through an acousto-optical modulator (AOM). The beat node then is shifted by the modulation frequency of the AOM, detected off the DC signal of the frequency analyzer. A comparison of self-homodyne and self-heterodyne methods, as well as a discussion of short-delay measurements is provided by [111].

The self-heterodyne measurement would, for enabling the measurement of a 10 kHz linewidth, require an optical path length of almost one kilometer. While this is feasible, such setup would not be able to resolve line jittering due to acoustic impacts in the kHz region. For detection of a frequency $f_{det} = 10\,\text{kHz}$ noise, or a detection time of $\tau_{det} = 100\,\mu\text{s}$, an optical delay in the same range would be required, resulting in a fiber length of >20 km ($L_{fiber} = c\tau_{det}/n_{fiber}$), with a refractive index of the fiber of $n_{fiber} = 1.45$. Since this appeared economically impractible, the beat frequency analysis was performed using two uncorrelated laser sources of the same kind.

In the experiment, two identical MECSEL systems were tuned to an almost identical wavelength, so that the difference and sum frequency of the interference could be detected by a photodiode and analyzed with a radio frequency (RF) analyzer. The first laser was locked to fixed cavity as described in section 5.2. The second laser was locked to a piezo tunable cavity in an identical arrangement. A portion of both fiber coupled laser outputs was overlapped using a polarization-maintaining fiber optic coupler (Thorlabs PN850R5A2), where one fiber connector was held adjustable in order to optimize the contrast of the two signals. The beat signal was detected by an amplified InGaAs biased photodiode with 1.2 GHz bandwidth (Thorlabs DET01CFC/M). The voltage signal created was recorded by a real-time Spectrum Analyzer with 9 kHz to 1.5 GHz bandwidth (RIGOL RSA) to display the beat node. In order to control temperature-induced drift of the beat signal, the frequency of the beat signal was compared to a fixed reference frequency of 27 MHz, and an analog output signal, proportional to the difference frequency between beat node and reference frequency, was created using a digital counter and timed integrator (MENLO SYNCRO-CEO with OFD and DXD modules). The output of this frequency comparator was then guided into a PID servo controller (TEM Messtechnik LaseLock digital). The output signal of the controller actuated the piezoelectric line of the reference cavity, through which the second laser was directed. This setup enabled to control the absolute beat frequency by adjusting the set voltage of the servo, and held the beat node at constant frequency for long integration times of the frequency measurements.

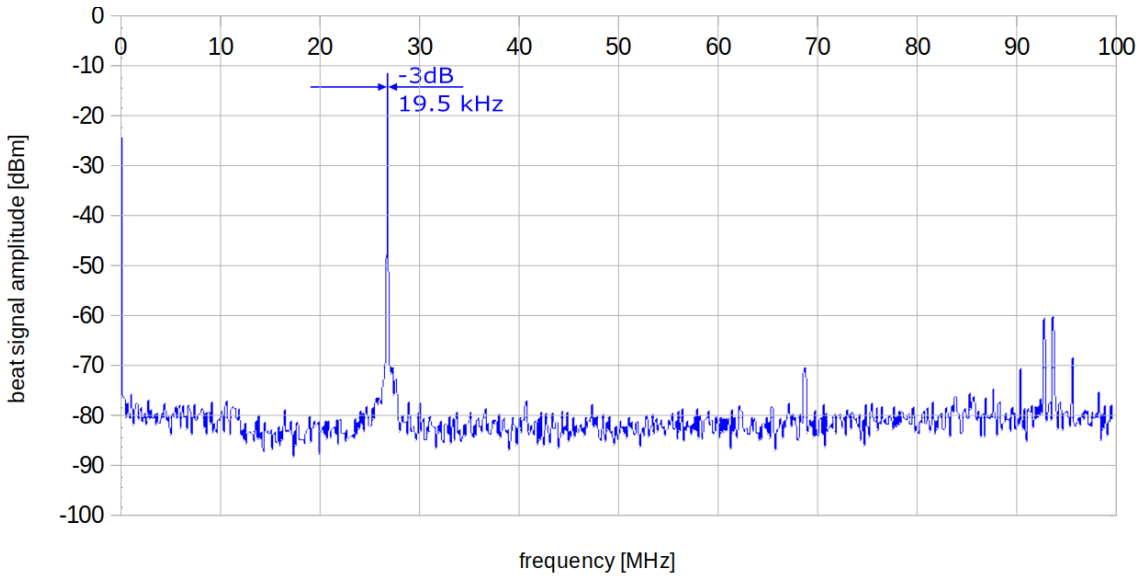

Figure 5.16: RF spectrum of beat signal at 1120 nm cavity fundamental output, generated with two similar MECSEL setups that include intra-cavity SHG into approximately 1.5 W of output power at 560 nm

The beat signal created provided a valuable benchmark for system optimization. Initially, pump current induced disturbances broadened the linewidth measured. After optimization of the current filters, and elimination of mechanical instabilities in the cavities locked to the laser, a -3 dB linewidth of $\Delta\nu < 20$ kHz could be detected at 50 ms sweep time. At longer integration times, the average result yielded values around $\Delta\nu \approx 40$ kHz, which is sufficient even for the narrow cooling line of Ytterbium (compare figure 1.2).

6 Conclusion

6.1 Discussion

The thermal lensing analysis, based on finite element analysis and comparison with measurement results from a Shack-Hartmann-Sensor setup, shows sufficient agreement to allow the simulation to be utilized as optimization tool for the design of MECSEL systems. Analysis of MECSEL thermal lensing has previously been performed and published (see [29], [92] and [112]).

In the first of these publications ([29]), finite element analysis results are described, based on dual side transparent heat spreading with the material property parameters of Diamond and Silicon Carbide. The results show a linear relationship of refractive power with the dissipated heat. These results are well comparable to the results of this work, prior to taking ASE and resonant amplification into account (compare figure 4.9). As discussed in section 4.2.2, spontaneous and amplified emission efficiency, and their saturation at elevated temperature, need to be taken into account when operating the laser near the maximum of potential output power. In this operational setting, the laser is close to thermal rollover, where the nonradiant losses are increasing in a nonlinear fashion. As an exemplary comparison below thermal rollover, the thermal lens dioptric power at 300 µm pump radius is determined to be $1/f_{therm} = 0.53\,\mathrm{dpt}$ in the simulation presented here - evaluating

a single side bonded SiC heat spreader of 500 µm thickness and 10 W absorbed power. The simulation results presented by Zhang et al. [29] suggest a thermal lens power of $1/f_{therm} = 0.49$ dpt at 10 W dissipated thermal power. It has to be noted, though, that this model does not take optical emission into account and is based on dual side heat spreading, whereas this work is focusing on single-side heat sinking. When scaling the calculation with a total of 45% emission efficiency (taking 55 % of the 10 W absorbed pump power into account), the model of [29] results in a dioptric power of approximately $1/f_{therm} = 0.27$ dpt. Given the linear dependency in this reference model, the result can be assumed to be $1/f_{therm} = 0.54$ dpt for a single-side heat spreader arrangement. This is in acceptable agreement with the data provided well below threshold in the simulations and measurements presented in this thesis. The model of [29] does not analyze higher order aberrations (which are highly relevant for optimizing efficient single transverse mode operation in MECSEL cavities). Also, the results in this theses provide a suitable method of predicting operation close to thermal rollover of MECSEL cavities.

The measurement results presented in [92] are based on GaInAsP Quantum well design, targeted for 825 nm emission. In the configuration reported, rather small pump diameters are used to allow operation of the laser setups above threshold. The authors analyzed the caustic of the laser output, determining the M^2 value, beam waist position and size. Then back-calculating into the resonator, using the ABCD matrix approach (see section 3.3), the effective thermal lens was determined. The authors present thermal lens focusing powers that saturate with rising pump powers and state "This reveals that the thermal gradient does not alter much before thermal rollover.". This statement is not supported by the results of the simulations of this thesis, showing a uniformly continuous development of the thermal gradient with pump power. It is in significant disagreement with the data simulated and measured in this work, where an exponential rise of thermally induced refractive power is simulated and measured with rising pump power. The simulations configured for this thesis do not provide sufficient local resolution to compare absolute values of the thermal lens to this publication. The data for

"cavity A" in section 4.2.4 are intended to provide a relative comparison to the data published and give a suitable explanation for the saturation effect. When the beam size in the gain chip increases with pump power, the effective dioptric power of the thermal lens (see section 4.2.4 for a exemplary data) is weakened, while aberrations are increased. This causes the effective focal length value to saturate with pump power, as described by the authors. But it is, as of the results of this work, purely induced by the diameter change of the resonant radiation penetrating over the non-spherical radial shape of the thermal lens.

Referencing to the same publication [92], another publication ([112]) states a comparable behavior. In this cavity (a plano/plano microchip MECSEL), the development of the caustik with pump power does not support the explanation given in section 4.2.4, as in this configuration, the beam diameter decreases in size with elevating pump power. The results in this work are prone to errors at larger relative pump power levels, due to the elevating beam parameter product M^2 with pump power. With the thermal lens power depicted as focal length (compare figure 4.14 on the left-hand side), the impression of saturation appears to be misleading.

Infrared and visible MECSEL ouput powers in excess of the results presented in this work have been published. The power target of 10 W was exceeded at the University of Dundee, with a longitudinally multi-mode setup at 1007 nm [28]. Record-breaking results were achieved at the University of New Mexico (UNM). The target of this development is the use of MECSEL technology as sodium guide star light sources. Using a multi-pass in-well pumping scheme, 28 W of multi-mode output power were achieved in at 1070 nm [29]. More recently, frequency-doubled >10 W single mode emission was shown at 589 nm, with a line width of <7 MHz [113]. The setup allowed locking to an external reference. Due to the comparably long cavity, the tuning bandwidth is limited to ± 500 MHz in the visible spectrum, 77 times smaller than the results achieved in this work. The line width reported in this work is in the two-digit kHz regime. It has to be noted, though, that the line width measurement at UNM was potentially limited by the test setup.

6.2 Conclusion

In this work, all fundamental technologies and design tools are covered that are required for the design and setup of narrow linewidth membrane lasers in the visible frequency range. The long-term linewidth and tunability measured on the systems set up in this work are superior to published data as of the date of completion of this thesis.

The thermal lens in the gain chip was analysed in computation and experiment. This thesis not only provides values for an effective thermal lens in the MECSEL gain chips, but describes methods and results for analysis of higher order aberrations. These are valuable for further optimization of the MECSEL technology, especially when aiming to increase the total output power. It is shown that in order to simulate the thermal lens at powers approaching thermal roll-over of the laser setup, amplified stimulated and spontaneous emission need to be taken into account. Also, the impact of Gaussian spot size on the effective thermal lens and its aberrations is found to be crutial.

Utilizing the thermo-optical effects of the SiC heat spreader in a MECSEL chip to stabilize the output frequency of the laser is novel and analyzed in experiment and model. The control method of pump current control allows MECSEL systems to be locked to a reference only by thermo-optical effects. This method has the capability of enabling locking bandwidths in excess of 500 kHz. In order to minimize amplitude noise, both piezoelectric cavity size and pump current modulation was implemented in this work.

Still, the line stability exceeds the theoretical limit by orders of magnitude. The first-order reason appears to be related to pump intensity noise and vibrational mechanical impact on the cavity length. Interpreting the frequency noise spectrum in figure 5.14, reduction of these noise sources could induce a significant improvement in linewidth, reaching the sub-kHz regime. In the experiments, the electric circuit of the pump modulation was a primary factor in the phase delay of the laser frequency modulation, and leaves room for future improvements. The line width requirements

for ytterbium and strontium cooling are already met with the results described, allowing the laser system to be utilized in quantum experiments and optical clocks.

6.3 Outlook

There is a demand for increasing laser power applied in experiments using optical lattices [114]. In these, an array of ultracold atoms can be trapped. This allows experiments on quantum many-body dynamics [115] and quantum computing [116]. The dominant practical challenge for increasing the efficiency and total output power of the system, while maintaining sufficient bandwidth for continuous single-frequency wavelength tuning in a robust and repeatable laser setup, is the control of parasitic etalons. Bonding Silicon Carbide to both surfaces of the gain membrane was proven feasible, but suppression of undesired etalon filtering requires a significant improvement of anti-reflection coating, or alternatively tight control of the relative wafer thicknesses. The evaluation of alternative transparent heat spreader material is in progress and may give additional opportunities for power scaling [117]. Currently, no wafer material with sufficient transparency and appropriate surface roughness is available, but Silicon Carbide.

The theoretical line width limit of the laser system described shows a potential for synchronization of MECSEL systems with optical clocks, providing a precision in the sub-kHz range. As an approach towards this goal, further reduction of the pump current noise, and optimization of the high-frequency response of the pump current modulation electronics are required. Optimization of the dynamic response of the pump current modulation electronics is expected to practically enable laser output frequency control bandwidths at the limits of the MECSEL thermal dynamic response. This is expected to improve the line stability and to significantly reduce the laser output linewidth.

A Appendix

A.1 Source Code for FEniCS

```
# Python code for performing the simulation of pump absorption, ASE and resonant pump depletion, using FEniCS to compute the FEA.
#  Note that the expressions (pump and lasing) need to be entered in C nomenclature.
# Credits to the work of Bilen Emek Abali - this code was initiated from an example (page 124) of his book
# "Computational reality" - ISBN  9789811024443, also listed in the references.
# The code was revised to work with Dolfin 2019.2.0, and expanded over the course of this work.

# SI units

from fenics import *
import numpy as np
from ufl import as_tensor # needed in version 2019.2.0
from ufl import Index # needed in version 2019.2.0
from mshr import *
from scipy.special import gamma, factorial
import time
parameters["allow_extrapolation"] = True
parameters["form_compiler"]["cpp_optimize"] = True
set_log_level(40)

um = 1e-6
c = 750 # J/(kg K) heat capacity
kappa = 480.0 #  W/(m K) thermal conductivity
tau_T = 0 # Temperature Gradient Lag - ignored
tau_q = 0 # Heat Flux Lag - ignored
h = 0 #natural convection coefficient in fJ/(ps um^2 K))
```

```
emis = 0 # emissivity - ignored
sigma = 0


Ppump = 10 # absorbed pump power in W

dia_pump=395*um #pump diameter/radius
w=dia_pump/2
w0=w
w2 = 1.14*w

th = 0.5E-3 # thickness in m
radius = 2.5E-3 # in m

k = 50  #supergauss order pump
k2 = 1 # supergauss order depletion

xml_file = "meshSI.xml"
mesh = Mesh(xml_file)
fd = MeshFunction('size_t', mesh, "meshSI_facet_region.xml");

Space = FunctionSpace((mesh), 'P', 1)
VectorSpace = VectorFunctionSpace(mesh, 'P', 1)
cells = MeshFunction('size_t',mesh,mesh.topology().dim()) #
    modified for version 2019.2.0
facets = MeshFunction('size_t',mesh,mesh.topology().dim()-1) #
    modified for version 2019.2.0
da = Measure('ds', domain=mesh, subdomain_data = facets)
dv = Measure('dx', domain=mesh, subdomain_data = cells)

u_out = 20
bc2 = DirichletBC(Space, Constant(u_out), fd, 55)
bc = [bc2]
Ta = u_out

def calc_FEA(f) :

    frequency = f
    periods = 10
    datapoints = 15
    t = 0.0
    t_end=periods/frequency
    Dt=1/frequency/datapoints

    initial_T = Expression("Tini", Tini=Ta, degree=3)
    T0 = interpolate(initial_T, Space)

    A = float(k/(2*w*gamma([1/k])))
    A2 = float(k2/(2*w*gamma([1/k2])))
    Pump1 = Expression('Pmax*A*A*mu*1*exp(-abs(pow(pow(x[0]*x[0] +
    x[1]*x[1], 0.5)/w, k)))*exp(-(pow(-mu*(x[2]), 2))) ',degree=3,
    Pmax=Ppump,w=w, mu=180000, k=k, A=A, w0=w0) #power (w2
    localises the z-coordinates)
    Laser = Expression('Pmax*A*A*mu*1*exp(-abs(pow(pow(x[0]*x[0] +
    x[1]*x[1], 0.5)/w, k)))*exp(-(pow(-mu*(x[2]), 2))) ',degree=3,
```

```
    Pmax=0.14*Ppump,w=w, mu=180000, k=k2, A=A2, w0=w0) #power (w2
    localises the z-coordinates)
75  Pump = Pump1 - Laser
76
77  T = Function(Space)
78  del_T = TestFunction(Space)
79  dT = TrialFunction(Space)
80  q0 = Function(VectorSpace)
81  i=Index() # needed in version 2019.2.0
82  G = as_tensor(T.dx(i), (i))
83  G0 = as_tensor(T0.dx(i), (i))
84
85  q = as_tensor(Dt/(Dt + tau_q) * (tau_q/Dt*q0[i] - kappa*(1+
    tau_T/Dt)*G[i] + kappa*tau_T/Dt*G0[i]),(i)) #left comma away at
     end for 2019.2.0
86
87  Form = (c/Dt*(T-T0)*del_T - q[i]*del_T.dx(i) -  Pump*del_T +
    Pump*del_T* (0.15*(1+cos((T-Ta)*0.1))) ) * dv + (h*(T-Ta) +
    emis*sigma*(T**4 - Ta**4))*del_T*da
88  Gain = derivative(Form, T, dT)
89
90  calc_time = 0
91  elapsed_time = 0
92  # read steady-state data set
93  f_in =  XDMFFile("state_end.xdmf")
94  f_in.read_checkpoint(T,"Pump",0)
95  T0.assign (T)
96
97  file_T = File(f"P={Ppump}W_2w0={dia_pump}um_frequency={f}
    periods={periods}datapoints={datapoints}.pvd")
98  file_T << (T,t)
99
100 t_series = np. arange (Dt,t_end,Dt)
101
102 size = np.size(t_series)
103
104 for t in t_series:
105     print ("step",size,"frequency",f, "minutes",(np.round((
    t_series.size*calc_time-elapsed_time)/60,1)))
106     size = size -1
107     st = time.time() #start time
108     Pump1.Pmax = Ppump *(1 + 0.1*np.sin(t*frequency*2*3.1415))
109     solve(Form==0, T, bc, J=Gain, solver_parameters={"
    newton_solver":{"linear_solver": "mumps", "relative_tolerance":
     1e-3 } },form_compiler_parameters={"cpp_optimize":True, "
    representation": "uflacs", "quadrature_degree":2} )
110
111     file_T << (T,t)
112     q0 = project (q, VectorSpace)
113     T0.assign (T)
114
115     et = time.time() #end time
116     calc_time = (calc_time +(et - st))/2 # moving average of
    calculation time
117     elapsed_time = elapsed_time + calc_time
```

```
118
119 N=22 #N=4 and 3,6,N for 1000, 10000, 100000, 1000000
120 freq_range = np.logspace(3, 6, N, endpoint=True)
121 print (freq_range)
122
123 for freq in freq_range:
124     calc_FEA(freq)
125
126 #write steady state:
127 """
128 f_out = XDMFFile("state_end.xdmf")
129 f_out.write_checkpoint(project(T, Space), "Pump", t, XDMFFile.
      Encoding.HDF5, True) #see https://fenicsproject.discourse.group
      /t/loading-xdmf-data-back-in/1925/4
130 f_out.close()
131 """
```

References

[1] R. N. Hall et al. “Coherent Light Emission From GaAs Junctions”. In: *Physical Review Letters* 9.9 (Nov. 1962), pp. 366–368.

[2] Marshall I. Nathan and Gerald Burns. “RECOMBINATION RADIATION IN GaAs BY OPTICAL AND ELECTRICAL INJECTION”. In: *Applied Physics Letters* 1.4 (Dec. 1962), pp. 89–90.

[3] L. Van Ruyven. “A Semiconductor Laser for Optical Disc Systems”. In: *IEEE Transactions on Consumer Electronics* CE-27.2 (May 1981), pp. 153–158.

[4] J. Osmundsen and N. Gade. “Influence of optical feedback on laser frequency spectrum and threshold conditions”. In: *IEEE Journal of Quantum Electronics* 19.3 (Mar. 1983), pp. 465–469.

[5] K. C. Harvey and C. J. Myatt. “External-cavity diode laser using a grazing-incidence diffraction grating”. In: *Optics Letters* 16.12 (June 1991), p. 910.

[6] L. Hollberg. “Diode Lasers and their Application to Spectroscopy”. In: *Applied Laser Spectroscopy*. Springer US, 1990, pp. 117–125.

[7] Mark S. Zediker and Erik Zucker. “High-power diode laser technology XX: a retrospective on 20 years of progress”. In: *High-Power Diode Laser Technology XX*. Ed. by Mark S. Zediker and Erik P. Zucker. SPIE, Mar. 2022, p. 1.

[8] D. Petring, C. Benter, and R. Poprawe. “Fundamentals and applications of diode laser welding”. In: *International Congress on Applications of Lasers amp; Electro-Optics*. Laser Institute of America, 2001, pp. 1311–1320.

[9] Oleg M. Efimov et al. “High-efficiency Bragg gratings in photothermorefractive glass”. In: *Appl. Opt.* 38.4 (Feb. 1999), pp. 619–627. URL: `https://opg.optica.org/ao/abstract.cfm?URI=ao-38-4-619`.

[10] Leonid B. Glebov. “High brightness laser design based on volume Bragg gratings”. In: *SPIE Proceedings*. Ed. by Gary L. Wood and Mark A. Dubinskii. SPIE, May 2006.

[11] Simon Rauch and Joachim Sacher. “Compact Bragg Grating Stabilized Ridge Waveguide Laser Module With a Power of 380 mW at 780 nm”. In: *IEEE Photonics Technology Letters* 27.16 (Aug. 2015), pp. 1737–1740.

[12] J. N. Walpole et al. “High-power strained-layer InGaAs/AlGaAs tapered traveling wave amplifier”. In: *Applied Physics Letters* 61.7 (Aug. 1992), pp. 740–742.

[13] Alexander Bachmann et al. “High power diode lasers for quantum technologies”. In: *High-Power Diode Laser Technology XXII*. Ed. by Erik P. Zucker, Jenna Campbell, and Mark S. Zediker. SPIE, Mar. 2024, p. 42.

[14] Shuji Nakamura and M. R. Krames. “History of Gallium–Nitride-Based Light-Emitting Diodes for Illumination”. In: *Proceedings of the IEEE* 101.10 (Oct. 2013), pp. 2211–2220.

[15] E.J. Thrush et al. “The growth of 1550 nm integrated laser/modulator structures by MOCVD”. In: *Proceedings of 1994 IEEE 6th International Conference on Indium Phosphide and Related Materials (IPRM)*. ICIPRM-94. IEEE, pp. 72–75.

[16] B. Ainslie and C. Day. “A review of single-mode fibers with modified dispersion characteristics”. In: *Journal of Lightwave Technology* 4.8 (1986), pp. 967–979.

[17] P. A. Franken et al. “Generation of Optical Harmonics”. In: *Physical Review Letters* 7.4 (Aug. 1961), pp. 118–119.

[18] P. D. Maker et al. “Effects of Dispersion and Focusing on the Production of Optical Harmonics”. In: *Physical Review Letters* 8.1 (Jan. 1962), pp. 21–22.

[19] S. Akhmanov et al. “Observation of Parametric Amplification in the Optical Range”. In: *Jetp Letters - JETP LETT-ENGL TR* 2 (Jan. 1965).

[20] M. Fejer et al. “Nonlinear Optics in Single Crystal Fibers”. In: *Tunable Solid State Lasers for Remote Sensing*. Springer Berlin Heidelberg, 1985, pp. 141–145.

[21] Jiro Saikawa et al. “High-energy, narrow-bandwidth periodically poled Mg-doped $LiNbO_3$ optical parametric oscillator with a volume Bragg grating”. In: *Optics Letters* 32.20 (Oct. 2007), p. 2996.

[22] Robert N Hall et al. “Coherent light emission from GaAs junctions”. In: *Physical Review Letters* 9.9 (1962), p. 366.

[23] Kenichi Iga. “Forty years of vertical-cavity surface-emitting laser: Invention and innovation”. In: *Japanese Journal of Applied Physics* 57.8S2 (July 2018), 08PA01.

[24] Haruhisa Soda et al. “GaInAsP/InP Surface Emitting Injection Lasers”. In: *Japanese Journal of Applied Physics* 18.12 (Dec. 1979), pp. 2329–2330.

[25] M. Kuznetsov et al. “High-power (0.5 W CW) diode-pumped vertical-external-cavity surface-emitting semiconductor lasers with circular TEM00 beams”. In: *IEEE Photonics Technology Letters* 9.8 (Aug. 1997), pp. 1063–1065.

[26] B. Heinen et al. “106 W continuous-wave output power from vertical-external-cavity surface-emitting laser”. In: *Electronics Letters* 48.9 (2012), p. 516.

[27] Zhou Yang et al. “Optically pumped DBR-free semiconductor disk lasers”. In: *Optics Express* 23.26 (Dec. 2015), p. 33164.

[28] S. Mirkhanov et al. “DBR-free semiconductor disc laser on SiC heatspreader emitting 10.1 W at 1007 nm”. In: *Electronics Letters* 53.23 (Nov. 2017), pp. 1537–1539.

[29] Mingyang Zhang et al. “Hybrid membrane-external-cavity surface-emitting laser”. In: *Optics Express* 30.23 (Nov. 2022), p. 42470.

[30] A. Ashkin. “Acceleration and Trapping of Particles by Radiation Pressure”. In: *Physical Review Letters* 24.4 (Jan. 1970), pp. 156–159.

[31] T.W. Hänsch and A.L. Schawlow. “Cooling of gases by laser radiation”. In: *Optics Communications* 13.1 (Jan. 1975), pp. 68–69.

[32] William D. Phillips. “Nobel Lecture: Laser cooling and trapping of neutral atoms”. In: *Reviews of Modern Physics* 70.3 (July 1998), pp. 721–741.

[33] Masami Yasuda et al. “Development of an Yb optical lattice clock using a fermionic isotope”. In: *SPIE Proceedings*. Ed. by Tetsuya Ido and Derryck T. Reid. SPIE, Aug. 2009.

[34] G. Ferrari et al. “Precision Frequency Measurement of Visible Intercombination Lines of Strontium”. In: *Physical Review Letters* 91.24 (Dec. 2003), p. 243002.

[35] E. L. Raab et al. “Trapping of Neutral Sodium Atoms with Radiation Pressure”. In: *Physical Review Letters* 59.23 (Dec. 1987), pp. 2631–2634.

[36] Yebing Wang et al. “Recent Advances Concerning the 87Sr Optical Lattice Clock at the National Time Service Center”. In: *Applied Sciences* 8.11 (Nov. 2018), p. 2194.

[37] Huidong Kim et al. “Absolute frequency measurement of the 171Yb optical lattice clock at KRISS using TAI for over a year”. In: *Metrologia* 58.5 (Aug. 2021), p. 055007.

[38] Tara Fortier and Esther Baumann. “20 years of developments in optical frequency comb technology and applications”. In: *Communications Physics* 2.1 (Dec. 2019).

[39] Albert Schliesser, Nathalie Picqué, and Theodor W. Hänsch. “Mid-infrared frequency combs”. In: *Nature Photonics* 6.7 (June 2012), pp. 440–449.

[40] Andrew D. Ludlow et al. “Optical atomic clocks”. In: *Reviews of Modern Physics* 87.2 (June 2015), pp. 637–701.

[41] Stefano Origlia et al. “Development of a strontium optical lattice clock for the SOC mission on the ISS”. In: (Mar. 2016).

[42] Gleb Belotelov, Denis Sutyrin, and Sergey Slyusarev. “Development of Transportable and Portable Optical Lattice Clocks on Ytterbium Atoms”. In: *2020 Joint Conference of the IEEE International Frequency Control Symposium and International Symposium on Applications of Ferroelectrics (IFCS-ISAF)*. IEEE, July 2020.

[43] Hongchi Lei. “GaAs-Based Distributed Feedback Lasers Based on GaAs-InGaP Regrowth Technology”. PhD thesis. Sept. 2017.

[44] D Schlenker et al. “Growth of highly strained GaInAs/GaAs quantum wells for 1.2 m wavelength lasers”. In: *Journal of Crystal Growth* 209.1 (Jan. 2000), pp. 27–36.

[45] J.-Y. Kim et al. “Highly efficient green VECSEL with intra-cavity diamond heat spreader”. In: *Electronics Letters* 43.2 (2007), p. 105.

[46] R. O. Carlson, G. A. Slack, and S. J. Silverman. “Thermal Conductivity of GaAs and $GaAs_{1-x}P_x$ Laser Semiconductors”. In: *Journal of Applied Physics* 36.2 (Feb. 1965), pp. 505–507.

[47] E. D. Pierron, D. L. Parker, and J. B. McNeely. “Coefficient of Expansion of GaAs, GaP, and Ga(As, P) Compounds from -62° to 200°C”. In: *Journal of Applied Physics* 38.12 (Nov. 1967), pp. 4669–4671.

[48] Xin Qian, Puqing Jiang, and Ronggui Yang. “Anisotropic thermal conductivity of 4H and 6H silicon carbide measured using time-domain thermoreflectance”. In: *Materials Today Physics* 3 (Dec. 2017), pp. 70–75.

[49] Z. Li and R. C. Bradt. "Thermal expansion of the hexagonal (4H) polytype of SiC". In: *Journal of Applied Physics* 60.2 (July 1986), pp. 612–614.

[50] A. V. Inyushkin et al. "Thermal conductivity of high purity synthetic single crystal diamonds". In: *Physical Review B* 97.14 (Apr. 2018), p. 144305.

[51] Katsuji Haruna et al. "Thermal Expansion Coefficient of Synthetic Diamond Single Crystal at Low Temperatures". In: *Japanese Journal of Applied Physics* 31.8R (Aug. 1992), p. 2527.

[52] L. Risegari et al. "Measurement of the thermal conductivity of copper samples between 30 and 150 mK". In: *Cryogenics* 44.12 (Dec. 2004), pp. 875–878.

[53] F. R. Kroeger and C. A. Swenson. "Absolute linear thermal-expansion measurements on copper and aluminum from 5 to 320 K". In: *Journal of Applied Physics* 48.3 (Mar. 1977), pp. 853–864.

[54] Cheng Zhang, Rami ElAfandy, and Jung Han. "Distributed Bragg Reflectors for GaN-Based Vertical-Cavity Surface-Emitting Lasers". In: *Applied Sciences* 9.8 (Apr. 2019), p. 1593.

[55] I E Dzyaloshinskii, E M Lifshitz, and Lev P Pitaevskii. "GENERAL THEORY OF VAN DER WAALS' FORCES". In: *Soviet Physics Uspekhi* 4.2 (Feb. 1961), pp. 153–176.

[56] Siqi Zhao et al. "Surface Uniformity of Wafer-Scale 4H-SiC Epitaxial Layers Grown under Various Epitaxial Conditions". In: *Coatings* 12.5 (Apr. 2022), p. 597.

[57] Garrett D. Cole et al. "Chip- and Wafer-Scale Manufacturing of High-Power Membrane-External-Cavity Surface-Emitting Laser Gain Elements". In: *Conference on Lasers and Electro-Optics*. Optica Publishing Group, 2022, ATh2L.2.

[58] Garrett D. Cole et al. "Tenfold reduction of Brownian noise in high-reflectivity optical coatings". In: *Nature Photonics* 7.8 (July 2013), pp. 644–650.

[59] M. Kuznetsov et al. "Design and characteristics of high-power (<0.5 W CW) diode-pumped vertical-external-cavity surface-emitting semiconductor lasers with circular TEM_{00} beams". In: *IEEE Journal of Selected Topics in Quantum Electronics* 5.3 (1999), pp. 561–573.

[60] Okhotnikov. *Semiconductor Disk Lasers: Physics and Technology*. Wiley, Apr. 2010.

[61] S. Lovold et al. "Frequency tuning characteristics of a Q-switched Co:MgF laser". In: *IEEE Journal of Quantum Electronics* 21.3 (Mar. 1985), pp. 202–208.

[62] Max Born et al. *Principles of Optics*. Cambridge University Press, Oct. 1999.

[63] R. Clark Jones. "A New Calculus for the Treatment of Optical SystemsI. Description and Discussion of the Calculus". In: *J. Opt. Soc. Am.* 31.7 (July 1941), pp. 488–493.

[64] Arnold L. Bloom. "Modes of a laser resonator containing tilted birefringent plates". In: *J. Opt. Soc. Am.* 64.4 (Apr. 1974), pp. 447–452.

[65] Petr Hlubina and Dalibor Ciprian. "Birefringence dispersion in a quartz crystal retrieved from a channeled spectrum resolved by a fiber-optic spectrometer". In: *Optics Communications* 284.12 (June 2011), pp. 2683–2686.

[66] Umıt Demırbas. “Off-surface optic axis birefringent filters for smooth tuning of broadband lasers”. In: *Applied Optics* 56.28 (Sept. 2017), p. 7815.

[67] Mani Hossein-Zadeh. “Electro-optic microdisk RF-wireless receiver”. In: *Dissertation at the University of Southern California* (Jan. 2004).

[68] Herman van de Stadt and Johan M. Muller. “Multimirror Fabry–Perot interferometers”. In: *J. Opt. Soc. Am. A* 2.8 (Aug. 1985), pp. 1363–1370.

[69] Steven J. Byrnes. *Multilayer optical calculations*. arXiv, 2016.

[70] S.W. Corzine et al. “Design of Fabry-Perot surface-emitting lasers with a periodic gain structure”. In: *IEEE Journal of Quantum Electronics* 25.6 (June 1989), pp. 1513–1524.

[71] Shota Yamada et al. “Experimental investigation of thermo-optic effects in SiC and Si photonic crystal nanocavities”. In: *Optics Letters* 36.20 (Oct. 2011), p. 3981.

[72] Orazio Svelto. *Principles of Lasers*. Springer US, 2010.

[73] A. Gerrard and J.M. Burch. *Introduction to Matrix Methods in Optics*. Dover Books on Physics. Dover, 1994.

[74] Frank L. Pedrotti, Leno M. Pedrotti, and Leno S. Pedrotti. *Introduction to Optics*. Cambridge University Press, Dec. 2017.

[75] H. Kogelnik and T. Li. “Laser Beams and Resonators”. In: *Appl. Opt.* 5.10 (Oct. 1966), pp. 1550–1567. URL: `https://opg.optica.org/ao/abstract.cfm?URI=ao-5-10-1550`.

[76] Eckhard Zanger et al. “Diode-pumped cw all solid-state laser at 266 nm”. In: *Advanced Solid State Lasers*. Optica Publishing Group, 1999, MB4.

[77] Gorachand Ghosh, Michiyuki Endo, and Takashi Iwasalu. “Temperature-dependent Sellmeier coefficients and chromatic dispersions for some optical fiber glasses”. In: *Journal of Lightwave Technology* 12 (1994), pp. 1338–1342.

[78] Sandra Stry et al. “Compact tunable diode laser with diffraction-limited 1 Watt for atom cooling and trapping”. In: *Proceedings of SPIE - The International Society for Optical Engineering* 5336 (June 2004).

[79] Alexandr P Bogatov, P G Eliseev, and B N Sverdlov. “Anomalous interaction of spectral modes in a semiconductor laser”. In: *Soviet Journal of Quantum Electronics* 4.10 (Oct. 1975), pp. 1275–1276.

[80] Daan Lenstra and Mirvais Yousefi. “Rate-equation model for multi-mode semiconductor lasers with spatial hole burning”. In: *Optics Express* 22.7 (Apr. 2014), p. 8143.

[81] Andre Ribes and Christian Caremoli. “Salome platform component model for numerical simulation”. In: *31st Annual International Computer Software and Applications Conference - Vol. 2 - (COMPSAC 2007)*. IEEE, July 2007.

[82] Igor A. Baratta et al. *DOLFINx: The next generation FEniCS problem solving environment*. en. 2023.

[83] Matthew W. Scroggs et al. “Construction of Arbitrary Order Finite Element Degree-of-Freedom Maps on Polygonal and Polyhedral Cell Meshes”. In: *ACM Transactions on Mathematical Software* 48.2 (May 2022), pp. 1–23.

[84] Martin S. Alnæs et al. “Unified form language: A domain-specific language for weak formulations of partial differential equations”. In: *ACM Transactions on Mathematical Software* 40.2 (Feb. 2014), pp. 1–37.

[85] Bilen Emek Abali. *Computational Reality*. Springer Singapore, 2017.

[86] P. J. Timans. “The experimental determination of the temperature dependence of the total emissivity of GaAs using a new temperature measurement technique”. In: *Journal of Applied Physics* 72.2 (July 1992), pp. 660–670.

[87] G. Hanreich and J. Nicolics. “Measuring the natural convective heat transfer coefficient at the surface of electronic components”. In: *IMTC 2001. Proceedings of the 18th IEEE Instrumentation and Measurement Technology Conference. Rediscovering Measurement in the Age of Informatics (Cat. No.01CH 37188)*. IMTC-01. IEEE.

[88] Rusheng Wei et al. “Thermal conductivity of 4H-SiC single crystals”. In: *Journal of Applied Physics* 113 (Feb. 2013).

[89] Joseph W Goodman. *Introduction to Fourier optics*. Roberts and Company publishers, 2005.

[90] WH Southwell. “Validity of the Fresnel approximation in the near field”. In: *JOSA* 71.1 (1981), pp. 7–14.

[91] Gleb Vdovin and Fred van Goor. URL: `https://opticspy.github.io/lightpipes/`.

[92] Hoy-My Phung et al. “Power scaling and thermal lensing in 825 nm emitting membrane external-cavity surface-emitting lasers”. In: *Optics Letters* 45.2 (Jan. 2020), p. 547.

[93] Ho Seong Lee et al. “Frequency stabilization of a directly modulated semiconductor laser”. In: *Review of Scientific Instruments* 61.9 (Sept. 1990), pp. 2478–2480.

[94] Tilman Preuschoff et al. “Wideband current modulation of diode lasers for frequency stabilization”. In: *Review of Scientific Instruments* 93.6 (June 2022).

[95] M. Ito and T. Kimura. “Carrier density dependence of refractive index in AlGaAs semiconductor lasers”. In: *IEEE Journal of Quantum Electronics* 16.9 (Sept. 1980), pp. 910–911.

[96] Aleksandar Gjurchinovski. “The Doppler effect from a uniformly moving mirror”. In: *European Journal of Physics* 26.4 (May 2005), pp. 643–646.

[97] Arnhold Simonsen et al. “Bidirectional electrostatic MEMS-tunable VCSELs”. In: *Optics Letters* 49.4 (Feb. 2024), p. 802.

[98] Malik Rakhmanov. “Doppler-induced dynamics of fields in Fabry–Perot cavities with suspended mirrors”. In: *Applied Optics* 40.12 (Apr. 2001), p. 1942.

[99] Robert W. Boyd. “The Nonlinear Optical Susceptibility”. In: *Nonlinear Optics*. Elsevier, 2020, pp. 1–64.

[100] Walter Koechner. *Solid-State Laser Engineering*. Springer Berlin Heidelberg, 1999.

[101] K. Kato. "Temperature-tuned 90° phase-matching properties of LiB_3O_5". In: *IEEE Journal of Quantum Electronics* 30.12 (1994), pp. 2950–2952.

[102] Castech Inc. *LBO Material Properties*. 2024. URL: `https://www.castech.com/product/LBO---Lithium-Triborate-121.html` (visited on 10/30/2024).

[103] G. D. Boyd and D. A. Kleinman. "Parametric Interaction of Focused Gaussian Light Beams". In: *Journal of Applied Physics* 39.8 (July 1968), pp. 3597–3639.

[104] R. W. P. Drever et al. "Laser phase and frequency stabilization using an optical resonator". In: *Applied Physics B Photophysics and Laser Chemistry* 31.2 (June 1983), pp. 97–105.

[105] Eric D. Black. "An introduction to Pound–Drever–Hall laser frequency stabilization". In: *American Journal of Physics* 69.1 (Jan. 2001), pp. 79–87.

[106] T.W. Hansch and B. Couillaud. "Laser frequency stabilization by polarization spectroscopy of a reflecting reference cavity". In: *Optics Communications* 35.3 (Dec. 1980), pp. 441–444.

[107] Arthur L Schawlow and Charles H Townes. "Infrared and optical masers". In: *Physical review* 112.6 (1958), p. 1940.

[108] Melvin Lax. "Classical Noise. V. Noise in Self-Sustained Oscillators". In: *Physical Review* 160.2 (Aug. 1967), pp. 290–307.

[109] Dr. Rüdiger Paschotta. *Derivation of the SchawlowTownes Linewidth of Lasers*. 2013. URL: `https://www.rp-photonics.com/Schawlow-Townes_linewidth.pdf` (visited on 06/10/2024).

[110] Jiaping Qian et al. "2 W single-frequency, low-noise 509 nm laser via single-pass frequency doubling of an ECDL-seeded Yb fiber amplifier". In: *Appl. Opt.* 57.29 (Oct. 2018), pp. 8733–8737.

[111] Hanne Ludvigsen, Mika Tossavainen, and Matti Kaivola. "Laser linewidth measurements using self-homodyne detection with short delay". In: *Optics Communications* 155.1–3 (Oct. 1998), pp. 180–186.

[112] Jakob Hirlinger-Alexander et al. *Microchip semiconductor membrane external-cavity surface-emitting laser*. arXiv, 2025.

[113] M. Zhang et al. "Frequency-Stabilized High-Power 589 nm Semiconductor Disk Laser for Guide Star Applications". In: *Laser Congress 2024 (ASSL, LAC, LS&C)*. Optica Publishing Group, 2024, ATu1A.4.

[114] Alan Bregazzi et al. "Single-Beam Grating-Chip 3D and 1D Optical Lattices". In: *Physical Review Letters* 134.1 (Jan. 2025), p. 013001.

[115] Simon Karch et al. *Probing quantum many-body dynamics using subsystem Loschmidt echos*. 2025.

[116] Mohamed Barhoumi, Riccardo Bassoli, and Frank H.P. Fitzek. "Qubit optical-cavity interaction and quantum synchronization of two qubits inside an optical lattice". In: *Materials Science and Engineering: B* 311 (Jan. 2025), p. 117819.

[117] Sayan Seal and Homer Mantooth. “High Performance Silicon Carbide Power Packaging—Past Trends, Present Practices, and Future Directions”. In: *Energies* 10.3 (Mar. 2017), p. 341.